THE UNIVERSITY *of* EDINBURGH

Ultrafast photophysics and magnetisation dynamics of Cr(III)-based Prussian blue analogue thin films

THE UNIVERSITY *of* EDINBURGH

Harry Alfred Lewis

University of Edinburgh

This thesis is submitted for the degree of

Doctor of Philosophy

2023

Abstract

As reliance on the use of magnetism for technological applications increases, molecule-based magnetic materials have emerged as interesting candidates for study due to their immense chemical flexibility and tuneable physical properties. Of these, Prussian blue analogues (PBAs) are an interesting subclass which conform to a simple cubic structure and their composition can be readily modified to incorporate a variety of different transition metal species. This has given rise to a wide range of materials with different spectral characteristics and notably high magnetic ordering temperatures. As such, PBAs provide useful model systems for investigations into how magnetic properties may be influenced through photoexcitation. This body of work aims to provide a description of photoinduced electronic and magnetisation dynamics in a Cr(III)-based PBA on ultrafast timescales using a combination of transient absorption (TA) spectroscopy and time-resolved magneto-optics (TR-MO) in transmission geometry.

The materials were synthesised in the form of thin films through electrodeposition from solution. While the greatest magneto-optical response is afforded in principle through the use of thicker films, these tend to scatter light heavily. A way to circumvent this is encapsulation of the films using a suitable agent of similar refractive index. For this purpose, two adhesives that are transparent in the visible region were tested for both mixed-valence Cr–Cr and Fe–Cr PBAs. A vast improvement in transmittance was observed, particularly for Cr–Cr PBA where spectral features that previously had been completely obscured by a broad background could be more clearly resolved. This

was attributed to the reduction of air/film interfaces in our polycrystalline materials, which act as a major source of light scatter. Encapsulation became part of standard film preparation for TA and TR-MO measurements, which would typically use films of ∼1 µm thickness.

Thus far, the dynamics of Cr(III)-based PBAs have been interpreted using the ultrafast photophysics observed in $Cr(acac)_3$ (acac = acetylacetonate) as a model. However, there are large differences in the structure and bonding observed within this complex compared to the hexacyanochromate(III) anion which forms the molecular "backbone" of said PBAs. Hence, the ultrafast photophysics in hexacyanochromate(III) in aqueous solution were investigated using TA to validate the existing interpretation. A broad excited state absorption feature was observed upon ligand-field excitation, consistent with observations in $Cr(acac)_3$ while also conforming to similar kinetics. However, a narrow, secondary feature was also observed to grow in within 2 ps. While the origins of the two features remain unknown, absorption from the quartet manifold, the spin-flipped doublet manifold or from photoproducts have been presented as possible causes.

For the combined TA and TR-MO studies, thin films of Cr–Cr PBA were produced with magnetic ordering temperature, T_c, of ∼160 K. Broadband TA measurements revealed an excited state absorption which overlapped with a broad, complex feature that accounted for most of the spectrum. Kinetic analyses of these two spectral components determined that their intensities both evolved on different characteristic timescales. Complementary TR-MO experiments indicated that the change in magneto-optical response over time conformed to the same kinetics as the broad spectral feature, suggesting that both the electronic and magnetisation dynamics are linked. Due to the complex stoichiometry of the material, assignment of the origin of these features is ongoing.

Lay summary

Much of the technology we use in modern life, such as microwaves, speakers and mobile phones, have some form of magnetic component. One key area that employs magnets is data storage, where magnetic hard drives dominated the market for a very long time. These have traditionally used thin films of metal which consist of many magnetic domains: small, independent regions that can store data as binary "bits". These bits exist in either a "0" or a "1" state which is controlled using a small electromagnet held close to the domain to change its magnetic properties. The greater the number of domains that can be included, the more data can be stored on your hard drive. However, there is a minimum size limit that these domains can reach before the storage capacity can't be increased any more without the risk of data loss. Thus, there is a lot of interest in solving this issue through the development of different materials.

Molecule-based magnets are being suggested by researchers as a potential replacement for metal-based materials in data storage because magnetic domains can essentially be reduced down to single atoms, which hypothetically could hugely increase data storage capacity. They can also be easily produced from solution, unlike metal-based magnets which require energy-intensive processing. In an age where we are much more environmentally-conscious, this is also a welcome benefit.

Another limitation of existing magnetic data storage is that read/write speeds — the time it takes to load or save information — are limited. These devices will increasingly become incapable of meeting our needs as efficient processing of more and

more data is required. Using light to read or write to magnetic domains can resolve this problem as it can do this job on ultrafast (i.e. 10^{-15}–10^{-9} s) timescales. This is currently a very active area of research.

The primary goal of my work is to investigate how the magnetic properties of molecule-based magnets can be both controlled and detected using light, which has huge potential in the production of high density, high speed data storage. This involves performing "pump–probe" experiments on thin films in a manner similar to "writing" and "reading", where an intense pulse of light (the "pump") provides energy to the film to induce a change in its magnetic properties which is then detected using a second, weaker pulse of light (the "probe") after a fixed time delay. This gives us a snapshot of the film's magnetic behaviour at that moment. When the experiment is repeated with a number of different time delays, we can effectively build a movie that shows how quickly the magnetic properties change and through what mechanisms. In this thesis, I detail how these experiments are performed on a member of the "Prussian blue analogue" (PBA) family of molecule-based magnetic materials, which are made from transition metal cyanides and come in a wide range of different colours.

For these pump–probe experiments to be successful, it is necessary for the films to be highly transparent so that light can pass through unperturbed. Unfortunately, thin films of PBAs tend to be quite opaque due to their tendency to "scatter" light in multiple directions. A secondary objective of my work is to develop better film preparation procedures to mitigate this and improve the quality of our data. This has been successfully achieved by sealing the films with glue and a glass coverslip, which provides a smooth surface for light to pass through.

Declaration

I declare that this thesis has been composed solely by myself and that it has not been submitted, in whole or in part, in any previous application for a degree. Except where stated otherwise by reference or acknowledgement, the work presented is entirely my own.

Harry Alfred Lewis

2023

Acknowledgements

It's been four long years and I would never have gotten to this stage if not for numerous people. I'd first like to thank my supervisory team: Dr. Olof Johansson for his unmatched passion for science and many, many ideas, and Professor Eleanor Campbell for her advice at various stages and for letting me play with her laser system for three years. Likewise, I'm grateful to Professor Neil Robertson for providing access to equipment for film deposition and for practical advice.

I thank the past members of the group and laser lab — Dr. Luke Hedley, Dr. Florian Liedy, Dr. Minas Stefanou, Dr. Debi Pattnaik and phenomenal Masters student Paulina Majchrzak — who trained me in the ways of the femtosecond arts (amongst other things) and showed so much patience at a time when I was utterly clueless. Also, I acknowledge past BSc student Jake Kirkpatrick in pioneering the work on thin film encapsulation: a total game-changer for optical measurements.

A huge thank you goes to the more recent members of the group — Dr. Erica Sutcliffe, Kyle Barlow, Dr. Thomas Stonelake and Dr. Ryan Phelps — for providing a truly great working environment and sharing their wealth of knowledge on ultrafast phenomena, inorganic photophysics and condensed matter physics.

I thank Dr. Andrei Gromov and Dr. Oleg Nerushev for advice and training on the micro-Raman and AFM instruments. I'm also grateful to George Steedman and Lloyd Mitchell in the workshop for providing fast, bespoke solutions to not-so-routine problems and helping us keep the lab in top shape.

Table of contents

Acronyms

AFM atomic force microscopy.

BBO β-barium borate.

BET back-electron transfer.

ESA excited state absorption.

FE Faraday ellipticity.

FTO fluorine-doped tin oxide.

GSB ground state bleach.

HS high-spin.

IC internal conversion.

IR infrared.

IRF instrument response function.

ISC intersystem crossing.

LMCT ligand–metal charge transfer.

LS low-spin.

MCD magnetic circular dichroism.

MM′CT metal–metal charge transfer.

MO magneto-optics.

MORD magnetic optical rotary dispersion.

ND neutral density.

NIR near-infrared.

NOA 61 Norland optical adhesive 61.

OPA optical parametric amplifier.

PBA Prussian blue analogue.

SCO spin crossover.

SEI superexchange interaction.

SHG second-harmonic generation.

SQUID superconducting quantum interference device.

TA transient absorption.

TM transition metal.

TR-FE time-resolved Faraday ellipticity.

TR-MCD time-resolved magnetic circular dichroism.

TR-MO time-resolved magneto-optics.

TT transient transmittance.

UV ultraviolet.

XPM cross-phase modulation.

Chapter 1

Introduction

1.1 Applications of magnetic materials in data storage and current limitations

The manipulation of magnetic behaviour, and technologies based on this, has been one of the most crucial developments in the modern world. The fields of electronics, healthcare and power generation are but a few areas in which the implementation of magnetic materials is widespread. Indeed, society is becoming increasingly reliant on the use of technology based on magnetic concepts, and with consistently increasing demands on the hardware that is present in the everyday electronics we use, there is a constant battle to develop new materials for use in the fabrication of even more efficient devices.

Development of devices for information storage and logical units has been essential to the field of computing, where magnetic materials have proven to be robust and reliable. However, they are not without drawbacks: there are limitations to the size of the magnetic domains used to encode data, which has an impact on the storage densities that can be achieved. This has been somewhat overcome through the changeover from

longitudinal to perpendicular recording media but is nonetheless still a limiting issue [1–3]. In addition, there are also limitations in attainable speeds for switching, which is typically achieved through magnetisation reversal of discrete magnetic domains. As a result, commercial use of magnetic media has so far been limited to permanent data storage, while semiconductor-based devices completely dominate other media such as random-access memory and have recently superseded magnetic media in permanent data storage as well in the form of solid-state drives.

There has been some development of alternative writing methods for magnetic media, such as heat-assisted recording technology. Even still, limitations exist in both achievable switching speed and the yet-finite magnetic domain size attainable without complications arising due to nano-scale effects, such as superparamagnetism [4]. Thus, for magnetic data storage to remain relevant, there needs to be development of both alternative methods to manipulate magnetisation and fabrication of new materials.

1.2 Magneto-optics and ultrafast magnetism

The typical switching rate of metal-oxide-semiconductor field-effect transistors, upon which modern processors and solid-state storage devices are based, is currently on the order of a few GHz. Thus, 500 ps provides the benchmark against which read/write speeds of magnetic media must compete. This could in principle be achieved using light: a typical commercial femtosecond laser system can readily produce laser pulses that are 100 fs in duration, which is of a similar timescale to the interactions which give rise to magnetic ordering [5].

When linearly polarised light passes through a medium in the presence of a magnetic field, the polarisation axis is rotated by an amount proportional to the strength of the field. This discovery was first documented by Michael Faraday in 1845 and is now referred to as the Faraday effect [6]. The physical basis for this will be discussed in

Section 2.3. This is but one branch in a wider-range of optical phenomenon collectively known as magneto-optics (MO), which when combined with femtosecond laser pulses can be used to probe the magnetic properties of a system on ultrafast timescales.

The field of ultrafast magnetism was first pioneered in the 1990s, and with the rapid advancement and increased availability of commercial femtosecond laser systems, has emerged as a vast area of research. Experiments employ a pump-probe scheme, for which a full description will be provided in Section 2.4. In summary, the experiment uses an initial "pump" laser pulse to supply energy to the system under study in order to induce a non-equilibrium state. The evolution of this state can then be characterised using a second "probe" pulse, which arrives at the sample after a finite time delay. Through these means, the dynamics that ensue upon photoexcitation can be investigated.

The first study to apply this technique to a magnetic system on sub-ps timescales was published by Beaurepaire *et al.* in 1996 [7]. In this study, the authors reported their use of time-resolved magneto-optics (TR-MO) to observe demagnetisation of a ferromagnetic Ni film upon irradiation with ultrashort (60 fs) visible wavelength laser pulses. The magnetisation decreased to a minimum within 2 ps before undergoing partial relaxation over the course of 10–15 ps. The electron dynamics were determined by complementary transient transmission measurements which found that there was a sharp increase in transmittance on faster timescales (<260 fs), followed by partial recovery within 8 ps. The clear disparity in the electron and spin dynamics was noted.

The results were explained using a three-temperature model which compartmentalised the total thermal energy of the system within three distinct but coupled "baths" corresponding to electronic, lattice and spin contributions. Each was represented by a different temperature, denoted by T_e, T_l and T_s, respectively. While T_e and T_s were determined experimentally, T_l was inferred from the others based on finite

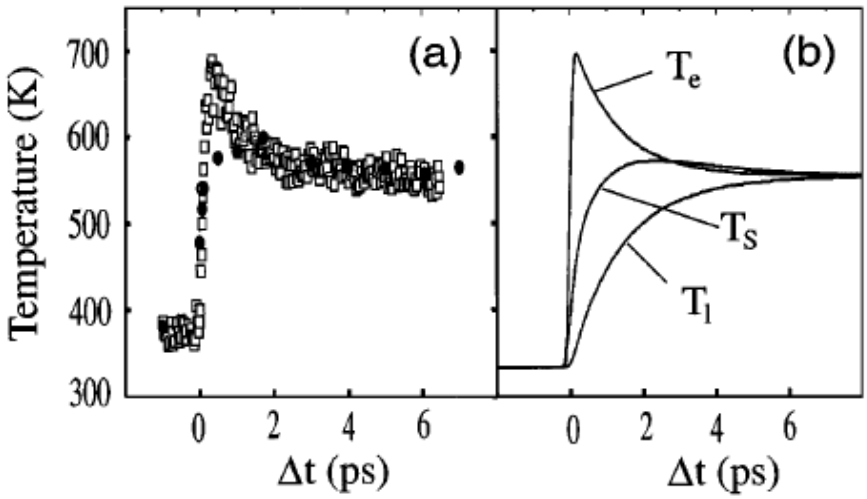

Fig. 1.1 Ultrafast demagnetisation data for a ferromagnetic nickel film. (a) Experimental transient transmittance and TR-MO response induced by an ultrashort laser pulse have been converted used to estimate T_e (hollow squares) and T_s (filled circles). (b) A microscopic three-temperature model was used to fit the data and ascertain the lattice temperature. Taken from [7].

relationships governing redistribution of energy between the three reservoirs. Hence the temporal evolution of temperature for each of the three baths upon optical pumping was determined, as shown in Fig. 1.1. The interpretation of the dynamics was that the laser pulse initially elevated the electron temperature only, in line with the dipole approximation, and generated a non-equilibrium state. Only upon electron–electron scattering events, which facilitate change in spin, was T_s observed to rise as the spin-up and spin-down populations equilibrated and thus magnetisation was lost [7]. Likewise, electron–phonon interaction gave rise to an increase in T_l at an even slower rate.

The work of Beaurepaire and co-workers spawned numerous similar ultrafast studies on a wide range of magnetic materials — from metals to semiconductors and insulators — for which perturbation of magnetic order was achieved through a thermal mechanism. However, it must be noted that these processes are both temporally and energetically inefficient. As illustrated by the Ni study, the timescales for magnetisation dynamics induced in this way are limited by the rate at which thermal energy can be exchanged

between the electron and spin reservoirs, which is inherently slow compared to the rate at which the hot electrons themselves are generated. Likewise, the direction of energy flow following optical pumping in this scheme is completely untargeted: in addition to elevation of T_s through electron-spin coupling, T_l will also increase through electron-phonon coupling and thus energy will be lost as heat. Therefore, an alternative mechanism for perturbation of magnetic properties is necessary to make use of the polarisation of light.

Photomagnetism is a phenomenon whereby the magnetic properties of a material can be manipulated by resonant pumping of specific spectroscopic transitions to alter its spin properties or structure. As such, it is typically dependent on both pump wavelength and polarisation, affording further degrees of freedom with which to control magnetisation. This has been demonstrated in ferrimagnetic garnets by Hansteen *et al.* [8], the results of which are summarised in Fig. 1.2. Upon pumping spin-forbidden d–d transitions, they observed oscillatory features in the TR-MO traces. This was attributed to creation of a photoinduced anisotropy field, $\delta\boldsymbol{H}^\mathrm{a}$, by optical pumping, which acts to tilt the effective magnetic field, $\boldsymbol{H}'_\mathrm{eff}$, away from its equilibrium position. Magnetisation, $\boldsymbol{M}$, then precesses about this axis, giving rise to TR-MO amplitude that scales with M_z, where z is the axis along which the probe beam propagates. Changing the angle that the electric field of the linearly polarised pump forms with respect to the [100] axis of the material, θ, was found to change the amplitude of the oscillations in the TR-MO response. This discounted a thermal effect as being the sole cause of precession.

Further studies have demonstrated that all-optical control of magnetisation is not limited to producing just short-lived transient effects. Stupakiewicz *et al.* have demonstrated non-thermal magnetisation reversal in Co-doped yttrium iron garnet (YIG:Co), again through resonant pumping of d–d transitions using ultrashort laser

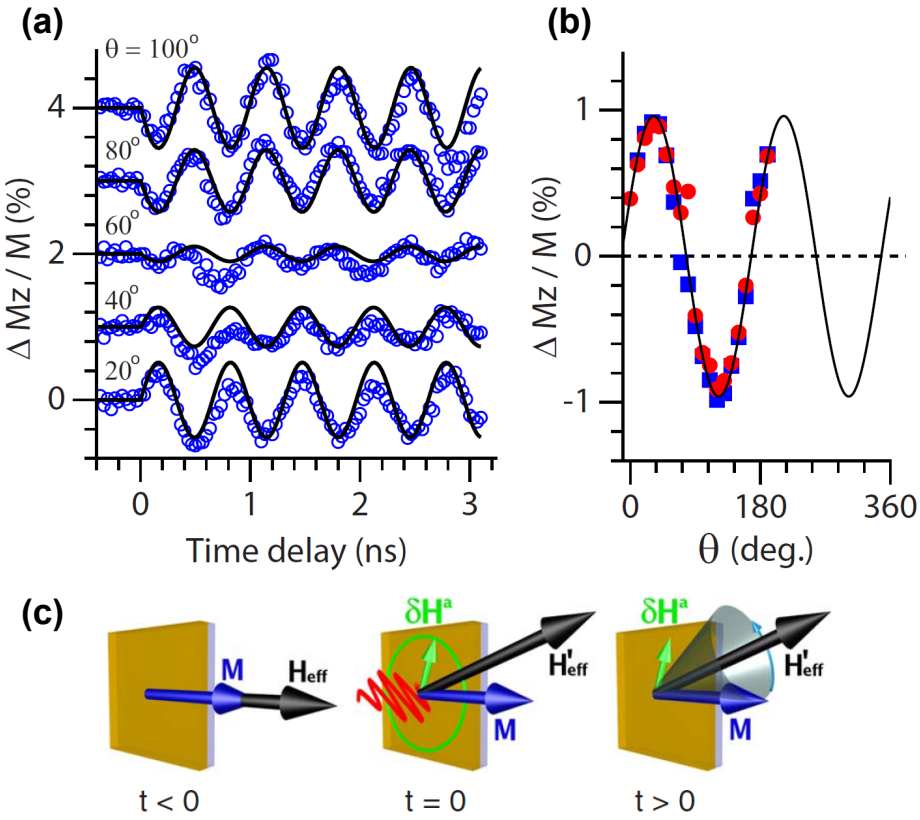

Fig. 1.2 Coherent magnetisation precession observed in a photoexcited ferrimagnetic garnet film. (a) Oscillations in the TR-MO response observed upon excitation with a near-infrared (NIR) pump. (b) Oscillation amplitude-dependence on the angle that the pump pulse's electric field forms with the material's [100] axis, θ. (c) Schematic illustrating the contribution of different magnetic field components that give rise to the precession dynamics. $\boldsymbol{M}$ and $\boldsymbol{H}_{\text{eff}}$ both lie parallel in their equilibrium state ($t < 0$). Upon photoexcitation, $\delta\boldsymbol{H}^{\text{a}}$ is induced by the pump, which acts to tilt $\boldsymbol{H}'_{\text{eff}}$ away from its equilibrium position ($t = 0$). $\boldsymbol{M}$ then precesses about this axis for several ns ($t > 0$). Taken from [8].

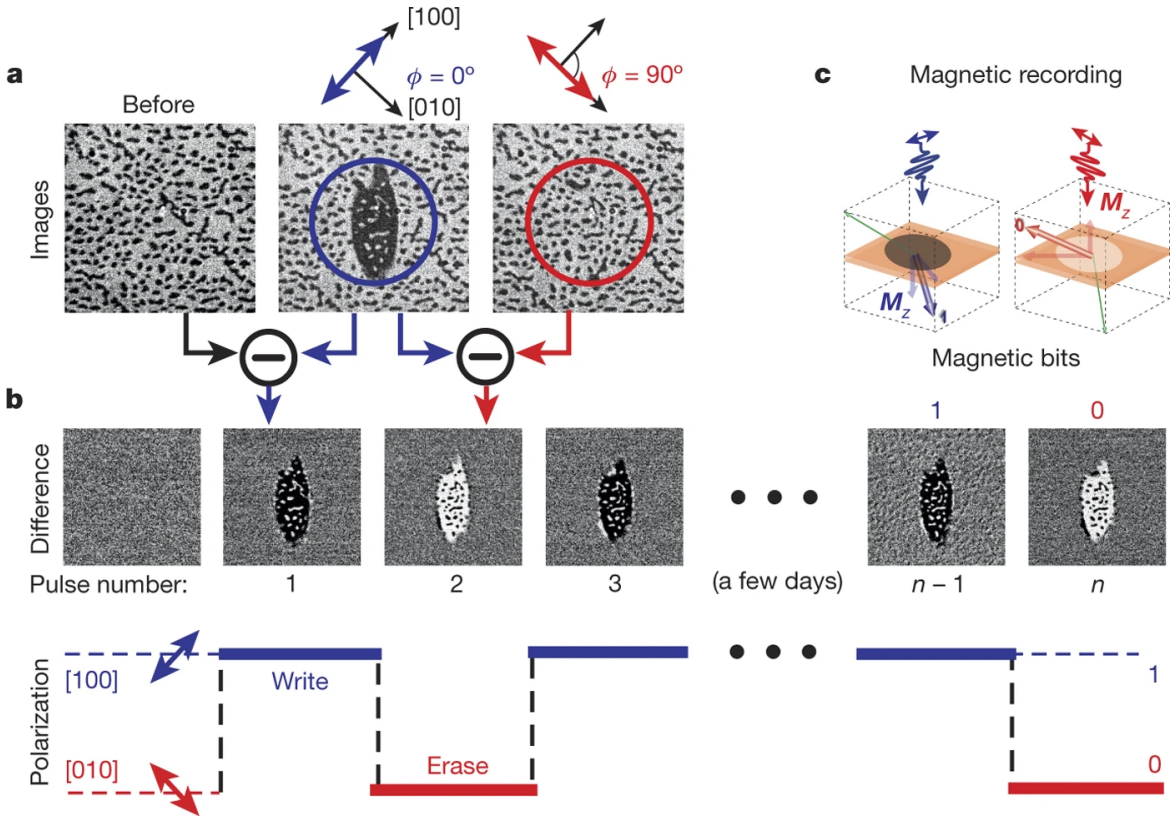

Fig. 1.3 Overview of the "writing" process for YIG:Co enabled by photoexcitation. **a** Optical pumping using 40 fs-duration laser pulses of different polarisation with respect to crystallographic planes induces formation ($\phi = 0°$) or elimination ($\phi = 90°$) of magnetic domains. This is represented by the dark elliptical feature, as observed through magneto-optical imaging of a 200×200 µm region. **b** Difference images taken between writing and erasing steps can represent the formation of two magnetic states, analogous to binary bits. This represents the basis of the magnetic recording scheme shown in **c**. Taken from [9].

pulses [9]. This scheme is illustrated in Fig. 1.3. As observed through MO imaging, a domain with a particular magnetisation direction could be created using a single laser pulse with polarisation parallel to the [100] axis of the material. Pumping this domain with laser pulses of perpendicular polarisation could then reverse magnetisation back to its original state. Through TR-MO imaging, it was found that generation of domains in this way could take up to 60 ps, and at ambient conditions were stable for days. The authors concluded that the single domain can effectively form a "bit" of magnetic memory which can be read/written to on ultrafast timescales.

The outcome of this study amply demonstrates how the use of all-optical pump–probe schemes could address the issue of slower switching speeds in magnetic media. However, one issue that persists is the finite size of magnetic domains in conventional metallic/semiconductor materials, which imposes limits for achieving higher storage density. It is also not trivial to modify the structure or composition of these materials to tailor them for desired optical and magnetic characteristics. The use of molecular-based magnets, for which physical properties are readily tuneable at the atomic (as opposed to microscopic) scale, may provide materials that could address these shortcomings and thus are interesting candidates for study.

1.3 Molecule-based magnetic materials

There are a variety of materials consisting of molecular assemblies that exhibit magnetic behaviour. These typically employ paramagnetic metal ions coordinated to a variety of suitable ligands, which vary in complexity and size. Use of these molecule-based magnets provides some profound advantages over traditional metallic alloy-based materials [10]. The synthesis is often rather facile in comparison to alloy or metal oxide-based materials: molecular materials are often highly soluble, which enables room-temperature solution-based processing, such as electrodeposition or simply layer-by-layer deposition [11]. In the case of alloys, energy intensive processes such as magnetron sputtering are usually necessary for deposition of thin layers onto other substrates. Thus, the production of molecule-based materials has obvious benefits in terms of reduced environmental impact and capital expense.

Chemical flexibility is another advantage; simple substitution of metal cations or ligands can result in vastly different properties, whether that be magnetic or optical. This allows for the rational design of a material that possesses specific characteristics, such as a specific colour or enhanced critical temperature for magnetic ordering, T_c.

Indeed, the optical properties of these materials also open another avenue to explore, which is modulation of magnetic ordering through photoexcitation. Molecular materials boast enhanced transparency over metallic materials, and photoexcitation can occur in these materials that is resonant with specific transitions, each of which may exhibit their own electronic and spin dynamics. This allows for finer control over the magnetic properties.

1.4 Prussian blue and its analogues

Prussian blue is an inorganic coordination polymer of historic significance. Well-known for its vivid blue colour, it has found widespread use in paints and dyes since the early 18th century. It exists as a networked solid conforming to the face-centred cubic lattice structure at the microscopic level. Its molecular formula is $Fe_4[Fe(CN)_6]_3$; Fe cations exist in both the +3 and +2 oxidation states, and are arranged in an alternating fashion, being bridged by ambidentate cyanide ligands. The mixed-valence nature of the material enables intense metal–metal charge transfer (MM′CT) transitions to occur between Fe(II) and Fe(III) when irradiated with red light, which gives rise to its strong colour [12].

Beyond providing a striking colour for various works of art, studies conducted on this material over the course of the last century have found that it is in possession of interesting magnetic properties; it was observed over 90 years ago to be paramagnetic at room temperature [13], while temperature-dependent measurements using Mössbauer spectroscopy and neutron scattering revealed that a ferromagnetic phase transition occurs at around 5.5 K [14, 15]. This results from spin-ordering of the Fe(III) cations, which are high-spin (N-coordinated; $S = 5/2$), while the Fe(II) ions are low-spin (C-coordinated; $S = 0$) and do not directly contribute.

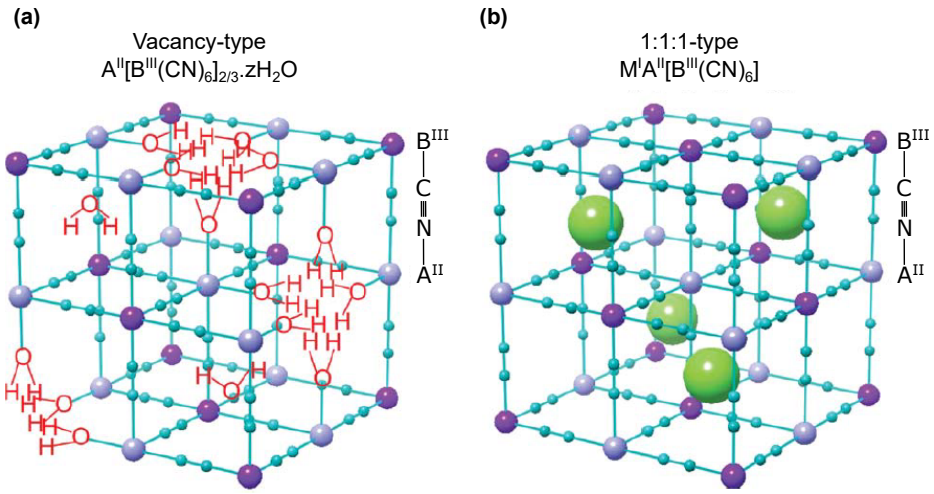

Fig. 1.4 Schematic of the two idealised lattice structures found in PBAs, which both afford different mechanisms for charge balance. (a) The vacancy-type lattice, where vacant $[B^{III}(CN)_6]^{3-}$ sites are occupied by H_2O coordinated to the nearest neighbours, maintaining octahedral coordination spheres. (b) The interstitial cation-type lattice, with intercalated M^+ in alternating tetrahedral holes. Taken from [17].

There exists an array of similar materials that are collectively referred to as Prussian blue analogues (PBAs). These are obtained through replacement of either one or both of the metal cations present in Prussian blue, typically conforming to one of two formulae for bimetallic or mixed-valence PBAs: $A^{II}[B^{III}(CN)_6]_{2/3} \cdot z\,H_2O$ or $M^IA^{II}[B^{III}(CN)_6]$, where A and B are transition metal (TM) cations [16, 17]. Charge balance is achieved in each of these scenarios through different means: the former possesses vacant sites where $[B^{III}(CN)_6]^{3-}$ is instead replaced by uncharged H_2O ligands bound to the empty A coordination sites, while the monovalent alkali cation M^I is inserted into interstitial lattice sites in the latter [16, 17]. These two idealised structures are shown in Fig. 1.4. It should be noted that zeolitic H_2O (i.e. non-coordinated and able to diffuse through the lattice) may also be present within the interstitial sites of the material [16–18].

Different PBA materials can exhibit vastly different spectral properties; like Prussian blue itself, these also arise due to the intense MM′CT transition between the TM cations present and the colour of said transitions can be tuned through careful selection

of the species to incorporate, as well as their stoichiometric ratio. Likewise, adjustments to material composition can also be used to fine-tune the magnetic-ordering behaviour throughout the material, which varies greatly across the different PBAs.

In many materials, magnetic ordering is enabled either through weak dipolar interactions or much stronger exchange interactions between distinct sources of magnetic moment. In the latter case, the magnetic exchange Hamiltonian, $\hat{H}$, for any pair of interacting spins, A and B, is described by:

$$\hat{H} = -J_{\mathrm{AB}}\hat{S}_{\mathrm{A}} \cdot \hat{S}_{\mathrm{B}} \tag{1.1}$$

where $\hat{S}_{\mathrm{A}}$ and $\hat{S}_{\mathrm{B}}$ are the respective spin operators for A and B, while J_{AB} quantifies the strength of the interaction. In a system comprising multiple distinct interactions, $\hat{H}$ is described by the sum of each pairwise exchange term.

Direct exchange interactions are observed when A and B are in close enough proximity for coupling effects to be observed. However, this is inadequate to explain the magnetic ordering observed in Prussian blue and its analogues, given that the distance between the magnetic centres is on the order of several Å. Thus, the alternative explanation for this is the existence of a magnetic superexchange interaction (SEI) between linked metal cations *via* the bridging cyanide ligands. This arises in PBAs as a result of π-backbonding interactions between d-orbitals of the two linked metal cations and the π*-orbitals of the cyanide linkers, which allows for partial electron delocalisation across the ligand [16]. This is illustrated in Fig. 1.5.

Here, it is shown that orbital overlap plays a crucial role in determining the nature of the interaction: if the two magnetic orbitals from A and B are of the same symmetry (for example, both t_{2g}), then the two spins are coupled antiferromagnetically to satisfy the Pauli exclusion principle, which prohibits electrons of identical spin from occupying the same volume in space. This is termed kinetic exchange ($J_{\mathrm{KE}} < 0$). If the two

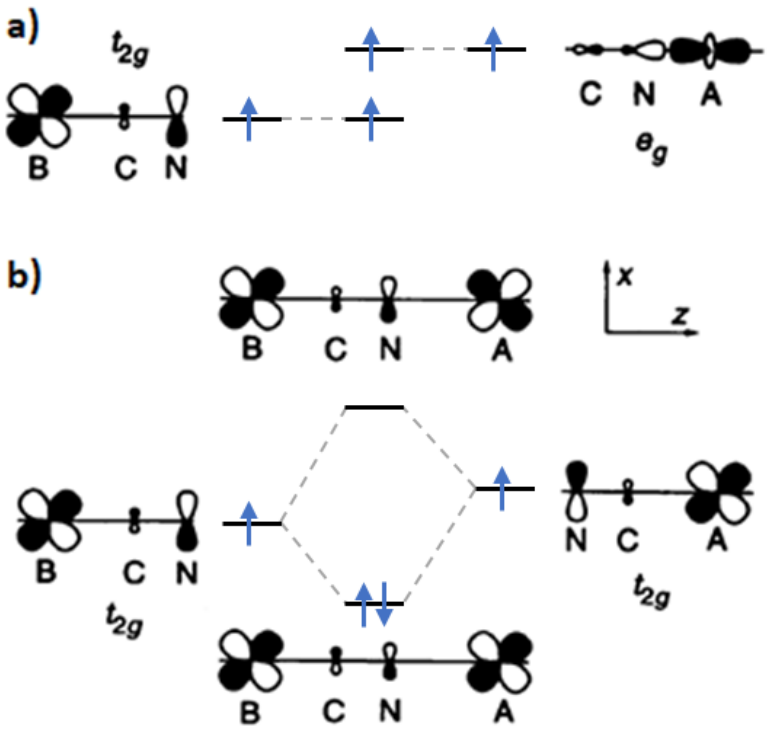

Fig. 1.5 Schematic of the SEI that takes place in PBAs. a) The interacting metal d-orbitals are of different symmetry and cannot undergo interference, resulting in parallel spin alignment and thus ferromagnetic coupling. b) Like-symmetry classification of the interacting d-orbitals allows overlap to form formal bonding interactions across the CN^- bridge, resulting in antiferromagnetic coupling. Adapted from [19].

interacting magnetic orbitals from A and B possess orthogonal symmetry (i.e. one is e_g, the other t_{2g}), then the overlap integral is zero; parallel alignment of spins is favoured to minimise energy as per Hund's rule, leading to ferromagnetic coupling. This is known as potential exchange ($J_{PE} > 0$). Magnetic ordering throughout the PBA in question results from summation of these pairwise interactions ($J = J_{KE} + J_{PE}$), which may or may not both be present; the sign of the overall exchange parameter J determines which type of magnetic ordering is observed between spin centres. The tendency is for antiferromagnetic coupling to be favoured ($|J_{KE}| > J_{PE}$), which results in many PBAs possessing ferrimagnetic characteristics due to the uncompensated spins (i.e. $S_A \neq S_B$). Given the consistency of the cubic lattice structure across different analogues, the nature of the magnetic ordering for any given PBA can be predicted through d-orbital overlap and electron configuration arguments.

Using J, the T_c for a given system can be predicted by [16, 20]:

$$T_c = \sqrt{Z_A Z_B}|J_{AB}|\sqrt{S_A(S_A+1)S_B(S_B+1)}/3k_B \tag{1.2}$$

where Z_A and Z_B represent the number of magnetic neighbours of A and B, respectively, and k_B is Boltzmann's constant. Thus, in addition to the magnitude of the SEI, T_c is also affected by the stoichiometry of A and B as well as their associated spin values.

With this in mind, a variety of PBAs have been constructed with varying values for T_c and computed J; $Mn^{II}[Mn^{IV}(CN)_6]\cdot z\,H_2O$ (T_c = 47.8 K; ferrimagnetic) [21], $Cs^{I}Mn^{II}[Cr^{III}(CN)_6]\cdot 1\,H_2O$ (T_c = 90 K; ferrimagnetic, $J = -18$ cm^{-1}) [20, 22], and $Cs^{I}Ni^{II}[Cr^{III}(CN)_6]\cdot 2\,H_2O$ (T_c = 90 K; ferromagnetic, $J = +28$ cm^{-1}) [20, 23], to name a few. It was remarked by Gadet and co-workers that the use of chromicyanide anions ($[Cr^{III}(CN)_6]^{3-}$) had been shown to exhibit enhanced T_c in comparison to ferricyanide ($[Fe^{III}(CN)_6]^{3-}$) [19, 23]. This is on account of the d^3-configuration providing the highest possible spin ($S = 3/2$) in this strong ligand-field environment and providing spin-

density in three dimensions [16, 24], which spurred the design and synthesis of PBAs using this molecular-based building block. This resulted in PBAs with greatly enhanced critical temperatures, such as mixed-valence $Cr^{II}{}_3[Cr^{III}(CN)_6]_2 \cdot 10\,H_2O$ ($T_c = 240$ K; ferrimagnetic, $J = -70$ cm^{-1}) [19, 20] and $V^{II/III}[Cr^{III}(CN)_6]_{0.86} \cdot 2.8H_2O$ ($T_c = 315$ K; ferrimagnetic, $J = -241$ cm^{-1}) [20, 25], the latter of which was hailed as being a "room-temperature organometallic magnet" that may have applications at ambient conditions.

1.5 Photomagnetism in Co–Fe Prussian blue analogue

As well as chemical tunability of their spectral and magnetic properties, some PBAs have also been shown to exhibit photomagnetic behaviour; irradiation with light results in a change in spin configuration of the metal cations, which alters the SEI and thus the macroscopic magnetic properties observed.

Much of the work of Sato *et al.* has focussed on materials of this nature, with an early study carried out on a powder of Co–Fe PBA ($K_{0.2}Co_{1.4}[Fe(CN)_6] \cdot 6.9H_2O$) [26]. Their experiments used light guided by an optical fibre into a superconducting quantum interference device (SQUID) magnetometer, which provided magnetic characterisation. It was observed that irradiation of the PBA by red light resulted in an increase of magnetisation (Fig. 1.6(a)), while subsequent irradiation with blue light or thermal treatment could mostly undo the change in magnetic properties. Additional experiments which irradiated the sample sequentially with red and blue light demonstrated that the process could be cycled a number of times (Fig. 1.6(b)), although the net increase in magnetisation observed after each repetition suggests that the photomagnetic switching process was not fully reversible.

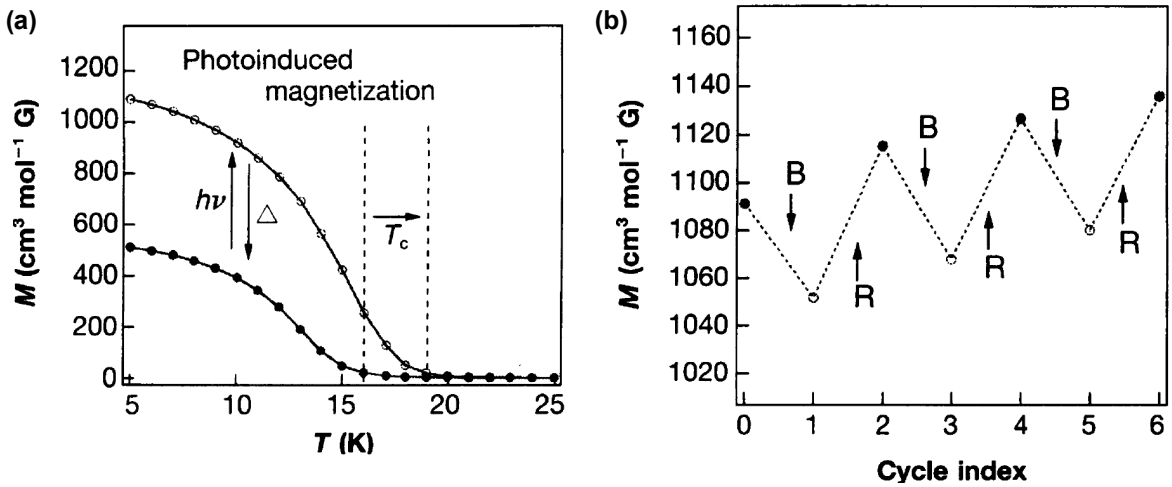

Fig. 1.6 Plots of magnetisation observed in photoactive Co-Fe PBA. (a) Field-cooled magnetisation curves obtained for the non-irradiated and photoexcited material; note that the photomagnetic phase transition is reversed upon application of heat. (b) Magnetisation data obtained upon cycling irradiation with blue (450 nm, B) and red (660 nm, R) light, highlighting the reversibility of the process. Taken from [26].

The findings of the Co–Fe PBA study were significant for their demonstration of photo-switchable magnetisation in a molecular-based material whose effects persisted far beyond the illumination time. Further studies used similar Co–Fe PBA materials with higher K^+ content or incorporated Rb^+ for charge balance instead [27, 28], both of which exhibited near-zero magnetisation in field-cooled magnetisation curves. This indicated that the material possessed a completely diamagnetic ground state, which could then undergo transition to a metastable ferrimagnetic state upon irradiation with visible light. The process was attributed to MM′CT between Fe^{II} ($S = 0$) and low-spin (LS) Co^{III}_{LS} ($S = 0$) to produce Fe^{III} ($S = 1/2$) and high-spin (HS) Co^{II}_{HS} ($S = 3/2$), which was termed a photoinduced phase transition. Spectroscopic data showed that while the original MM′CT is suppressed in the ferrimagnetic phase, additional peaks in the visible and NIR could be observed; these were ascribed to Co^{II}_{HS} d–d transitions [27, 28]. Any photoinduced change in either the magnetic and spectral properties could be reversed upon heating the sample to 120 K, consistent with there being a small potential energy barrier between the ferrimagnetic and diamagnetic states and thus accounting for the

stability of the former at low temperature [28]. The authors highlighted the small energy separation between the two states and suggested that interconversion may occur with slight changes to the ligand-field environment of Co-sites [28], which may explain the outcome of their previous studies where irradiation of the ferrimagnetic phase with blue or NIR light would induce transition back to the diamagnetic state [26, 27].

The dynamics associated with the photomagnetic phase transition in Co–Fe PBA have been the subject of numerous studies [29–32]. These concluded that conversion of Co^{III}_{LS} ($t_{2g}{}^6e_g{}^0$) to Co^{II}_{HS} ($t_{2g}{}^5e_g{}^2$) occurs upon photoexcitation with visible light on ultrafast timescales (<100 ps). This is accompanied by lattice expansion, which was attributed to the population of antibonding e_g orbitals on the Co-sites which act to increase the length of Co–N bonds [30, 31]. While consistent with spectroscopic assignment of a direct MM′CT combined with a Co-based spin rearrangement, Cammarata and co-workers proposed a different mechanism for the electron transfer process: that photoexcitation in the first instance induces a d–d transition on Co^{III}_{LS} which ultimately relaxes to form the MM′CT state comprising Co^{II}_{HS} and Fe^{III}_{LS} [32]. They suggested that this proceeded *via* the scheme illustrated in Fig. 1.7. In summary, photoexcitation of a Co^{III}_{LS}-centred transition initially populates the e_g sublevel, which results in expansion of the Co-site coordination sphere. While the energy of the t_{2g} sublevel in this state is largely unchanged, the e_g sublevel itself is stabilised by the decreased Co/N orbital overlap and thus the ligand-field splitting is reduced. This provides the driving force for spin crossover (SCO) from LS → HS, after which MM′CT from Fe^{II} to Co^{III}_{HS} occurs. The authors' interpretation was confirmed using ultrafast X-ray absorption experiments, which could provide elemental-specific information and thus a present a clearer picture as to the localisation of any observed dynamics. Upon comparison of kinetic data pertaining to Co- and Fe-sites, they observed an additional decay component (50 fs) that was exclusive to the former, while two others (200 and 450 fs)

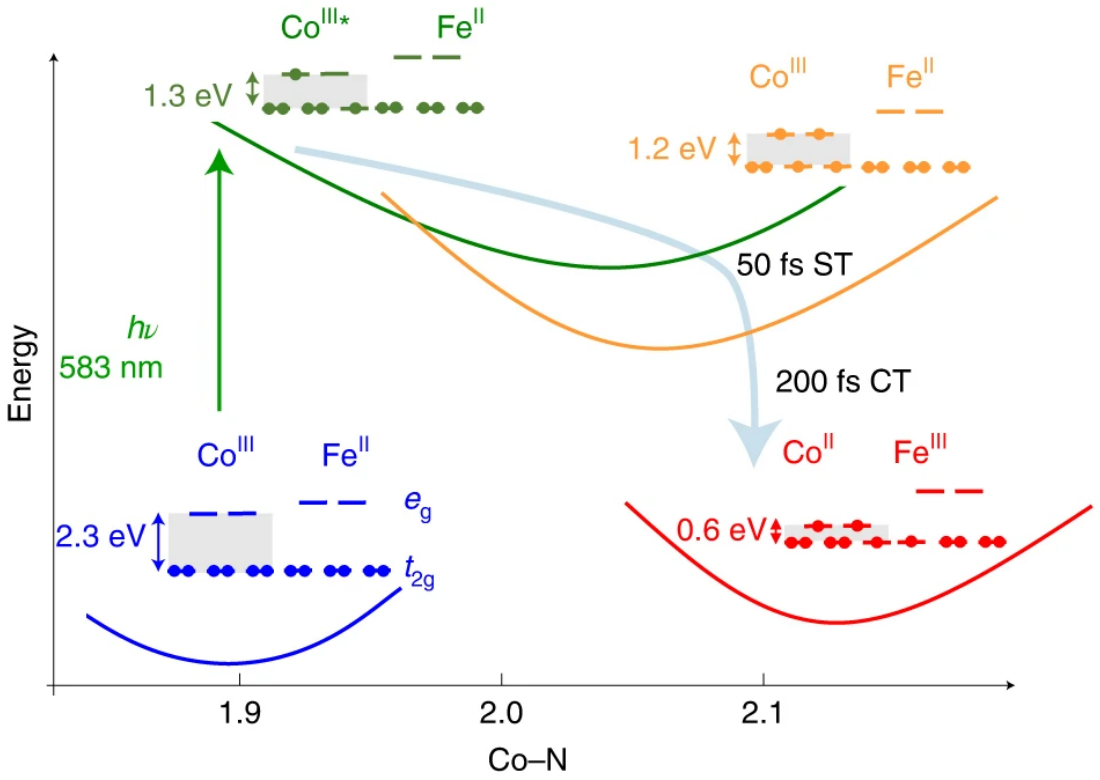

Fig. 1.7 1D potential energy surfaces along the Co – N coordinate for the relevant states involved in the MM′CT process in in Co–Fe PBA. Franck-Condon excitation of the diamagnetic ground state (blue) populates metal-centred excited state (green). The repulsive surface drives elongation of Co – N bonds, which is followed by Co spin transition (ST) to a paramagnetic excited state (yellow). This is followed by charge transfer (CT) from Fe^{II} to Co^{III} (red). Taken from [32].

were common between both metals. The faster decay was attributed to Co-SCO, while complementary experiments indicated that the MM′CT occurred on longer timescales.

The investigations into the photomagnetic behaviour observed in Co–Fe PBA discussed so far serve to demonstrate the rich and diverse photophysics that can be found within just one PBA and highlight the necessity of complementary techniques and analyses to build a comprehensive model of how electronic structure and magnetic behaviour are influenced by light in photomagnetic materials.

1.6 Photophysics of Cr(III)-based systems

As discussed in Section 1.4, some Cr(III)-based PBAs have been shown to exhibit higher T_c than many other PBAs. As such, magnetic ordering can be readily achieved upon cooling with liquid N_2, making them amenable to study using MO.

The first working laser, based on synthetic ruby (Al_2O_3:Cr), was reported in 1960 [33]. The Cr(III) dopant was key to the light emission mechanism, which is not just limited to solid-state materials but also observed in Cr(III)-based complexes. As such, the photophysics for Cr(III)-based systems have since been extensively investigated and have featured in a number of reviews [34–37].

Understanding the photophysics of any system requires consideration of its electronic structure: the electronic states it possesses, their energetic ordering and their associated spin multiplicities. For octahedral Cr(III) complexes, this is summarised for metal-centred states by the d^3 Tanabe–Sugano diagram, provided in Fig. 1.8. This plots the energy, E, of different electronic states with respect to ligand-field splitting parameter, Δ. As interelectronic repulsion is what gives rise to the dependence of a given state's energy on ligand-field splitting, both E and Δ are represented in terms of the Racah parameter B, which is a measure of this repulsion.

Fig. 1.8 reveals a monodegenerate quartet ground state ($^4A_2$) is observed for d^3 systems. The presence of three quartet excited states ($^4T_2$, $^4T_1$ and $^4T_1$) indicate that three Laporte-forbidden d–d transitions may be observed, although the third is much more energetic and likely to overlap with charge transfer bands. For intermediate/strong Δ, the spin-flipped ^2E and $^2T_2$ states are the lowest lying excited states, and lie close enough together such that the energy separation is accessible with thermal energy. Thus, these are frequently considered together and denoted in the singular ^2E term. As direct transitions to the doublet manifold from the ground state are spin-forbidden, they are usually accessed *via* intersystem crossing (ISC) from photoexcited ligand-field

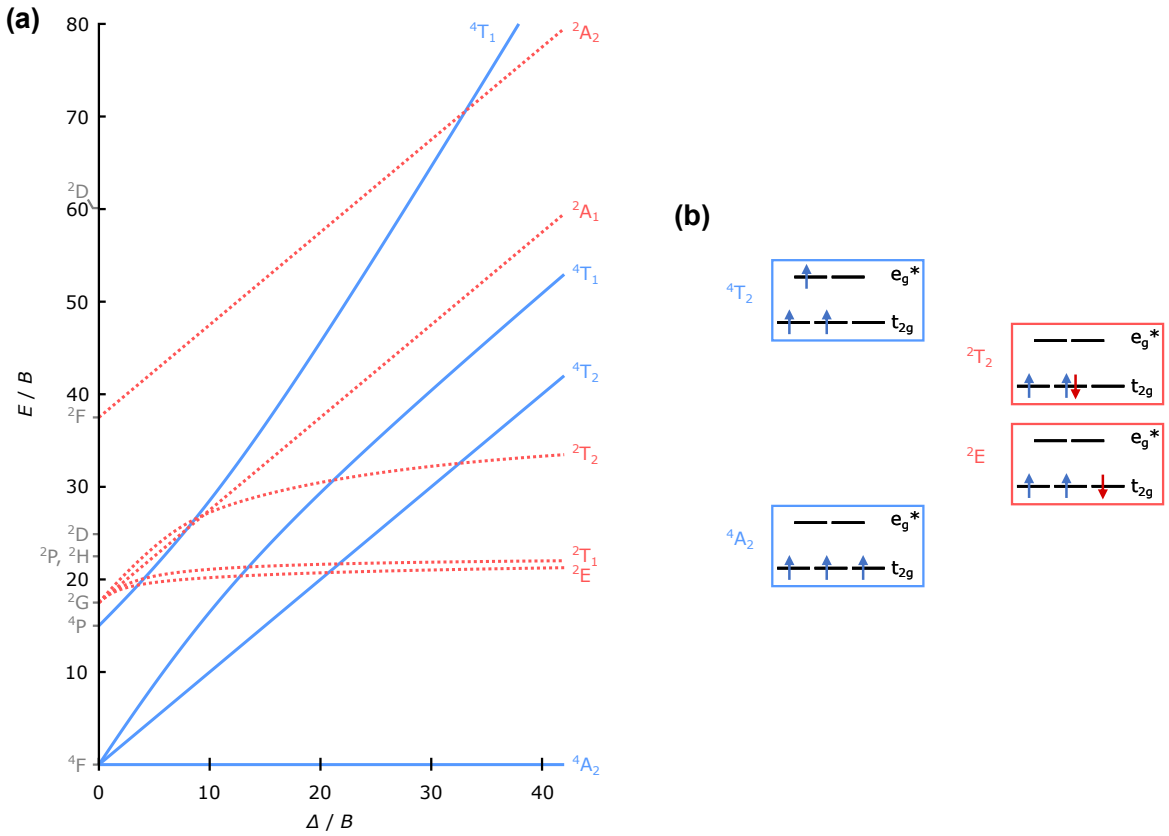

Fig. 1.8 Electronic structure summarised for octahedral Cr(III) complexes. (a) Tanabe–Sugano diagram for d^3 electron configuration when Racah parameter $C = 4.5B$. Quartet states ($S = 3/2$) are coloured blue, doublet states ($S = 1/2$) are coloured red. (b) Individual electron configurations for the ground state ($^4A_2$) and lowest lying quartet ($^4T_2$) and doublet (^2E and $^2T_2$) excited states. Methodology used to reproduce (a) first reported in [38].

or charge-transfer states. Likewise, relaxation from the doublet manifold back to the ground state is also a spin-forbidden process; in the absence of non-radiative relaxation pathways, this results in extended doublet state lifetimes. This gives rise to the photoluminescence for which Cr(III) complexes are well-known.

Quartet–doublet ISC efficiencies for Cr(III) complexes can range between 0.5–1, with greater values afforded by systems for which the $^4T_2$–^2E energy separation is low [39]. $Cr(acac)_3$ is one of such systems. Juban and McCusker have studied the dynamics associated with population of the doublet manifold in this complex using ultrafast transient absorption (TA) measurements [40]. Upon photoexcitation of the $^4T_2 \leftarrow {}^4A_2$ transition, they concluded that the doublet manifold is populated within the time resolution of their experiments (<100 fs), while the timescale for ground state recovery was determined to be ∼700 ps. Optical pumping of the lowest ligand–metal charge transfer (LMCT) transition resulted in similar behaviour, with a key difference being that a fast component to the dynamics (50 fs) is also observed. This was attributed to $^4\text{LMCT} \xrightarrow{\text{ISC}} {}^2E$.

In summary, Cr(III) photophysics is characterised by the presence of low-lying spin-flipped doublet states which can be accessed indirectly through first populating spin-allowed states which then undergo rapid and efficient ISC. Thus, this could provide the means for optical control of macroscopic magnetic properties in Cr(III)-based PBA through perturbation of spins on localised Cr(III) sites.

1.7 Charge and magnetisation dynamics in V–Cr Prussian blue analogue

While there have been various studies focussed on the ultrafast dynamics of discrete Cr(III) complexes in solution, publications that extend this to extended molecular-based solid systems are sparse. The work of Johansson *et al.* sought to fill this void through study of electronic and spin dynamics within V–Cr PBA [41], which was previously highlighted for possessing a T_c above room-temperature. This, in conjunction with an intense MM′CT band in the visible and well-characterised MO spectra [24, 42, 43], made it well-suited for all-optical TR-MO measurements.

Experiments involved complementary transient transmittance (TT) and TR-MO measurements to provide information on both electronic and spin dynamics. Optical pumping of the LMCT transition at 400 nm was found to transiently reduce Cr(III) before ISC to the ^{2}E state on timescales faster than the experimental time resolution (< 250 fs). This concurred with the work of Juban and McCusker on Cr(acac)$_3$ [40]. A sharp change in the magnetisation on the same timescales was observed through complementary TR-MO measurements, as shown in Fig. 1.9(a). This was attributed to alteration of the SEI — and thus magnetic ordering — through change in the spin-state on the Cr(III) sites (Fig. 1.9(b)). Both the TT and TR-MO response were observed to decay exponentially with similar time constants ($\tau_{\mathrm{TT}} = 0.76$ vs. $\tau_{\mathrm{TRMO}} = 0.64$ ps at $T = 50$ K). These were also similar to what was observed in Cr(acac)$_3$, which had been attributed to vibrational cooling [40].

The work of Johansson *et al.* is notable as it acted as a proof of concept for the application of ultrafast TR-MO measurements to probe the magnetisation, and hence spin, dynamics in molecular-based systems. While there are numerous examples of pump–probe studies that have investigated the ultrafast electronic and lattice dynamics

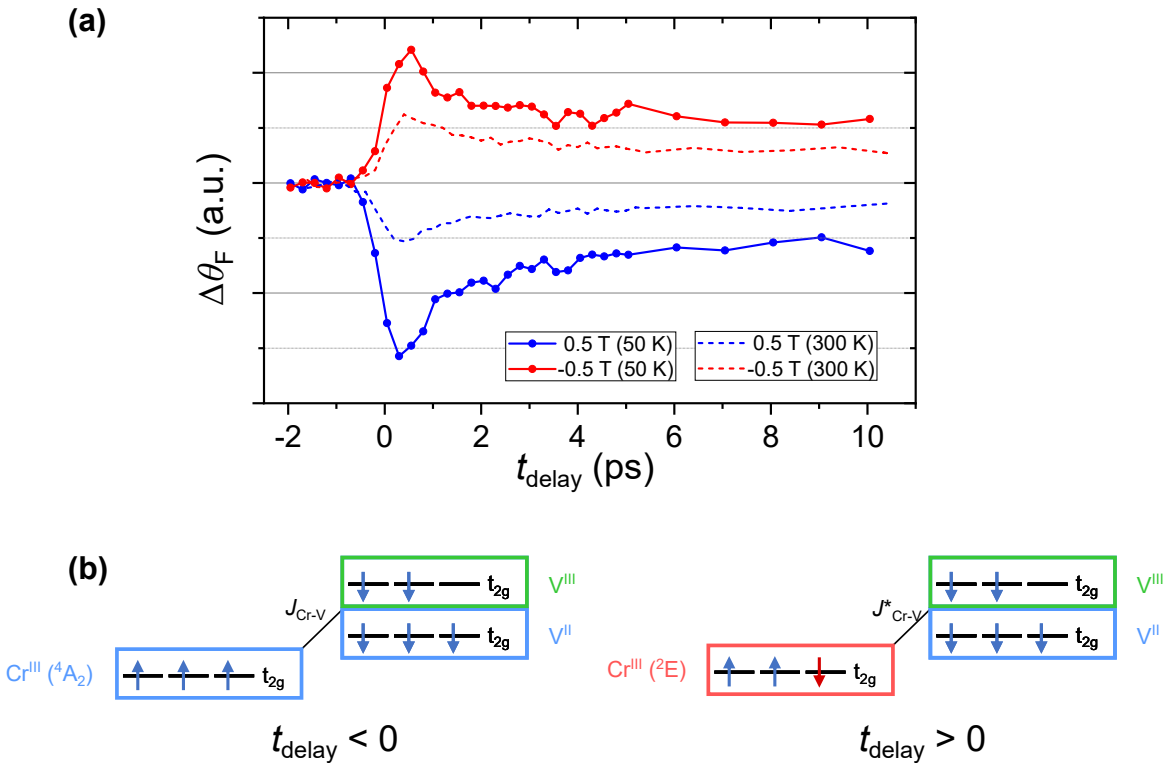

Fig. 1.9 Overview of magnetisation dynamics observed in V–Cr PBA. (a) TR-MO traces obtained at different temperatures and applied magnetic fields upon photoexcitation of the LMCT at 400 nm. Data were obtained using a probe wavelength of 660 nm. (b) Scheme of how spin configuration changes following optical pumping, thus perturbing the SEI, $J_{\mathrm{Cr-V}}$. Adapted from [41].

of PBAs in various forms [29–32, 44–46], investigations of these materials using ultrafast TR-MO is still underreported.

1.8 Aims

The primary goal of the work reported in this thesis was to extend the use of all-optical TA and TR-MO to other PBAs to build a comprehensive picture of the electronic and magnetisation dynamics in this class of materials. For this purpose, mixed-valence Cr–Cr PBA has been selected for study: a material in which A-sites are predominantly Cr^{II} while B-sites are a mixture of Cr^{III} and Cr^{II}. Due to the different electronic configuration of Cr^{II} compared to V^{II}, the MM′CT and SEI for this material are different to those observed in V–Cr PBA. Nevertheless, both possess the same $[Cr(CN)_6]^{3-}$ backbone and thus photoexcitation in Cr–Cr PBA should provide useful insight into what influence the A^{II} sites have on the dynamics. Complementary to this is the TA study of $[Cr(CN)_6]^{3-}$ itself in solution, with the goal of using the dynamical behaviour observed to inform the models applied to ultrafast experiments on the two PBAs.

The use of transmission-based MO techniques necessitates the study of PBAs in the form of a thin film to enable measurement of bulk properties while ensuring maximum transmittance. However, the polycrystalline morphology and heterogeneity of the films themselves still give rise to immense scatter which acts to depolarise transmitted light and hinders MO measurements. A secondary objective of this work was to present new ways to mitigate these effects (both procedural and in film preparation), which until now have been the primary obstacle in our group's optical measurements. These efforts have focussed on films of Cr–Cr and Fe^{II}–Cr^{III} PBAs.

Chapter 2

Methods

This chapter details the methods used to synthesise, characterise and investigate photoinduced dynamics of PBA thin films used in the work reported throughout this thesis. As such, some of the data used to exemplify the characterisation of said samples have already been published [47].

2.1 Preparation of Prussian blue analogues

As previously outlined in Chapter 1, the molecular-based nature of PBAs enable relatively facile, solution-based procedures for their synthesis to be employed. To facilitate the optical methods used to probe their electronic and magnetic properties, Cr–Cr and Fe–Cr PBAs were produced in the form of thin films on transparent substrates. For the projects discussed, this was achieved through electrodeposition.

2.1.1 Electrodeposition of thin films

The electrodeposition procedure involved the formation of a PBA thin film on a transparent conductive substrate using an electrochemical cell charged with aqueous solutions, and closely followed procedures reported previously [48–53]. The advantage

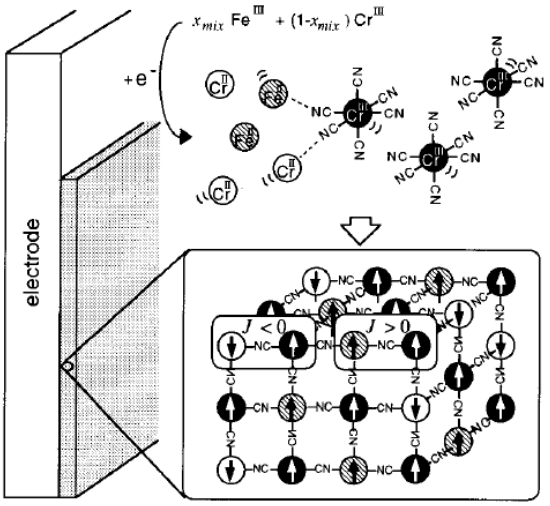

Fig. 2.1 Diagram portraying the formation of a PBA thin film on a conductive substrate. First, electrochemical reduction of TM cations takes place at the surface. Self-assembly then occurs where $[Cr(CN)_6]^{3-}$ coordinates to the reduced metal cations, resulting in nucleation and growth of film. Example shown is for a ternary PBA containing Fe^{II}, Cr^{II} and Cr^{III}. Taken from [54].

of this approach is that the growth of the PBA film can be well-controlled through alteration of parameters such as applied potential and deposition time. For the same reasons, this method allows for finer control of stoichiometric ratios and interstitial cation insertion, which cannot be so easily manipulated through other means.

Syntheses typically conformed to a standard procedure, with minimal alterations for the deposition of different PBA films. A three-electrode system was used, comprising a conductive substrate to act as a working electrode (WE), a counter electrode (CE) to allow for passage of current to the WE, and a reference electrode (RE) against which a potential was applied to the WE. The cell was charged with aqueous solutions of $K[Cr(CN)_6]$, a chloride salt containing the desired TM cation A in its +3 oxidation state, and KCl in large excess as an electrolyte. A^{III} underwent reduction to A^{II} at the WE and adhered to the substrate, upon which self-assembly of the insoluble PBA occurred at the surface through successive coordination of $[Cr(CN)_6]^{3-}$ anions and further reduced metal cations. A schematic of the process is provided in Fig. 2.1.

A potentiostatic (i.e. fixed applied potential, E) method was used for film deposition to enable greater control over the chemical potential and thus the chemical species that were generated in the cell. During the deposition, current, I, and charge, Q, passed through the cell were logged as a function of deposition time. These quantities could be consulted while synthesis was ongoing as a diagnostic tool to ensure that the deposition process was proceeding correctly. Fig. 2.2(a) illustrates how these values typically evolve over time: peak current is observed upon commencement of deposition while the substrate is clean, but is shown to decrease rapidly as material deposits on the surface and the substrate's effective resistance is increased. A plateau is reached when the exposed surface of the substrate is covered, after which material continues to deposit normally. The thickness of produced films was primarily controlled through the deposition time used; alternatively, a cut-off on Q could be imposed to limit film thickness when the area of substrate exposed to solution was accounted for. While galvanostatic (i.e. fixed I) procedures are known to result in films of great uniformity, the presence of multiple oxidation states with close-lying reduction potentials rendered this method — which can allow large fluctuations in applied potential — impractical for the synthesis of the selected PBA films: materials deposited in such a way were typically very dark and opaque on account of over-reduction in the cell, and thus unsuitable for optical experiments.

PBA thin films reported herein were consistently deposited onto fluorine-doped tin oxide (FTO) coated soda–lime glass substrates (Ossila S302) with a sheet resistance of 11–13 Ω sq^{-1} and of $\sim$1 mm total thickness. The total volume of solution used in electrodeposition was consistently held at 10 ml, with relative concentrations of TM-based reagents selected to reflect the expected stoichiometry of the films as reported in literature [50, 53]. For both Cr–Cr and Fe–Cr PBAs, this ratio was 3:2 A^{III}:$[Cr(CN)_6]^{3-}$, where A was Cr or Fe, respectively. Reagents used in the synthesis were all acquired

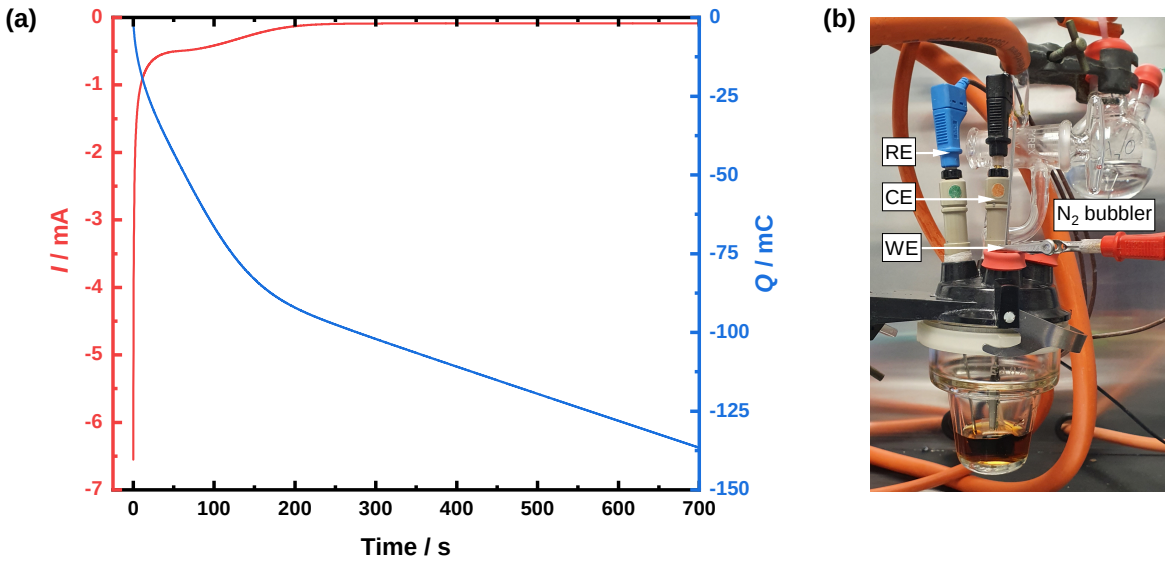

Fig. 2.2 (a) Current and charge passed through the electrochemical cell as a function of film deposition time, as acquired during synthesis of an Fe–Cr PBA film at an applied potential of $E = -0.8$ V. (b) Image of the electrochemical cell assembly, with key elements labelled.

from Sigma-Aldrich or Fisher Scientific and used without further purification. The potential applied to the working electrode was different for deposition of the two materials: $E = -1.2\,\mathrm{V}$ for Cr–Cr and $E = -0.8\,\mathrm{V}$ for Fe–Cr PBAs. Equipment used for electrodeposition included a Metrohm µAUTOLAB III potentiostat, a home-built Faraday cage constructed to house the electrochemical cell itself, and an N_2 bubbler used either to deaerate the solution between film depositions or blow N_2 over the surface of the solution and provide an inert atmosphere while deposition was ongoing. An image of the cell assembly is provided in Fig. 2.2(b).

2.1.2 Encapsulation of polycrystalline thin films

Thin films subject to optical experiments were encapsulated with an appropriate medium to reduce opacity arising from light scatter. This involved applying one drop of an adhesive to a 0.18 mm thick soda–lime glass coverslip which was then pressed against the film. Two adhesives were trialled for this purpose: cyanoacrylate glue and

Norland optical adhesive 61, the latter of which was cured when subject to 370 nm light (Intelligent LED Solutions N3535 1 PowerStar UV 365nm) for 5–10 minutes [47]. The merits of this procedure will be discussed in Chapter 3.

2.2 Compositional and structural characterisation techniques

A series of spectroscopic and morphological measurements are suitable for the characterisation of PBA films. While the background theory behind the techniques will not be described in detail, the specific relevance of each to these materials and the kind of information that is gleaned will be discussed in turn.

2.2.1 Electronic spectroscopy

As previously mentioned in Chapter 1, the intense colours of different PBAs arise from MM′CT transitions, which are often referred to as intervalence charge transfer in literature. These provide a unique spectral fingerprint for the characterisation of thin films by ultraviolet (UV)-visible spectroscopy. Identification of a PBA film can thus be made through determining the peak position for the characteristic transitions that dominate the spectrum.

The electronic spectrum for Fe–Cr PBA is dominated by a broad MM′CT band centred at 450 nm, with no other discernible features within the visible region [52, 54, 55]. In contrast, the electronic spectrum for Cr–Cr PBA is much more complex and is characterised by a strong absorption edge in at <350 nm, a peak at 380 nm, a weaker shoulder at 515 nm, and a succession of weak, poorly resolved peaks between 550 and 750 nm [49, 54]. An additional absorption feature may be observed in the NIR with a maximum beyond 1000 nm in reduced Cr–Cr PBA [19, 49]. There is a lack of

consensus in the literature as to the assignment of any of these peaks, which will be explored further in Chapter 5. Nevertheless, the aforementioned spectral features in both Fe–Cr and Cr–Cr PBA were replicated upon synthesis of films presented in this work and are illustrated in Fig. 2.3.

Given the sensitivity of spectra to the oxidation states and ligand-field splitting of the TM species present, any observed peak shifting or presence of shoulders provide a good indication of unwanted chemical processes occurring. This is evident in the Fe–Cr PBA, which undergoes linkage isomerisation to yield $Fe^{II}-NC-Cr^{III} \longrightarrow Fe^{II}-CN-Cr^{III}$. This is associated with a gradual colour change from brick red to green [56–59]. In the same vein, oxidation of Cr–Cr PBA can also be discerned from the electronic spectrum as it results in suppression of absorption in the NIR.

In addition to providing information about PBA material composition, electronic spectra enable qualitative judgements to be made about film thickness through application of the Beer-Lambert law. This describes the attenuation of light transmitted through a medium by absorption and is given by:

$$A = -\log\left(\frac{I}{I_0}\right) = 0.434\alpha\ell \tag{2.1}$$

where A is absorbance (also referred to as optical density, OD), I and I_0 are the transmitted and incident light intensities, respectively. α is the absorption (or attenuation) coefficient that is related to the probability of absorption, while the prefactor 0.434 accounts for conversion from base e (upon which α is defined) to base 10 (upon which A is described). ℓ is the path length of light taken through the medium. As α is a material property which should be consistent across different films with the same composition, the path length can be used to estimate film thickness, d, in lieu of full morphological characterisation. Complications arise in the event of excessive scattering observed for thicker films, limiting the usefulness of UV-visible spectroscopy to gauging

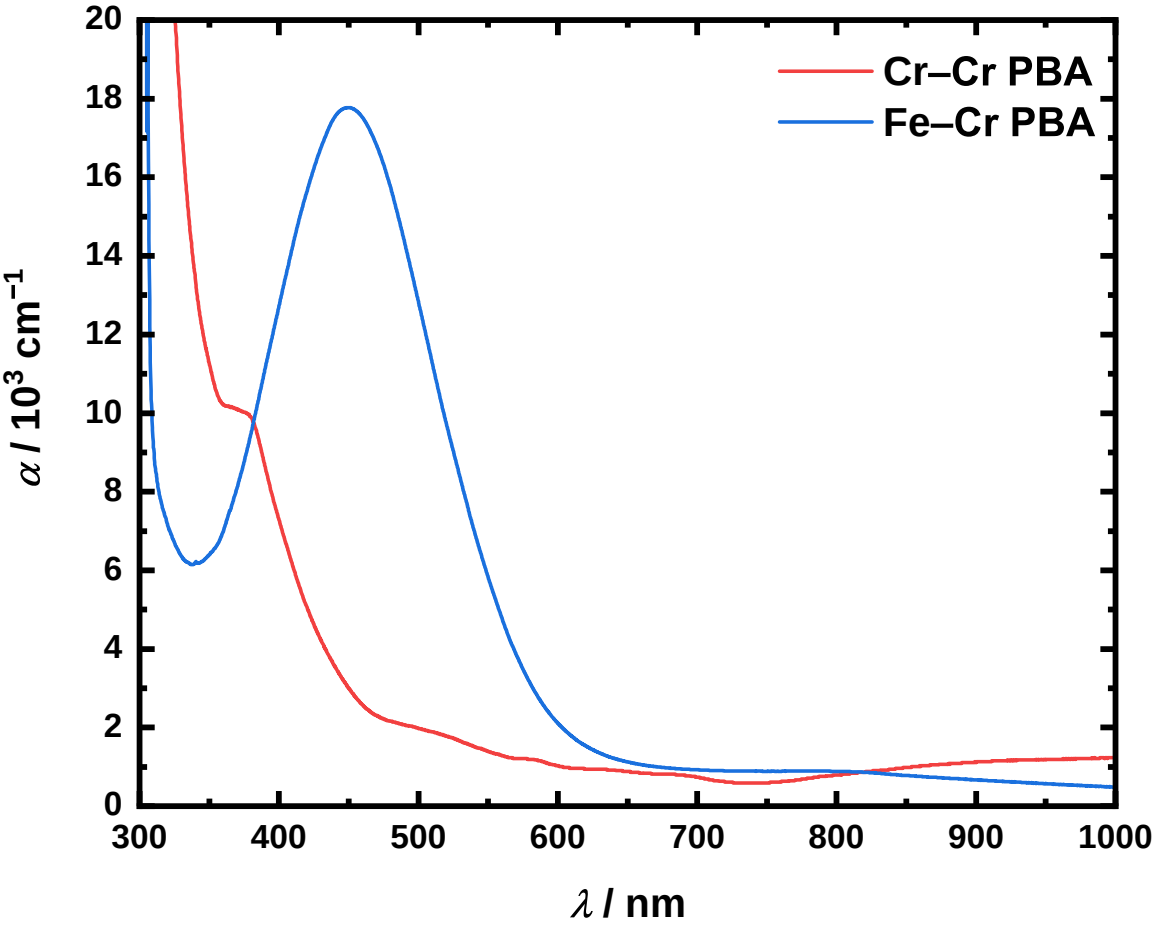

Fig. 2.3 Electronic spectra for encapsulated Cr–Cr (red) and Fe–Cr (blue) PBA thin films. The absorption coefficient, α, has been calculated by accounting for the thickness, d, of the material ($d_{\mathrm{Cr–Cr}} = 1110(50)$ nm and $d_{\mathrm{Fe–Cr}} = 1300(100)$ nm). For the purposes of this calculation, attenuation of transmitted light through reflection and scattering is ignored. Measurements were recorded against a reference comprising a clean substrate encapsulated with adhesive and a glass coverslip.

thickness only of films possessing sufficient optical quality, such as those encapsulated with a suitable adhesive.

The electronic spectra reported herein were obtained using one of two means. For general film characterisation, these were obtained using a commercial double-beam spectrophotometer (Shimadzu UV-1800). For data complementary to transient absorption measurements, spectra were recorded using the supercontinuum probe generated by our laser system, as described in Section 2.5.

2.2.2 Vibrational spectroscopy

The nature of the metal–ligand interactions observed in PBAs also renders vibrational spectroscopy a powerful tool in characterisation of thin films. Coordination of the CN^- ligands to the metal occurs through σ-donation and π-backbonding interactions, both of which adjust the stability of the C≡N bond and modulate the frequency of its stretching vibration. The contribution from each of these effects is sensitive to the identity of the TM cation, its oxidation state and its coordination mode (i.e. whether coordinated to C or N), all of which affect the metal cation's ability to accept and donate electron density.

Vibrational spectra have been extensively reported for both Cr–Cr and Fe–Cr PBAs. Infrared (IR) spectra for Cr–Cr PBA possess a primary band at ∼2190 cm^{-1} corresponding to the C≡N stretch mode in a Cr^{III}–CN coordination environment. A second band may also appear at ∼2070 cm^{-1}, which corresponds to the same mode in a Cr^{II}–CN coordination environment [19, 48, 49, 51, 60]. It has been reported that the IR bands are invariant to the oxidation state of N–coordinated A-sites in Cr–Cr PBA [60], which is a major limitation in using this technique for total stoichiometric evaluation. For Fe–Cr PBA, two peaks are observed in the IR spectrum: a primary band at ∼2160 cm^{-1} corresponding to the C≡N stretch mode in the Cr^{III}–CN coordination

environment and a second band at ∼2100 cm^{-1} corresponding to the same mode in the linkage isomer Fe^{II}–CN coordination environment [53, 55, 59]. While the changes in the electronic spectrum associated with linkage isomerism in Fe–Cr PBA occur over the course of days or months, growth of the associated band in the vibrational spectrum is apparent within the space of hours [59, 61].

It is obvious that conventional IR measurements are an effective probe for coarse determination of material composition. However, the caveat is that the greatest sensitivity is only afforded when characterising powders or crystals. To record spectra of reasonable quality on a thin film requires either scraping it from the substrate or the use of reflection geometry, which then imposes its own constraints on the substrate used and is hindered when the material is encapsulated. Raman spectroscopy offers a viable alternative as it can be used at any stage of the film's life, encapsulated or not, on account of the ability to change the focal depth of the source.

While Raman spectra have previously been reported for Fe–Cr PBA [55], none for Cr–Cr PBA have appeared in literature. A Raman study on PBAs in general has indicated that IR- or Raman-exclusive bands may occur depending on the symmetry and stoichiometry of the material [62]. This is because the Raman effect arises from inelastic scattering of light, so the resultant vibrational spectra are subject to a different set of selection rules to those obtained through IR absorption: whereas normal modes may only be IR-active if they incur a change in dipole moment, Raman-active modes must have an associated change in polarisability. Raman and IR spectra will possess features that may or may not be mutually exclusive, depending on the system under study. Furthermore, it is possible that features common to both may appear at distinct frequencies, although the differences in PBAs are generally quite small [62].

Raman spectra recorded for Cr–Cr and Fe–Cr PBA films are provided in Fig. 2.4 and are representative of those measured for various films reported throughout this

work. The Raman spectrum for Cr–Cr PBA is accompanied by an IR reflectance spectrum recorded on the same film to enable comparison of the bands observed in each. The IR spectrum possesses the two peaks corresponding to both $Cr^{III}-CN$ and $Cr^{II}-CN$ coordination environments at similar frequencies to those reported in literature [19, 48, 49, 51, 60], which confirms that the B-sites in the material are indeed mixed-valence. Conversely, the Raman spectrum only possesses one peak which coincides with $Cr^{III}-CN$ moieties, indicating that the second band is not Raman-active. Thus, it can be concluded that that Raman spectra alone are insufficient to adequately characterise the oxidation state of B-sites in Cr–Cr PBA.

The Raman spectrum measured for Fe–Cr PBA possesses a peak at 2165 cm^{-1} corresponding to the $Cr^{III}-CN$ environment, in agreement with literature reporting both Raman [55] and IR data [53, 55, 59]. The second peak at 2108 cm^{-1} is attributed to an additional C≡N stretch band corresponding to the $Cr^{II}-CN-Fe^{III}$ coordination environment and results from the wavelength of the Raman light source — an intense laser — being resonant with the MM′CT band in Fe–Cr PBA [55]. Its similarity to the frequency observed for the linkage isomer $Fe^{II}-CN$ amply demonstrates that due care should be taken in assignment of Raman bands since peaks resulting from vibronic transitions may also be observed.

Raman spectra reported throughout this thesis were obtained using a Raman microscope (Renishaw inVia) employing a 514 nm laser line. In the event of resonant excitation of the sample, the laser was attenuated to reduce the risk of photodegradation. The Raman microscope also enabled measurement of IR reflectance spectra using a modular attachment (Smiths IlluminatIR).

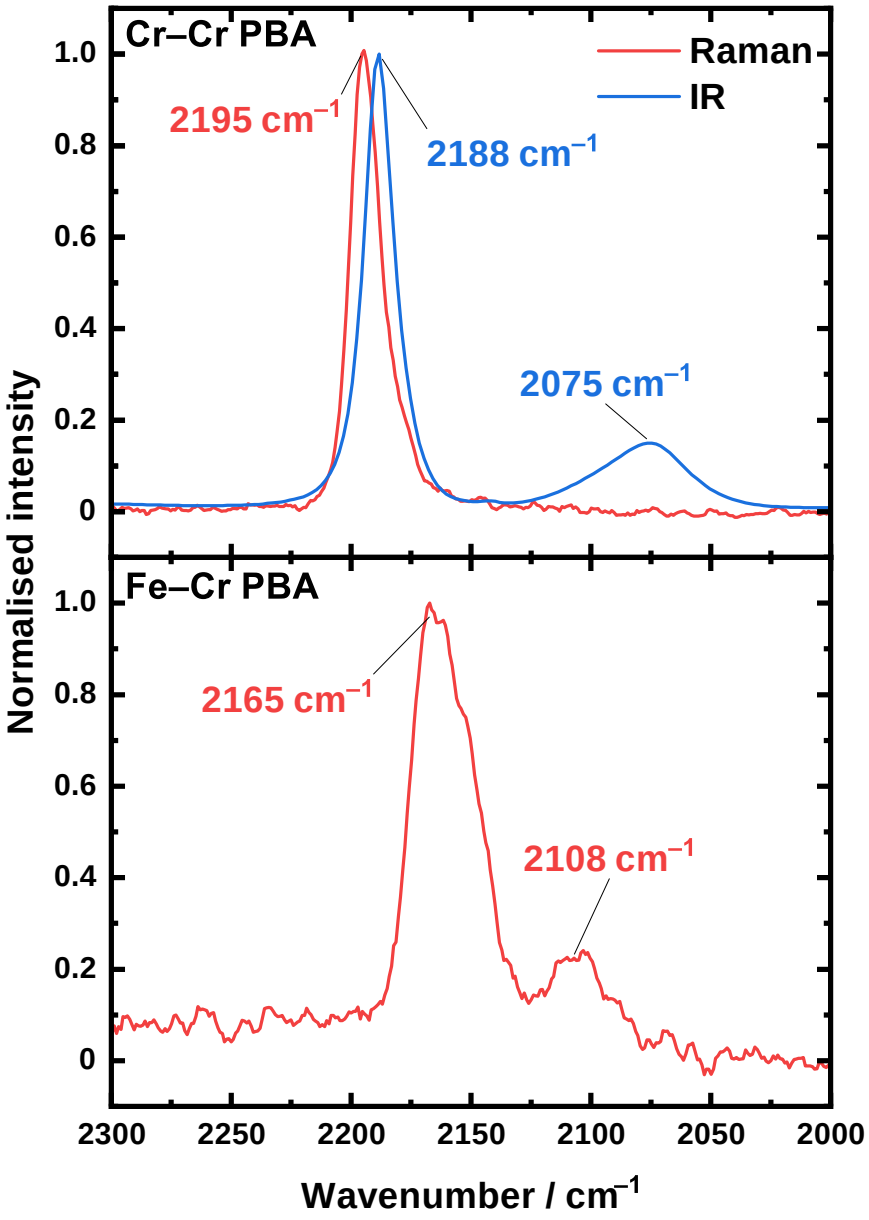

Fig. 2.4 Vibrational spectra recorded for Cr–Cr (top panel) and Fe–Cr (bottom panel) PBA thin films. Raman spectra have been recorded using a 514 nm laser line; IR measured in reflectance mode. The frequencies of any clearly discernible peaks have been highlighted.

2.2.3 Atomic force microscopy

Atomic force microscopy (AFM) relies upon the use of interatomic repulsion forces between a sample and a sharp tip to measure surface topology. Different methods for obtaining images exist with varying suitability for different materials. The most common method employed is “tapping mode”, whereby the cantilever holding the tip oscillates at a defined frequency which is dampened as it meets the sample surface. To mitigate this, tip height is adjusted to alleviate the force exerted, thereby reverting to the set oscillation frequency. Changes in the oscillation frequency are measured through reflection of a laser from the back of the cantilever onto a photodetector which can measure the deflection. Images are obtained through raster motion across the sample, creating a topological map of the surface.

In the context of the reported studies, AFM was primarily used to determine film thickness. The procedure involved creating a sharp step between the film and the substrate by drawing a razor blade across its surface, although this would be unnecessary for films which already possessed a well-defined boundary. The AFM probe would then be engaged within the vicinity of this step and a wide image encompassing both a large area of the film and the substrate recorded. A series of parallel sections (typically six) would be drawn across the image and their corresponding height profiles exported. During post-processing, any tilt in the height profiles was removed through subtraction of a straight line along the region corresponding to the substrate. The individual sections were displaced horizontally so that all the steps would coincide and the mean height profile calculated. This is demonstrated in Fig. 2.5. To ensure that it would not be skewed by a gradual step, the film thickness would be determined by computing the mean height from 10 µm across the surface onwards. For the example image shown, thickness was determined to be $d = 1300(100)\,\mathrm{nm}$.

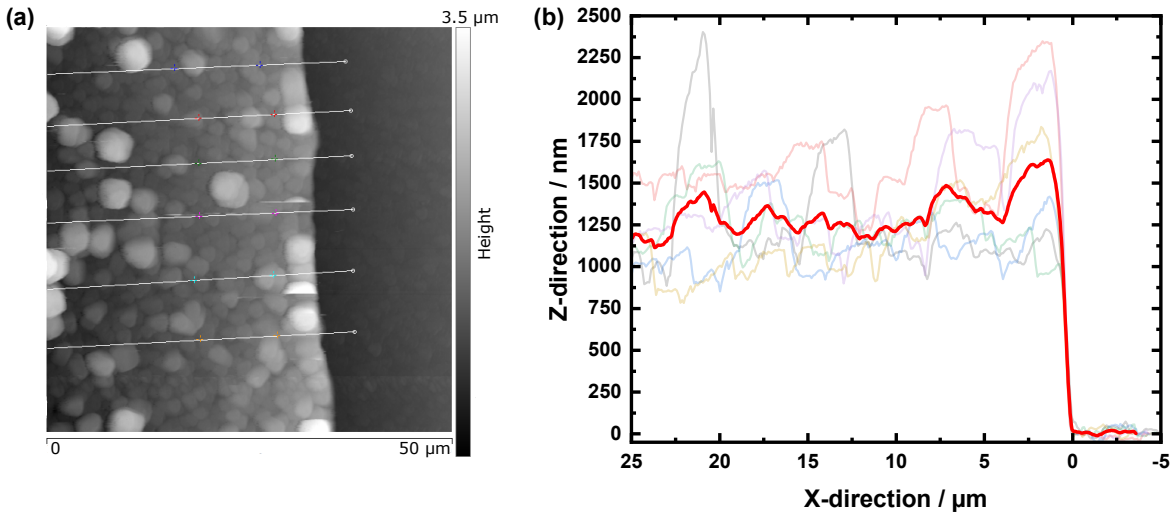

Fig. 2.5 Film thickness determination using AFM. (a) AFM image of an Fe–Cr film along the film's edge. The six parallel lines illustrate cross-sections for which height data is exported for analysis. (b) Height profile for the six cross sections, post-processing (coloured, transparent). The mean height profile is calculated from these (red, bold).

Measurements were performed on a commercial scanning probe microscope (Veeco Nanoman VS with NanoScope 7.30). Images were analysed using NanoScope Analysis 1.5 software and height profiles exported to a routine data analysis package.

2.3 Magneto-optics

Magnetic characterisation of PBA thin films was predominantly performed through transmission-based MO techniques. These exploit the Faraday effect [6], a phenomenon whereby the polarisation state of light that propagates through a medium in the presence of a magnetic field is altered. The principles behind this and practical means of measurement will be discussed in turn.

2.3.1 Optical activity

A comprehensive description of the phase and amplitude behaviour of electromagnetic radiation propagating through a medium is given by the complex refractive index, $\tilde{n}$. This is defined by the following:

$$\tilde{n} = n + i\kappa \tag{2.2}$$

where the real component, n, is the refractive index which relates to the phase velocity of light through the material, and the imaginary component, κ, is the extinction coefficient which describes the attenuation of light in the medium through absorption. Note that this latter quantity is directly related to the absorption coefficient, α, described in Eq. 2.1 through the relation $\kappa = \frac{\alpha\lambda}{4\pi}$.

Polarised light can be considered to be the superposition of two components whose electric fields rotate in opposite directions: left- and right-hand circular polarisations, which are defined in this work by the direction of rotation from the point of view of the receiver rather than the source. These are henceforth denoted by σ_+ and σ_-, respectively. In anisotropic media, there is a polarisation dependence to $\tilde{n}$, whereby the two circular components may undergo different degrees of refraction or absorption; these give rise to optical activity and circular dichroism. In an optically active medium, $n_{\sigma_+} \neq n_{\sigma_-}$, meaning that the two components will travel with different phase velocities and thus will have undergone a relative phase-shift upon transmission. The net effect of this is that polarisation of transmitted light will have been rotated by an amount proportional to the path length through the medium. Similarly for a material that exhibits circular dichroism, $\kappa_{\sigma_+} \neq \kappa_{\sigma_-}$, resulting in differential absorption of the two polarisation components. The difference in amplitude of the two components will lead to an elliptical polarisation overall. Both of these cases are illustrated in Fig. 2.6.

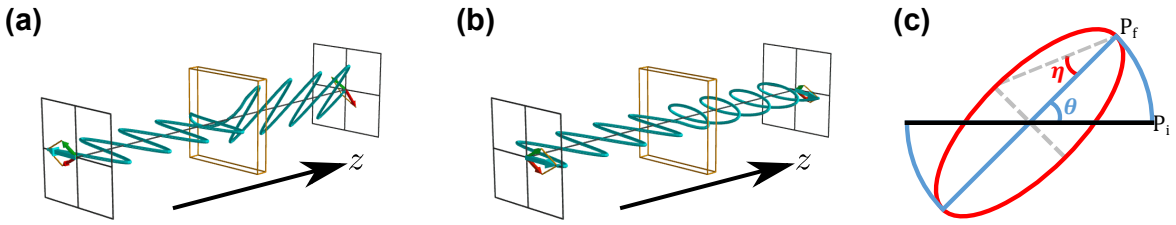

Fig. 2.6 Illustration of polarised light propagation along the z-direction through media exhibiting (a) optical activity and (b) circular dichroism, giving rise to rotation and ellipticity in the polarisation of transmitted light. These are quantified by the angles θ and η, respectively, as depicted in (c) where polarisation changes from initial state P_i to final state P_f. Images showing light propagation were generated using the EMANIM web application [63].

Intrinsic optical activity and circular dichroism is often limited to materials that are innately chiral in nature. However, these phenomena may also be induced in even achiral media when subject to a magnetic field.

2.3.2 The Faraday effect

An atomic state with total angular momentum quantum number J possesses $(2J+1)$ sub-states, each with magnetic quantum number M_J. While degenerate in a spherically symmetric environment, these will undergo an energy shift, ΔE, in response to a magnetic field. This is known as Zeeman splitting and is quantified by:

$$\Delta E = g_J \mu_\mathrm{B} B_z M_J \tag{2.3}$$

where g_J is the Landé g-factor, μ_B is the Bohr magneton, and B_z is the component of magnetic field along the light propagation axis (denoted by z).

For an electronic transition to occur, the total angular momentum of the system must be conserved. A photon possesses intrinsic angular momentum of $J_z = \pm\hbar$, with $+\hbar$ carried by σ_+ and $-\hbar$ carried by σ_-. Thus, there will be selective absorption of the polarisation component with J_z corresponding to the difference in M_J between the

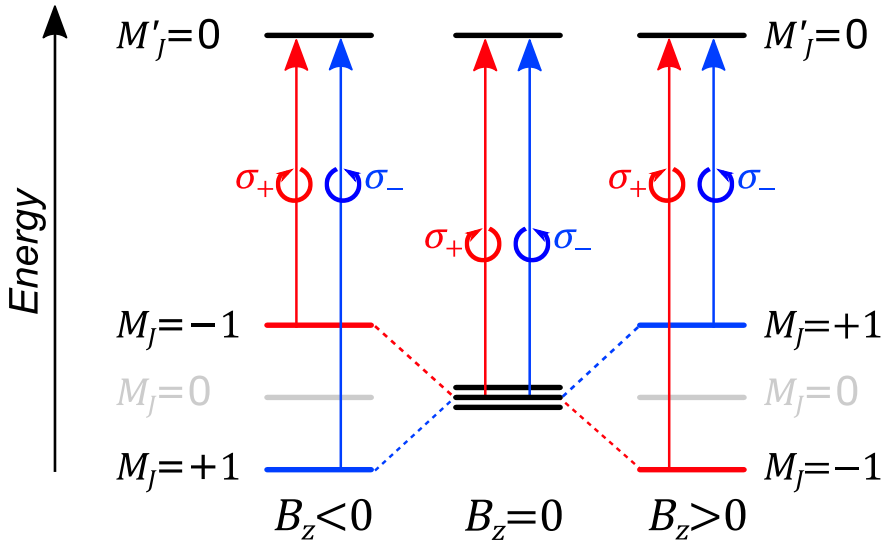

Fig. 2.7 Energy level diagram for a hypothetical system with total angular momentum quantum number $J = 1$. Magnetic sublevels, M_J, undergo energy separation in the presence of a magnetic field B_z due to the Zeeman effect, enabling differential absorption of left (σ_+) and right (σ_-) circular polarisation of light. Only the $M'_J = 0$ excited state is included for simplicity.

two states involved in the transition. This leads to Faraday ellipticity, also known as magnetic circular dichroism (MCD), and is illustrated in Fig. 2.7.

As $\tilde{n}$ is a complex quantity, its real and imaginary components can be related to one another through the Kramers–Kronig relations. It then follows that any change in the wavelength-dependence of κ induced by magnetic field will be accompanied by a change in n. This gives rise to differential refraction of σ_+ and σ_-, leading to Faraday rotation, also known as magnetic circular birefringence.

Faraday rotation

The degree to which Faraday rotation is observed in a material can be quantified by the following empirical equation:

$$\theta_{\mathrm{F}} = V B_z \ell \tag{2.4}$$

where θ_{F} represents the angle of rotation and ℓ is again the path length. V is the Verdet constant, a material property that is dependent on both the wavelength of the propagating light and the temperature.

The $\boldsymbol{B}$-field can be related to magnetisation, $\boldsymbol{M}$, as follows:

$$\begin{aligned} \boldsymbol{B} &= \mu_0 \mu_{\mathrm{r}} \boldsymbol{H} \\ &= \mu_0 (1 + \chi) \boldsymbol{H} \\ &= \mu_0 (\boldsymbol{H} + \boldsymbol{M}) \end{aligned} \tag{2.5}$$

where μ_0 is the vacuum permeability constant, μ_{r} is the relative permeability of the medium, $\boldsymbol{H}$ is the external magnetic field and χ is magnetic susceptibility. It can be surmised that $\theta_{\mathrm{F}} \propto \mu_{\mathrm{r}}$ and is indirectly related to $\boldsymbol{M}$; thus, its magnitude is a reasonable quantity to use for comparison across different films to make relative statements regarding their magnetic properties.

There are two practical means of measuring Faraday rotation: differential transmission through a polarisation analyser or direct polarimetric characterisation of the transmitted beam.

Differential transmission involves passing horizontally-polarised light through the material followed by a polariser with its transmissive axis set to 45° relative to the initial polarisation. The intensity of light transmitted through the polariser is recorded while applying equivalent magnetic fields in opposite directions ($\pm H$). As the field is aligned in one direction, the polarisation of light will be rotated by the medium towards the polariser axis, while the converse is true for the opposite field. The magnetic-only aspect can thus be determined by $\theta_{\mathrm{F}} = I_{+H} - I_{-H}$. When used with a broadband light source and detection scheme, this technique can be used to record the wavelength-dependence of Faraday rotation [64, 65]. This is often referred to as magnetic optical rotary dispersion (MORD).

Alternatively, the polarisation state of monochromatic light can be directly characterised after transmission through a sample using a half-wave plate, polarising beamsplitter and two well-matched photodetectors. In this scheme, a beam passing through the beamsplitter will be split into two, each corresponding to the horizontal and vertical components of the input polarisation and directed towards its own detector. The half-wave plate can be used to rotate input polarisation to 45° to yield two beams of equal intensity. Through monitoring the difference between the signals generated at each photodiode, the effect of varying magnetic field on the polarisation can be measured.

Both techniques have their advantages and limitations and are best used in combination to acquire complementary data. Differential transmission is most appropriate for acquiring the whole Faraday rotation spectrum given its ability to measure multiple wavelengths simultaneously. From this, an appropriate probe wavelength can be selected for use with the polarimetric experiment, which is more appropriate for determining magnetic hysteresis or time-resolved information given its greater sensitivity and faster data acquisition speed.

Magnetic circular dichroism

While Faraday rotation may in principle be observed at any wavelength, MCD may only occur at those frequencies which are close to resonant with a spectroscopic transition. Fig. 2.7 illustrated how MCD may arise when Zeeman splitting of a magnetically degenerate ground state occurs. Likewise, splitting of degenerate excited states or reducing energy separation of distinct electronic states to the point where they may undergo mixing also give rise to MCD, with each contributing distinct features to the spectra.

MCD can be measured using similar methods to Faraday rotation — differential absorption or polarimetric characterisation — albeit with some distinct changes.

Differential absorption involves passing σ_+ and σ_- through the material separately and measuring the difference in attenuation of each. This is readily achieved using a photoelastic modulator to convert linearly polarised light into σ_+ and σ_-, alternating between the two at a rapid rate (typically ∼25–30 kHz). Alternatively, recording the transmitted intensity of fixed circular polarisation of either kind while applying $\pm H$ as described before for rotation should yield the same result [64, 65]. This is because reversing the field will invert the Zeeman splitting of degenerate states, as was shown in Fig. 2.7, and thus will still result in differential absorption.

The same polarimetric scheme can be used as for rotation, but with addition of a quarter-wave plate. The photodetectors should initially be balanced (input polarisation set to 45°) using the half-wave plate. The quarter-wave plate should then be inserted in front of the half-wave plate and set close to its fast axis to balance again, which should undo any ellipticity in the beam. As magnetic field is varied, any change in ellipticity is thus converted into a change in rotation, which can be measured *via* the difference signal.

2.4 Optical pump–probe techniques

Elucidation of the photoinduced electronic and magnetisation dynamics in PBAs necessitates the use of optical pump–probe methods, which are among the only ways to probe a system on the relevant ultrafast timescales. These involve use of an intense laser pulse to photoexcite a system in a process referred to as optical "pumping". The point at which this occurs is used to clock the process under investigation, thus taken to be time zero, t_0. After a finite time delay, t_{delay}, a second "probe" pulse can yield information on the current state of the system. In a typical ultrafast pump–probe

experiment, both pump and probe are generated using the same femtosecond laser system, and an optical delay line is used to stagger one beam with respect to the other so that t_{delay} can be varied.

The electronic and magnetic components of the dynamics are each investigated by two different pump–probe techniques to yield complementary information. The principles that underpin each of these will be briefly discussed.

2.4.1 Transient absorption spectroscopy

TA spectroscopy is used to investigate changes in electronic state. This experiment employs UV or visible laser pulses, measuring the intensity of the probe with respect to t_{delay} to yield kinetic information on population of excited states following optical pumping. While the probe may be monochromatic, it is common to employ a broadband beam for these experiments which allows for evolution of the entire spectrum to be measured. From this, contributions arising from the ground and any populated excited states may simultaneously be observed. This is typically presented in the form of difference spectra, which depict the change in absorption of photoexcited sample relative to the ground state, ΔA, with respect to t_{delay} and wavelength in terms of OD. This is illustrated for a hypothetical system in Fig. 2.8, where the relevant electronic states and their contribution to the TA signal are depicted.

While TA spectra may be rich and complex, they normally result from summation of a few distinct features. The sign and magnitude of these signals typically correspond to a small set of processes, outlined as follows.

$\Delta A < 0$ is characteristic of a ground state bleach (GSB) signal. This occurs when excitation of chromophores is intense enough to appreciably depopulate the ground state, thereby reducing the absorbance. The ground state bleach is representative of the static absorption spectrum that is obtained through UV-visible spectroscopy.

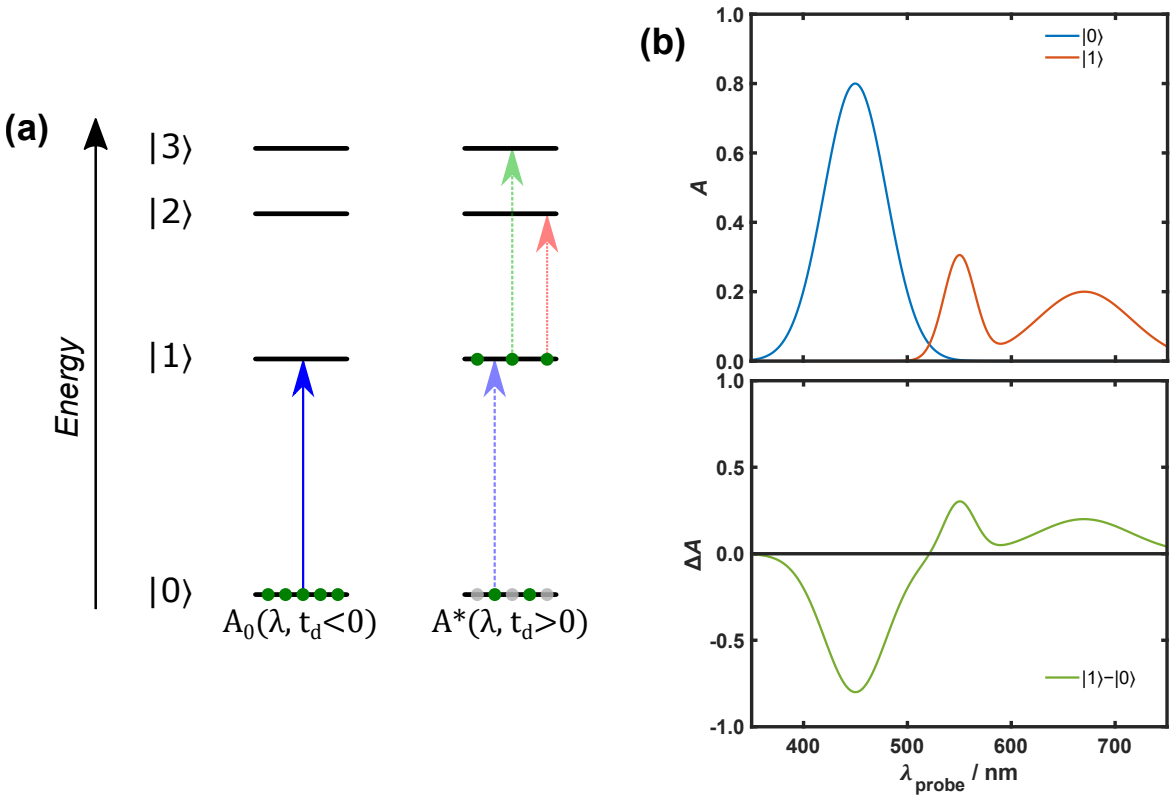

Fig. 2.8 Energy diagram for electronic states of a hypothetical system (a) along with corresponding simulated spectra (b, top). Population of the states is represented by green dots. When the ground state, $|0\rangle$, is fully populated ($t_{\mathrm{delay}} < 0$), intense absorption is observed in a wide band centred at 450 nm. After photoexcitation ($t_{\mathrm{delay}} > 0$) to the first excited state, $|1\rangle$, absorption bands may be observed corresponding to transitions to even higher lying states at 550 and 670 nm. Conversely, the ground state absorption in the blue will now be less intense as the $|0\rangle$ population has been reduced. TA measures the difference between these (b, bottom).

Alternatively, $\Delta A < 0$ can be indicative of stimulated emission from an already excited state by specific frequency components of the probe, or photoluminescence observed upon radiative decay of an excited state to either a lower-lying excited state or the ground state. In accordance with Kasha's rule, these features would be expected to appear at wavelengths redder than that used to pump. Thus far, neither stimulated emission nor photoluminescence have been observed for PBAs in bulk form.

$\Delta A > 0$ is described as the excited state absorption (ESA) signal, which results from transitions to even higher excited states upon population of the initial excited states following optical pumping.

Strong, peculiar artefacts that are inherent to the experiment also frequently appear around t_0 when the pump and probe overlap both spatially and temporally. These stem from cross-phase modulation (XPM): a non-linear optical phenomenon whereby the intense electric field of the pump pulse induces a change in the real part of the refractive index of the sample, resulting in a shift of the probe's component frequencies and consequently its spectral distribution [66]. This manifests as an artefact with a characteristic intensity profile in TA kinetic traces with a shape and amplitude that are strongly dependent on both the frequency and temporal dispersion of the probe within any given experiment [66]; in the work presented throughout this thesis, XPM features are typically narrow and sharp for bluer wavelengths, but become broader and less intense at redder wavelengths. As these artefacts are superimposed onto the TA signal observed from the sample, they often hinder the observation of very early dynamics.

It should be noted that while reporting transient spectra in terms of ΔA is acceptable for non-lossy media such as homogeneous solutions, light transmitted through solids is subject to non-negligible attenuation as a result of reflection and scatter, both of which may also be influenced by optical pumping in addition to absorption. A more robust treatment of photoinduced dynamics in thin films would at least take reflection into

account using complementary time-resolved transmittance and reflectance spectra [67, 68] to more accurately determine dynamics that arise from change in absorption only. However, the use of reflection geometry is beyond the current capabilities of the ultrafast pump–probe setup in our lab. Hence, transient spectra for the PBA films reported in this work are represented in terms of relative transmittance change and are referred to as TT spectra. These are calculated from the "TA" outputted by the experiment through $\Delta T/T = -100 \times \ln(10) \times \Delta A$ and expressed as a percentage. Nevertheless, contributions from change in absorption coefficient are assumed to dominate the TT spectra for the sake of simplicity, and thus spectral features for which transmittance is increased ($\Delta T/T > 0$) or decreased ($\Delta T/T < 0$) are still attributed to GSB and ESA, respectively.

2.4.2 Time-resolved magneto-optics

TR-MO experiments are used to investigate magnetisation dynamics in a system through combining the pump–probe experiment with the MO methods described in Section 2.3.2. Both the broadband and polarimetric techniques for Faraday rotation/ellipticity are equally valid for use in time-resolved measurements [65], with the only practical difference being measurement of changes in the probe polarisation at the pump-modulated frequency.

2.5 Optical setup

The optical experiments reported herein employed a fully integrated Yb-based laser system in conjunction with an optical parametric amplifier (OPA), prism compressor and harmonics generator to produce ultrashort laser pulses to serve as pump and/or probe. Excluding the aforementioned systems, the experimental configuration was assembled from scratch by the Johansson research group as a collaborative effort following the replacement of an older Ti:sapphire laser system in June 2021 and thus was in its second iteration at the time of writing. My own contributions to its construction included devising beam paths, sourcing suitable optics, and the design/implementation of the sample mount and beam/sample imaging stations. Day-to-day beam alignment and optimisation was also carried out by myself during the course of all presented experiments.

Since its assembly, the workings of the lab's experimental setup have been described by the group in literature [69]. A detailed schematic of the optical bench as used is provided in Fig. 2.9: each aspect of the experiment illustrated here will be discussed in turn.

2.5.1 Yb:KGW femtosecond laser

The femtosecond laser used in this work was a PHAROS from Light Conversion: a turnkey system comprising a laser oscillator and regenerative amplifier, both based on diode-pumped Yb-doped tungstate (Yb:KGW) media. The system was controlled *via* a web app on an external computer and all internal components were fully automated, negating the need for alignment or manual tuning.

The fundamental output of the laser were pulses of ∼270 fs duration and central wavelength 1028 nm. The maximum pulse energy of the output was 0.4 mJ, which could be maintained for repetition rates up to 25 kHz. Due to limitations of the

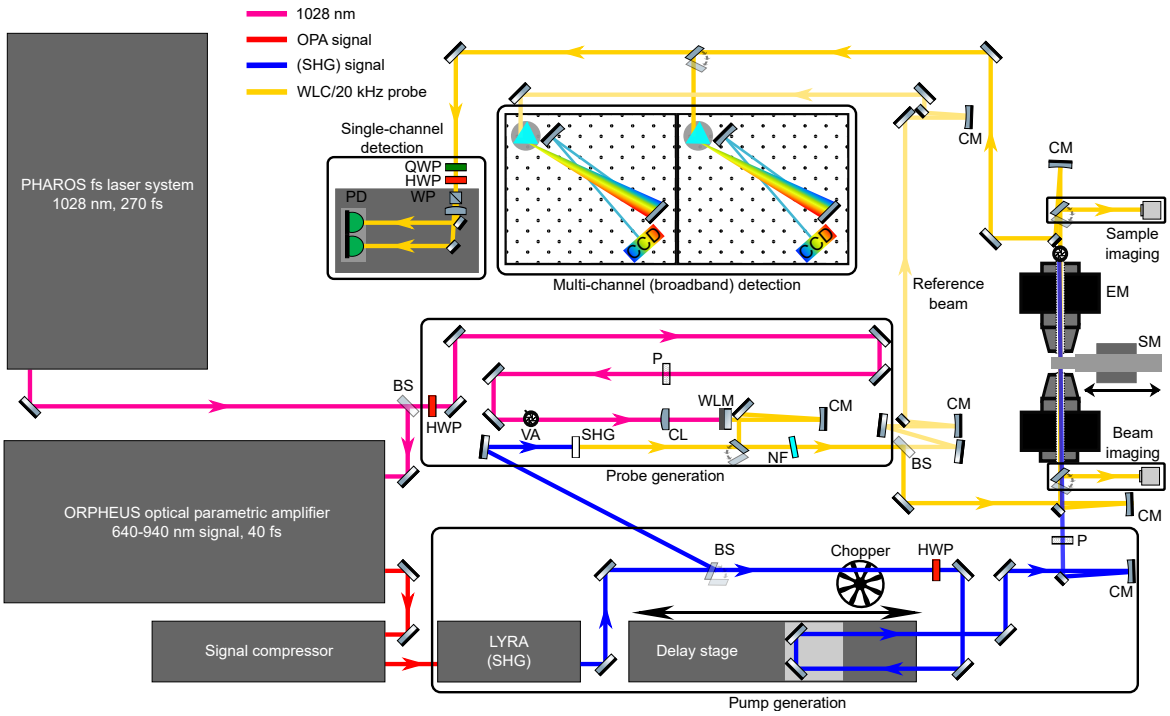

Fig. 2.9 Layout of the optical setup used for TA and MO experiments. Generation of pump/supercontinuum probe and the two detection schemes are labelled. Various terms are abbreviated as follows: beam splitter (BS), half-wave plate (HWP), quarter-wave plate (QWP), Wollaston Prism (WP), polariser (P), variable aperture (VA), convex lens (CL), medium for white light generation (WLM), concave mirror (CM), NIR filter (NF), electromagnet (EM), sample mount (SM), second-harmonic generation (SHG).

detectors and mechanical beam modulation employed in the experiment, the laser was typically operated at 1 kHz when using the multi-channel (broadband) detection scheme or 20 kHz when using the single-channel scheme. The system also possessed an internal pulse picker mechanism that could reduce the laser pulse delivery rate without changing the repetition rate of the regenerative amplifier. This was typically used in the measurement of pump-off signal when calibrating TR-MO experiments using single-channel detection.

2.5.2 Optical parametric amplifier

The OPA used was an ORPHEUS-F, also from Light Conversion. Like the PHAROS, the OPA was controlled *via* a dedicated app (WinTOPAS4) on an external computer and possessed several motorised components that could be tuned at ease by the user to improve efficiency.

The OPA was supplied with 90% of the 1028 nm output from the PHAROS (0.36 mJ) to serve as a pump. Inside, this was split using a polarising beamsplitter, with a preceding half-wave plate used to control the proportions of the two beams. The minor arm (1%) was used to generate supercontinuum in a sapphire plate to act as a seed for amplification. The major arm (99%) underwent second-harmonic generation (SHG) to 514 nm in a crystal of β-barium borate (BBO) to serve as a pump for the two amplification stages.

Both the supercontinuum and a minor part of the 514 nm pump beam were spatially overlapped with non-collinear geometry in a second BBO crystal during the first amplification stage. Provided that the phase of the pump and seed beams were sufficiently matched as they propagated through the medium, amplification would occur through fission of pump photons to yield additional photons with the same frequency as the seed, thus generating the “signal” beam. To satisfy the condition that

energy must be conserved upon splitting pump photons, this process also generated a second beam of frequency equal to the difference between that of the pump and the signal; this is known as the "idler". Because the supercontinuum that provided the seed for amplification was chirped, different frequency components would arrive at the BBO at different times. Through use of a delay stage, the temporal overlap of the pump and the supercontinuum could be adjusted to select which wavelength band was amplified for signal/idler generation.

The remaining part of the pump beam was then spatially and temporally overlapped with the previously generated signal/idler in a third BBO crystal during the second amplification stage. The geometry of the beams here was collinear and offered greater conversion efficiency to maximise power output. A series of dichroic mirrors were used to separate the signal from the idler, which were both directed through separate output ports.

The amplification process was capable of generating signal pulses within the range 650–900 nm and idler pulses within the region of 1200–2500 nm. A prism compressor extension was used to reduce the temporal width of the signal beam. This consisted of a first prism, which dispersed the beam and caused different wavelengths to travel different path lengths, while a second prism reconstructed the beam. The end result was that all the frequency components of the pulse lay within a tighter temporal envelope. This would produce pulses ∼40 fs in duration, which was close to the theoretical transform limit given their typical spectral width.

2.5.3 Pump generation and delay line

The ultrashort laser pulses that served as the pump for the pump–probe experiments were taken from the signal output of the OPA/compressor. This beam first passed through a harmonics generator (Light Conversion LYRA) that was capable of high

efficiency SHG using BBO. Phase matching was afforded by rotating the crystal using a motorised stage, which was controlled using the same software as the OPA. This made generation of pumps with wavelength between 320–460 nm possible, although the BBO could be bypassed entirely if a redder pump wavelength was required. The beam exited the harmonics generator using a modular set of two mirrors attached to the output port. A set of silver mirrors were used for 1st-harmonic output, but could be exchanged for a set of dichroic mirrors for 2nd-harmonic output; these were used in lieu of transmissive colour filters as a means of removing the input beam following SHG.

After the harmonics generator, the pump was passed through an optical chopper which modulated the beam at half the repetition rate of the laser — 500 Hz for measurements using broadband probe detection or 10 kHz for single-wavelength. The phase of the chopper was set to block every second pump pulse for the purpose of calculating differential absorption or change in probe polarisation. Note that because the wedge spacing on the chopper wheel used for 10 kHz modulation was much narrower than the original beam diameter (1.36 mm-wide spacing *vs.* ∼3 mm-wide beam), it was necessary to focus the pump through the holes for these experiments. This was achieved using an $f = 10\,\mathrm{cm}$ lens situated before the chopper, and an identical, second lens after the chopper to recollimate.

The pump was then diverted along a variable delay line comprising a hollow retroreflector (Newport U-BBR2.5-1S) mounted on a 60 cm mechanical translation stage (Aerotech PRO115LM-600) capable of providing $t_{\mathrm{delay}} \leq 3\,\mathrm{ns}$. The beam was subsequently focussed through the sample using an $f = -50\,\mathrm{cm}$ concave mirror *via* an intermediate D-mirror. The latter was equipped with piezoelectric inertia actuators (Thorlabs PIAK10) that allowed for coarse adjustments of pump alignment using manual adjustment screws or fine adjustments through an external control console

(Thorlabs KIM101). The pump passed through the sample such that it was quasi-collinear with the probe (∼1°), after which it was dumped using a variable aperture centred on the probe. The incident spot typically possessed a $1/e^2$ beam diameter on the order of 100 µm, which would change depending on wavelength used and additional optics inserted.

Pump fluence was controlled using a half-wave plate/polariser combination to attenuate pulse energy and control pump polarisation angle with respect to the probe. In the event that a circularly polarised pump was used, the polariser would be removed and the half-wave plate replaced with a quarter-wave plate. Fluence in this case would instead be controlled using a variable neutral density (ND) filter situated before the chopper wheel. The typical pump pulse energies employed for experiments were on the order of 1 µJ.

2.5.4 Supercontinuum probe generation

All 1028 nm output from the PHAROS not used to pump the OPA was instead dedicated to supercontinuum generation, which then served as a probe. In brief, the beam was attenuated using a half-wave plate/polariser combination, with polarisation set to horizontal. 2.5 mJ was focussed into 5 mm thick CaF_2 plate using an $f = 10\,\text{cm}$ lens to produce a white light supercontinuum; to prevent photodegradation through prolonged exposure to the NIR beam, this plate was continuously translated in an eccentric circular motion using a DC motor. A variable aperture positioned before the lens was used to trim the input beam edges, which enhanced stable filament production in the CaF_2 medium and thus reduced spectral noise in the white light generated. The white light itself was collimated with an $f = -10\,\text{cm}$ concave mirror, after which a short-pass filter (Newport 10CLVR-1) was used to filter out any residual fundamental.

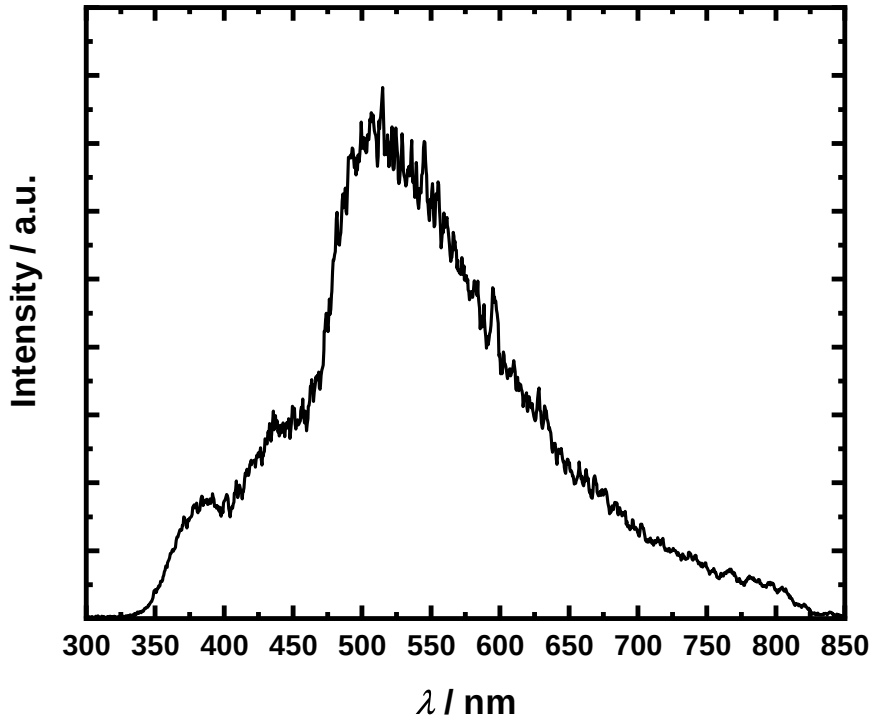

Fig. 2.10 Spectrum of the white light supercontinuum probe generated in CaF_2 after removal of any residual pump beam. Data were acquired using a portable, fibre-based spectrometer (OceanOptics HR2000+).

This ultimately resulted in a probe which spanned the detectable range of 350–750 nm: the spectrum for this is provided in Fig. 2.10.

The filtered beam was split into two using a metallic beam splitter: the transmitted arm (∼10% of overall intensity) was dedicated to referencing while the reflected arm (∼90%) was used as a probe and focussed through the sample using an $f = -50\,\mathrm{cm}$ concave mirror *via* an intermediate D-mirror. The probe beam diameter incident on the sample was on the order of ∼50 µm, while the total broadband probe intensity was too weak to be measurable (below the 20 nJ limit of detection). Following the sample, the probe was collimated using another $f = -50\,\mathrm{cm}$ concave mirror and directed towards either the multi-channel detection scheme for broadband measurements or single-channel scheme for measurements involving a monochromatic probe.

The reference beam was employed exclusively in measurements using the multi-channel detection scheme, accounting for shot-to-shot fluctuations in the white light supercontinuum and enhancing signal-to-noise. To make this process as effective as possible, the number of reflections and focussing/collimation steps for the reference beam was matched to the number used in the probe so that two beams would possess as similar spatial characteristics as possible.

2.5.5 Beam characterisation

It was necessary to regularly inspect pump and probe beam characteristics to ensure optimal experimental performance and reproducibility. A variety of methods were employed to measure the transverse spatial profile, spectral and temporal widths.

The OPA possessed an integrated spectrometer which could monitor the spectral shape of the signal output beam. This would automatically output the central wavelength, bandwidth and theoretical transform-limited pulse duration of the signal output *via* integrated software. Direct measurement of the pulse duration could be performed by diverting the signal beam away from the pump delay line and passing it into an autocorellator (APE Pulsecheck).

The procedure for measuring beam waists was as follows. Both pump and probe were intercepted immediately before the electromagnet and redirected to a camera (Basler acA1920-25um) positioned so that the sensor coincided with the focal point for the probe. Monochromatic bitmap images of the two beams were recorded and imported into an appropriate data analysis package. Each image was fitted with a 2D Gaussian function, as exemplified in Fig. 2.11. From the fitted Gaussian, the transverse $1/e^2$ diameters along the x- and y-directions would be averaged to give the overall beam waist.

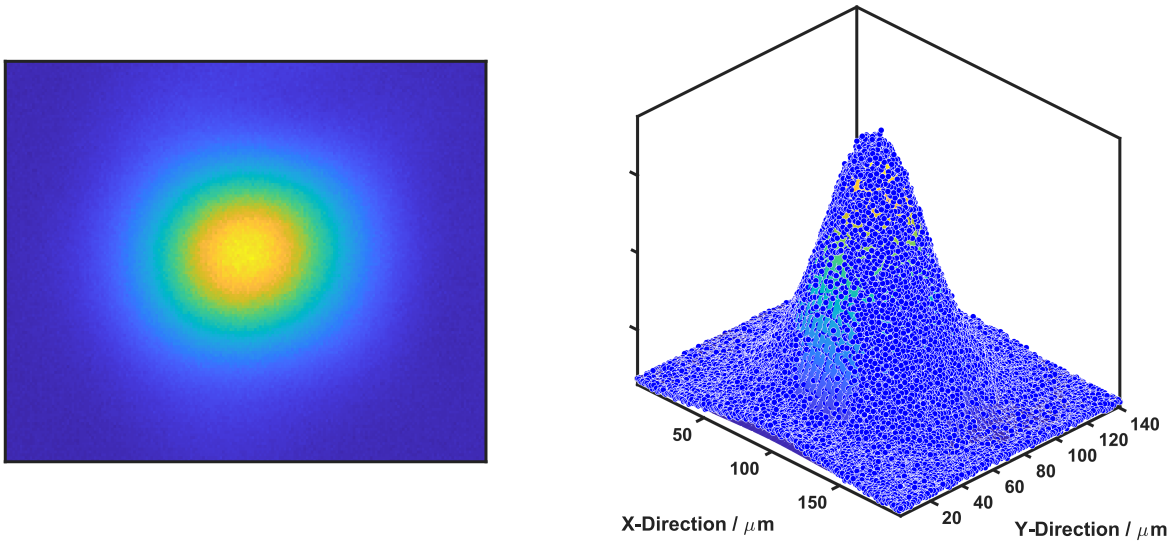

Fig. 2.11 Image of an 800 nm pump recorded with the beam imaging camera (left). A 2D Gaussian function is fitted to the intensity profile (right) for the purpose of calculating beam waist. In this example, the beam waist is 116 µm.

A thermopile sensor (Ophir 3A with Juno USB interface) controlled by software on an external computer was used to measure pump power for the purpose of determining the pump fluence, F_{pump}. This is calculated using the following equation:

$$F_{\text{pump}} = \frac{P_{\text{mean}}}{f_{\text{rep}} A_{\text{pump}}} \tag{2.6}$$

where P_{mean} is the time-averaged power, f_{rep} is the laser repetition rate, and A_{pump} is the area of the pump beam, which itself is calculated from the beam waist by assuming the shape is approximately circular.

2.5.6 Multi-channel (broadband) detection

Broadband TA/TR-MO measurements employed two identical home-made spectrometers employing a dispersive multi-channel detection scheme capable of monitoring a wide range of wavelengths simultaneously for both probe and reference beams. As

the maximum read-out rate was 1 kHz, these were not suitable for measurements employing high laser repetition rates.

The path taken by each beam through the spectrometers was as follows: the beam would be dispersed upon entry by a prism (Eksma Optics) mounted on a rotary stage set to Brewster's angle. Two concave mirrors were used to control divergence and redirect the beam towards a camera (Entwicklungsbuero Stresing) based on a 512×58 pixel charge-coupled device array (Hamamatsu S7030). To account for the greater intensity of the white light supercontinuum at the red-end of the spectrum and avoid camera saturation, a graduated ND filter was positioned in front of the camera such that the UV-end of the dispersed beam would be attenuated less than the red.

The cameras were interfaced with a LabVIEW program which handled all data acquisition. Through this, intensity data acquired across vertical pixel lines were binned while horizontal lines were tracked separately. Each of the 512 pixel lines would correspond to a different wavelength. This would be calibrated by the user by passing the white light through a filter (Schott BG36) selected for its distinctive features across the UV-visible-NIR spectrum. The wavelengths for around 20 peaks or troughs detected by the cameras would be matched to specific pixels and a 3rd-order polynomial function fitted to these for assignment of every pixel.

Because the spectrometers used a prism to disperse the white light, the frequency dependence of the dispersion was non-linear: blue was dispersed more than red, and as such, the UV-end of the spectrum would be incident upon more pixels than the NIR. Thus, measurements that employed the cameras possessed greater spectral resolution for bluer wavelengths than red.

2.5.7 Single-channel (monochromatic) detection

The single-channel detection scheme was typically employed for MO/TR-MO experiments where the greater sensitivity afforded by higher laser repetition rates was necessary, and closely followed the polarimetric scheme described in Section 2.3.2. Experiments using this detection method employed a 20 kHz probe originating from the OPA instead of a white light supercontinuum. This was generated as follows: a small portion of the OPA signal output (∼10%) was siphoned from the pump beamline and underwent frequency-doubling in BBO to yield a horizontally-polarised beam. Any residual fundamental was removed from the beam using a band-pass filter and the remainder was left unattenuated; assuming typical 10% efficiency for SHG, the resultant beam possessed a maximum power equivalent to 1% of the overall OPA output before accounting for inevitable losses from numerous mirrors and transmissive optics. The probe was introduced into the same beamline used for broadband measurements, such that the path followed to the sample was identical for the two experiments. Note that these measurements did not employ any referencing; as such, the reference beam would be blocked for the course of these experiments.

Upon transmission through the sample, the probe beam was directed towards the single-channel detection station. There, a Wollaston prism was used to split the probe beam into two arms, with each encompassing the horizontal and vertical polarisation components. The intensity ratio was determined by whichever component dominated the input polarisation. Thus, for polarisation at 45° from horizontal, two beams of equal intensity would result. Conversely, at the two extremes of horizontally- or vertically-polarised probe, only one beam would emerge from the prism with full intensity. A lens situated after the prism would focus the two beams, which were then reflected from two mirrors onto a set of two bridged photodiodes (Thorlabs PDB210A/M). These possessed three output channels capable of monitoring the signal generated at

each of the two photodiodes individually, $S_|$ and S_-, or the difference between them, $\Delta S = S_| - S_-$.

The output from the difference channel was passed to a lock-in amplifier (Zurich Instruments MFLI) triggered by the laser system for signal demodulation. The various settings for this were controlled using a web browser-based app on an external computer, although data acquisition was performed using a LabVIEW program.

Prior to beginning the experiment, it was necessary for the detectors to be balanced as this afforded the greatest sensitivity to changes in the polarisation induced by either changing magnetic field or optical pumping. The input polarisation to the detectors would be set to 45° using a half-wave plate before the Wollaston prism. This was done precisely by monitoring ΔS and rotating the wave plate until the signal was minimised. When measuring MCD or time-resolved magnetic circular dichroism (TR-MCD), an additional quarter-wave plate would be inserted in front and the detectors balanced a second time; the additional wave plate in this instance was used to convert elliptical into linearly polarised light.

Any rotation induced in the probe beam can be determined through the ratio of ΔS to overall intensity. This is quantified by:

$$\theta_\mathrm{F} = \frac{1}{2} \times \arcsin\left(\frac{\Delta S}{2S_0}\right) \tag{2.7}$$

where S_0 is the difference signal measured with one photodiode blocked when the detectors are balanced, and thus $2S_0$ approximates the overall intensity of the beam. As $\theta_\mathrm{F} < 1°$, the small angle approximation can be made. Using this and a factor to convert from radians, the above is simplified to:

$$\theta_\mathrm{F} = \frac{180}{2\pi} \times \frac{\Delta S}{2S_0} \tag{2.8}$$

which gives θ_F in degrees. Note that the above equation is equally valid for measuring Faraday ellipticity using this scheme.

Magnetic hysteresis could be measured using this method by recording rotation as magnetic field was varied. Under these conditions, the trigger rate for the lock-in amplifier would simply be set to the laser repetition rate. TR-MO measurements instead triggered the lock-in amplifier at the pump modulation rate afforded by the optical chopper, thereby only detecting pump-induced response. For measurement of S_0 in this instance, the pump was blocked and the PHAROS's pulse picker would be used to halve the effective repetition rate to match that of the pump modulation frequency.

2.5.8 Sample positioning and electromagnet

For all optical measurements, samples were housed in an optical cryostat (Oxford Instruments MicrostatHe2). This was held under high vacuum ($<10^{-5}$ mbar) and could be cooled to 77 K using liquid nitrogen or 15 K using liquid helium if necessary for the experiment being performed. Temperature could be monitored and controlled using an external console (Oxford Instruments Mercury iTC).

The cryostat itself was situated between the poles of an electromagnet (GMW 3470) supplied with current by an external DC power supply (Aim-TTi CPX400SP). The poles were held at 26 mm separation and had holes drilled through the centre to allow the pump and probe through; as such, all magnetic fields were applied transverse to the sample plane and parallel to the probe propagation direction, which is shown in Fig. 2.12(a). With the aid of water cooling, the magnet could sustain currents up to 5 A, which would produce a magnetic field of 407 mT.

The cryostat was held in a purpose-built mount bolted to a translation stage (Zaber X-LSM025A-E03/X-VSR20A) capable of 2D movement transverse to the probe beam

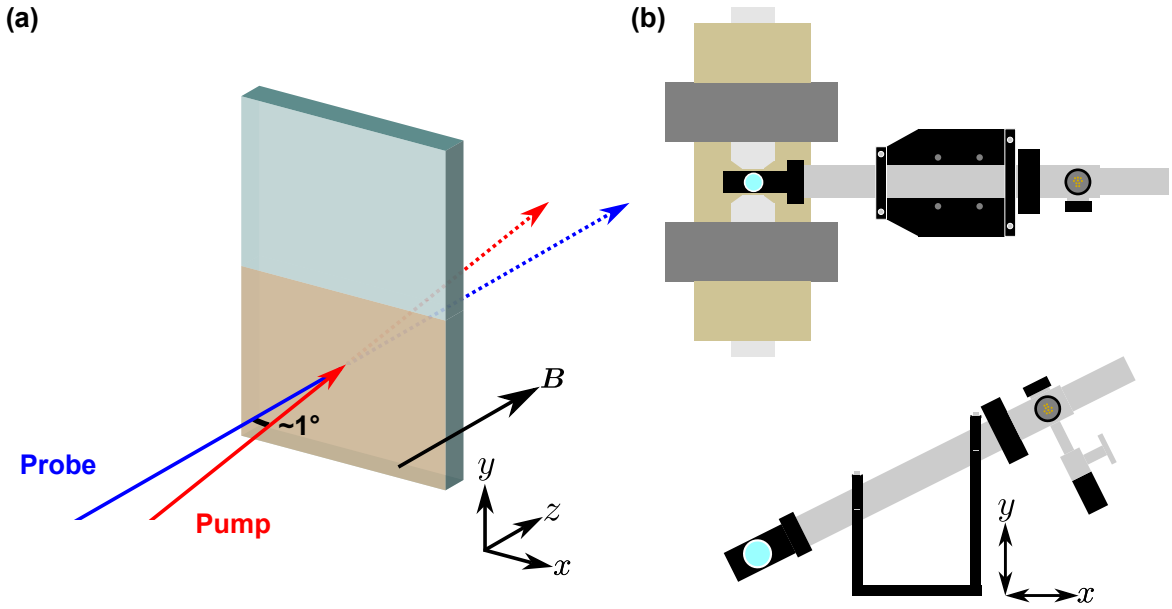

Fig. 2.12 (a) Schematic of the pump–probe beam geometry at the point of incidence on the sample: the probe passes through the sample at normal incidence (i.e. along the z-direction) and parallel/antiparallel to the $\boldsymbol{B}$-field, while the pump meets the probe at an angle of $\sim$1°. (b) Scale diagrams illustrating the sample mount and optical cryostat when viewed from above (top) and side-on (bottom). The electromagnet is included in the top-down view for context; the side-on view highlights the directions of motion available (x and y) for sample translation.

propagation direction; this is illustrated in Fig. 2.12(b). Using a lens/pick-off mirror after the electromagnet and a dedicated camera (Basler acA1920-25um), the position of the probe beam incident on the sample could be imaged through the cryostat windows. This allowed for selective probing of specific sites on the sample, and areas that appeared to scatter light more heavily could be avoided.

Through use of a dedicated LabVIEW program, it was possible to view a live feed of $\frac{I_{\text{probe}}}{I_{\text{ref}}}$ using the multi-channel detectors. Through comparison of this to a reference spectrum, the sample could be translated to maintain the same transmitted intensity between measurements, thereby reducing impact of pump-induced photodegradation and allowing for the effects of sample inhomogeneity to be mitigated.

2.5.9 Post-processing of data

Group velocity dispersion was observed for the white-light supercontinuum due to the frequency-dependence of refractive index for various optical elements; this caused the different frequency components to propagate at different phase velocities, and thus arrived at the sample at different times. This dispersion was positive – light was "chirped", meaning that higher frequency components trailed behind those of lower frequency, which was clearly observed for the TA data obtained. While possible to compensate for this by using a prism compressor, it was procedurally easier to correct for this in data post-processing.

Chirp correction was performed through manual selection of time-zero for a finite number of wavelength kinetic traces as indicated by the presence of a spectral artefact caused by XPM. A third-order polynomial function was then used to fit the data to bring time vectors across the spectrum in line with one another, followed by resampling of the data such that all wavelengths then possessed the original time vector. This process is illustrated in Fig. 2.13.

Baseline correction of ΔA was also typically performed on TA and TR-MO data in post-processing. Experiments included the measurement of TA/TR-MO response at $t_{\text{delay}} \ll 0$ — typically 5 time steps around -20 ps — for this purpose. These were averaged and subtracted from the data.

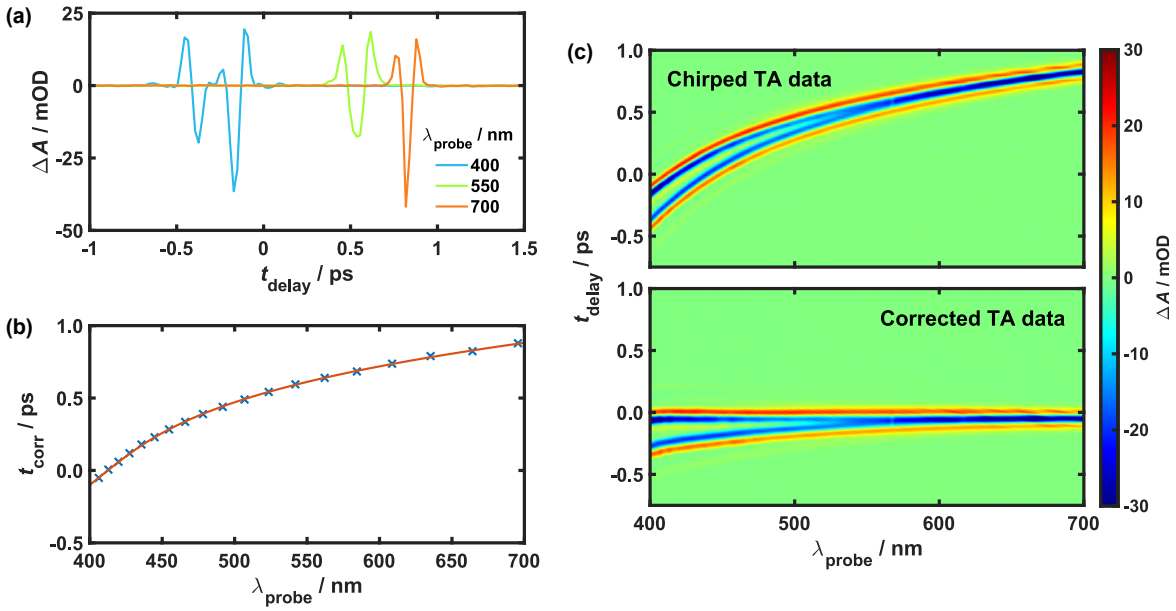

Fig. 2.13 Illustrated process for chirp correction of TA data. (a) t_0 is manually selected for different wavelengths based on the last peak of the XPM artefact that occurs when the pump and probe overlap in time. (b) Fitting with a 3rd order polynomial provides a vector of t_0 terms for each individual wavelength. (c) The 2D time array for the TA data is adjusted to unify t_0 for all wavelengths.

Chapter 3

Encapsulation of polycrystalline thin films

3.1 Project background

It is necessary to store V–Cr PBA in an anaerobic environment, as rapid air-oxidation of $V^{II} \longrightarrow V^{IV}O$ leads to suppression of the T_c and loss in colour [25]. Encapsulation of electrodeposited films using cyanoacrylate glue and a glass coverslip is sufficient to stave off oxidation while facilitating optical measurements, which has been reported by the Johansson group [41, 45, 70]. In the same vein, thin films of the organic-based ferrimagnet $V[TCNE]_{x\sim2}$, also air-sensitive, have also been encapsulated to prolong their lifetime using a UV-cured adhesive which was found to have no effect on the chemical composition or magnetic properties of the material [71].

Like the materials discussed above, Cr–Cr PBA is also known to undergo air-oxidation [49, 60], albeit less readily and without as severe a consequence for the spectral and magnetic properties. While Cr–Cr PBA is not strongly coloured (due to the MM′CT occurring in the UV), exposed films are nevertheless highly opaque due to

significant light scatter. It was observed that upon encapsulation, these films became highly transparent to the point where one could clearly read text through them.

The major obstacle to performing MO measurements on polycrystalline materials is light scatter: crystallites that have dimensions on the same scale as the wavelength of visible light will act to redirect it in random directions. This leads to attenuation of any transmitted beam and loss of coherent polarisation, thus decreasing signal/noise in polarimetric measurements. The enhanced transparency of encapsulated films was deemed to have the potential to overcome this and served as the motivation for this project.

The initial stages of this project were carried out by undergraduate student Jake Kirkpatrick (BSc Chemical Physics, 2020) as part of his Honours' programme. His selection of suitable encapsulation agents was retained for the work reported herein. The project was subsequently completed by myself and was subject to publication [47]. All data and analysis presented are my own.

3.2 Synthesis and encapsulation of films

Thin films of Cr–Cr and Fe–Cr PBA were synthesised for the purposes of this project using the electrodeposition procedure described in Section 2.1.1. Two encapsulation agents of known refractive index (n_{D}^{20} standard: reported for 589 nm at 20°C) were included in this study: cyanoacrylate glue ($n = 1.49$) and Norland optical adhesive 61 (NOA 61) ($n = 1.56$), which were both selected for their transparency across the visible region of the spectrum and ease of application. These were applied to the film using the procedure outlined in Section 2.1.2. A third agent, spectroscopic-grade mineral oil ($n = 1.47$), was also tested. However, it has no adhesive properties and so it was procedurally difficult to seal this between the film and a glass coverslip. Thus, data pertaining to these films have been omitted.

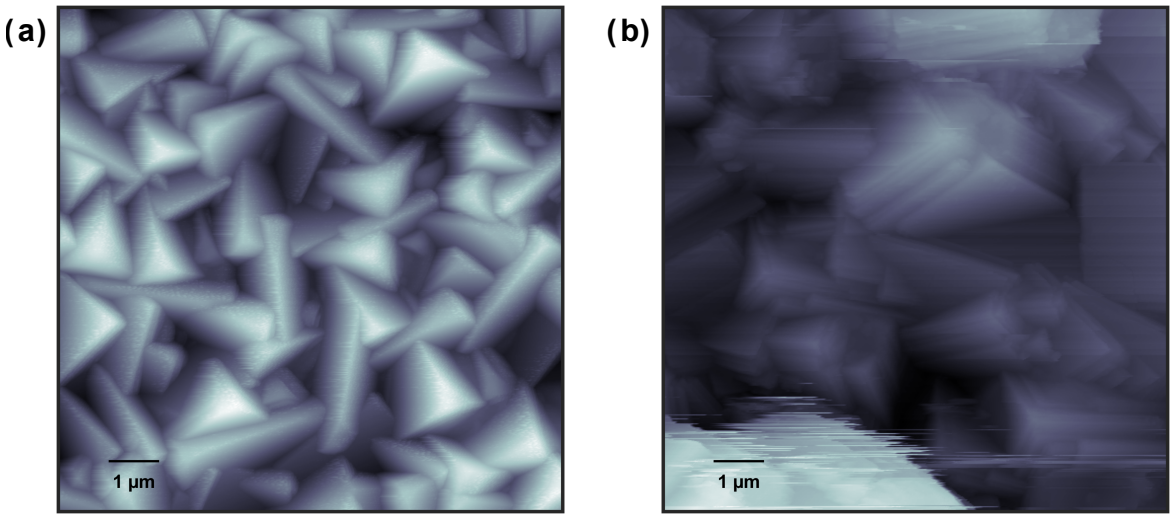

Fig. 3.1 AFM images showing typical surface morphology for (a) Cr–Cr and (b) Fe–Cr PBAs, from which surface roughness was calculated. Note that a foreign particle is present at the lower-left corner of (b); this area was omitted for the purposes of roughness calculation. Adapted from [47].

3.3 Characterisation of encapsulated films

3.3.1 Surface morphology

Morphological characterisation of Cr–Cr and Fe–Cr PBA films reported in the literature all conclude that the materials are polycrystalline in nature and possess inherently rough surfaces [49, 51, 53, 55, 60]. These characteristics were replicated in the films produced for this work, as illustrated by the AFM images shown in Fig. 3.1.

The Cr–Cr PBA film manifested as a collection of large cubic crystallites that were up to 1 µm in width. Thickness, d, was determined to be 1110(50) nm, suggesting that the film was only a few crystallites deep. The calculated root mean square surface roughness, R_q, was 207 nm. The Fe–Cr PBA film instead appeared to be comprised of wider, multiple layered sheets that were up to 2 µm wide. For this film, $d = 1100(200)$ nm; the greater uncertainty in thickness here can be attributed to the inherently rougher surface as $R_q = 313$ nm.

The roughness-to-thickness ratio, R_q/d, can be used as a measure of film heterogeneity with respect to depth. This was calculated to be 0.2 and 0.3 for Cr–Cr and Fe–Cr PBA, respectively. That the values are so high may indicate that the largest contribution to light scatter is from the film surface, thus supporting the notion that the number of scattering events could be reduced by artificial smoothing *via* encapsulation.

3.3.2 Vibrational spectroscopy

While TM cyanides are well-known for their resilience to ligand substitution, magnetic materials based on these have been observed to exhibit humidity-dependent properties [72, 73] or ligand-photodissociation in response to light [74]. Thus, it is pertinent that any encapsulation procedure used for PBAs does not in itself affect the composition of the films or their useful properties may be compromised. This is vitally important in the case of NOA 61 encapsulation, as exposure to UV light is necessary to cure it.

As highlighted in Section 2.2.2, vibrational spectroscopy is a powerful tool in characterising the composition of PBAs. Raman techniques are particularly helpful when applied to encapsulated films, as the laser beam is uninhibited by the presence of the coverslip. Thus, Raman spectra were obtained for Cr–Cr and Fe–Cr PBA films prior to and after encapsulation to assess whether the process appreciably affected the materials in any way; these are presented in Fig. 3.2.

The C≡N-stretch region of the Raman spectrum recorded for the exposed Cr–Cr PBA film featured one single asymmetric peak at 2193 cm^{-1}. Upon encapsulation, the peak instead appeared at 2195 cm^{-1} — a shift of only 2 cm^{-1} — while no new bands appeared. This suggests that no photochemistry was observed upon exposure to NOA 61 and curing by UV light. For Fe–Cr PBA, the Raman spectra for both exposed and encapsulated film overlapped, featuring a major peak at 2167 cm^{-1} and a

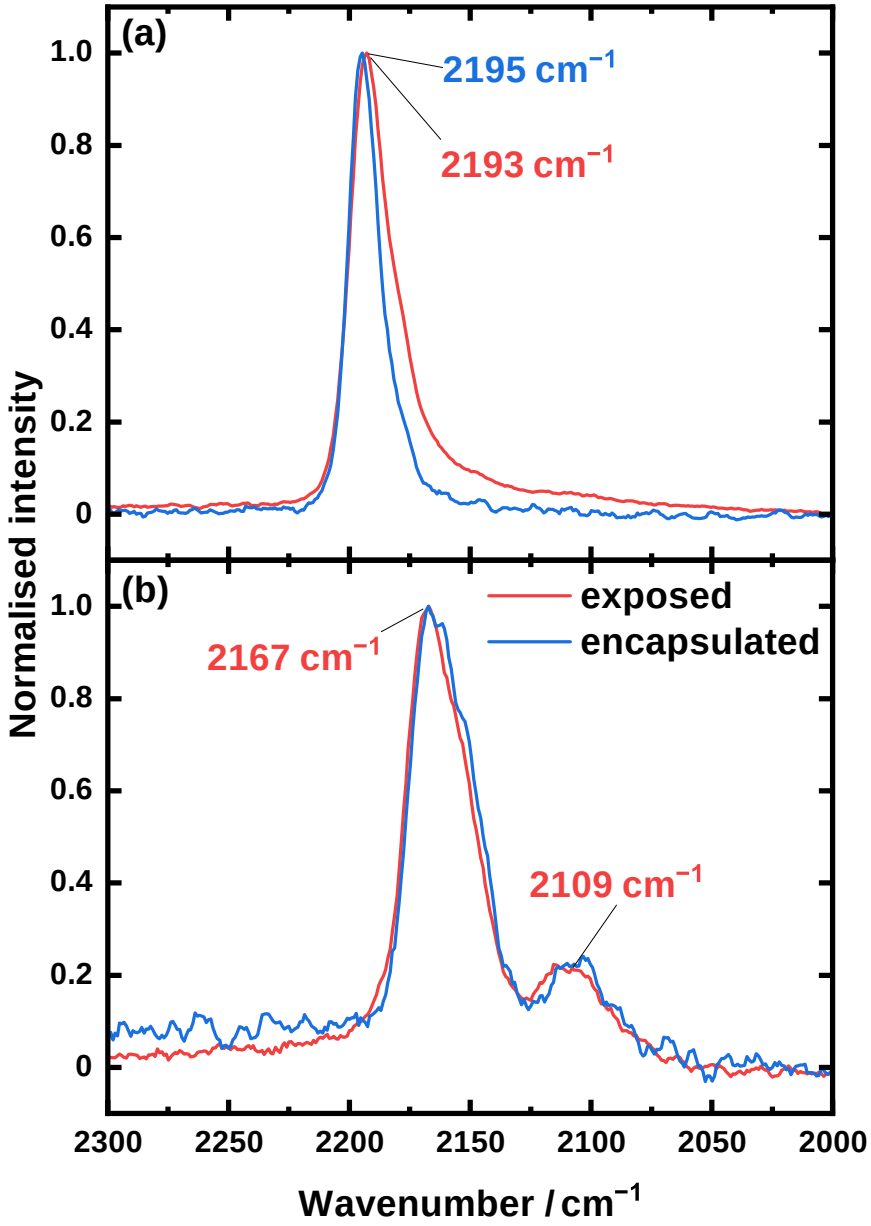

Fig. 3.2 Raman spectra recorded for (a) Cr–Cr and (b) Fe–Cr PBA films prior to (red) and following encapsulation (blue) with NOA 61. The frequencies of relevant C≡N stretch modes are highlighted. Adapted from [47].

minor peak at 2109 cm^{-1}. As discussed in Section 2.2.2, these are in accordance with literature [55]. The lack of any significant difference in the spectrum again indicates there was no change in composition of the film.

3.4 Quantifying improvement in transmittance

In accordance with the overall aim of suppressing light scatter, UV-visible-NIR transmittance spectra were recorded to gauge the opacity of the films before and after encapsulation. These are provided in Fig. 3.3.

It is clear that there was a dramatic increase in transmittance for both films. In the case of Cr–Cr PBA, overall transmittance for the exposed film was extremely poor and the spectrum largely featureless. Upon encapsulation, baseline transmittance was increased from 0.3 to 0.9 and even weaker transitions between 500–700 nm were discernible in addition to the stronger peak at 375 nm. For Fe–Cr PBA, baseline transmittance was also increased by the same amount and the broad MM′CT band became clearly defined. A much smaller peak at 800 nm could also be observed.

The improvement in transmittance could be attributed to a refractive index-matching effect upon encapsulation. Consider air and an exposed film to constitute two distinct optical phases, each with its own refractive index n. The polycrystalline morphology of the film would give rise to innumerable air/film interfaces with random orientation, each of which acts to scatter incoming photons along various directions. This results in attenuation of the beam transmitted along the original propagation direction (Fig. 3.4(a)), an effect which will be more profound when there is a greater mismatch between n_{air} and n_{film}. In the same vein, an encapsulated film consists of two optical phases, each again with its own associated n value. When n_{adhesive} and n_{film} are similar, the refractive properties of the two materials will closely matched and both can be considered a uniform optical phase. In this event, the propagation of

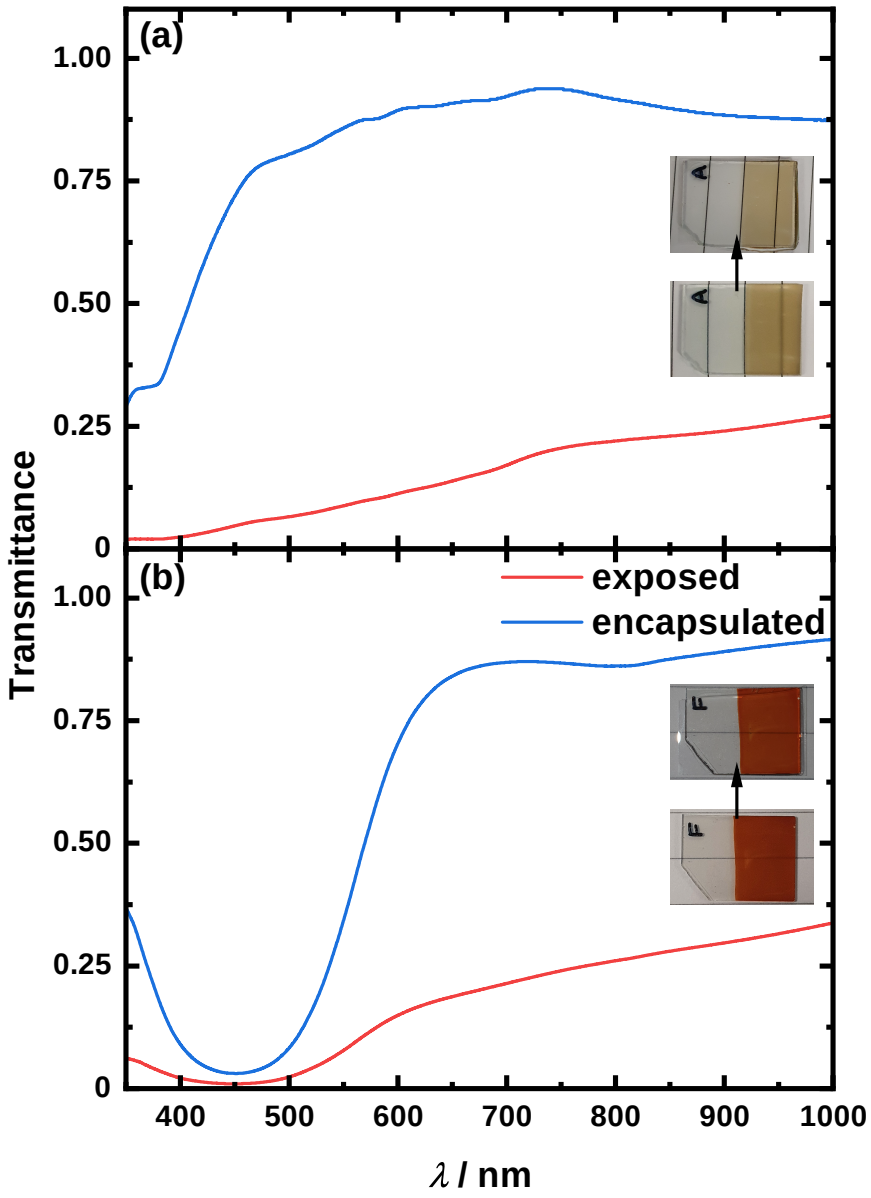

Fig. 3.3 UV-visible-NIR transmittance spectra for (a) Cr–Cr and (b) Fe–Cr PBA films prior to (red) and following encapsulation (blue) with NOA 61. Inset are initial and final photographs of each film. Adapted from [47].

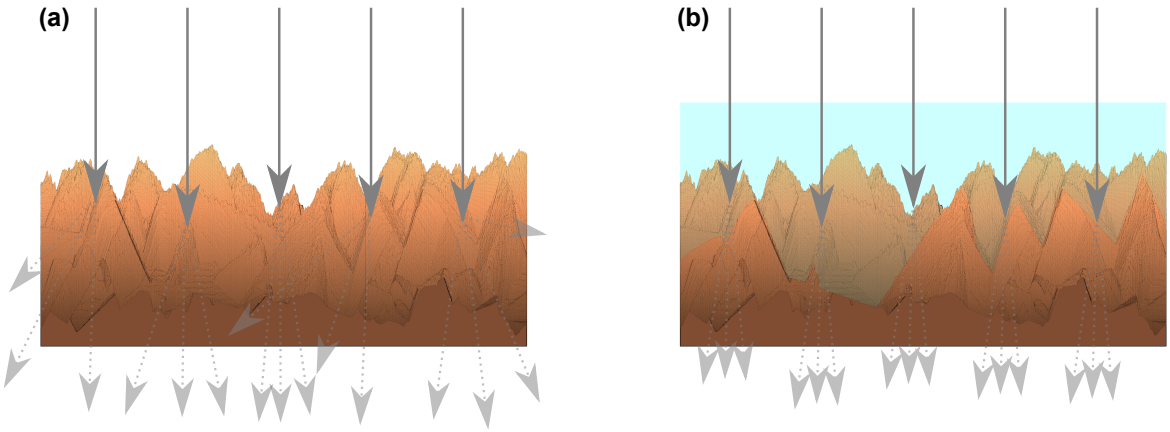

Fig. 3.4 Diagram illustrating light scattering events from a film's rough surface. (a) Light incident at the interface between air and the exposed film is scattered and redirected. There is a wide distribution of scattering vectors, resulting in attenuation of the transmitted beam. (b) Light incident on an encapsulated film passes through with little redirection. The distribution of scattering vectors is narrower, leading to retention of transmitted intensity.

light passing from the adhesive to the film will be unperturbed (Fig. 3.4(b)). Instead, scatter may primarily occur at the surface of the encapsulation agent.

If the improvement in transmittance can be attributed to better refractive index-matching between adhesive/film than air/film, it then follows that greater transmittance (and less scatter) will be afforded when $|n_{\text{film}} - n_{\text{adhesive}}|$ is minimised. As the value of n_{film} was unknown for both PBAs, this study employed trial and error to optimise the index-matching process using two encapsulation agents with known n. The improvement in optical clarity for each was quantified as the transmittance ratio between encapsulated and exposed films, $T_{\text{encap}}/T_{\text{exposed}}$. This was determined for films sealed with either cyanoacrylate glue or NOA 61 and is plotted with respect to wavelength in Fig. 3.5.

For Cr–Cr PBA, at least a fourfold increase in transmittance was observed upon encapsulation, which increased to more than tenfold at shorter wavelengths. The enhancement in transmittance was greater when NOA 61 was used over the cyanoacrylate glue, suggesting greater index-matching with the former. For Fe–Cr PBA, there was greater disparity in $T_{\text{encap}}/T_{\text{exposed}}$ between the two adhesives: NOA 61 was outclassed

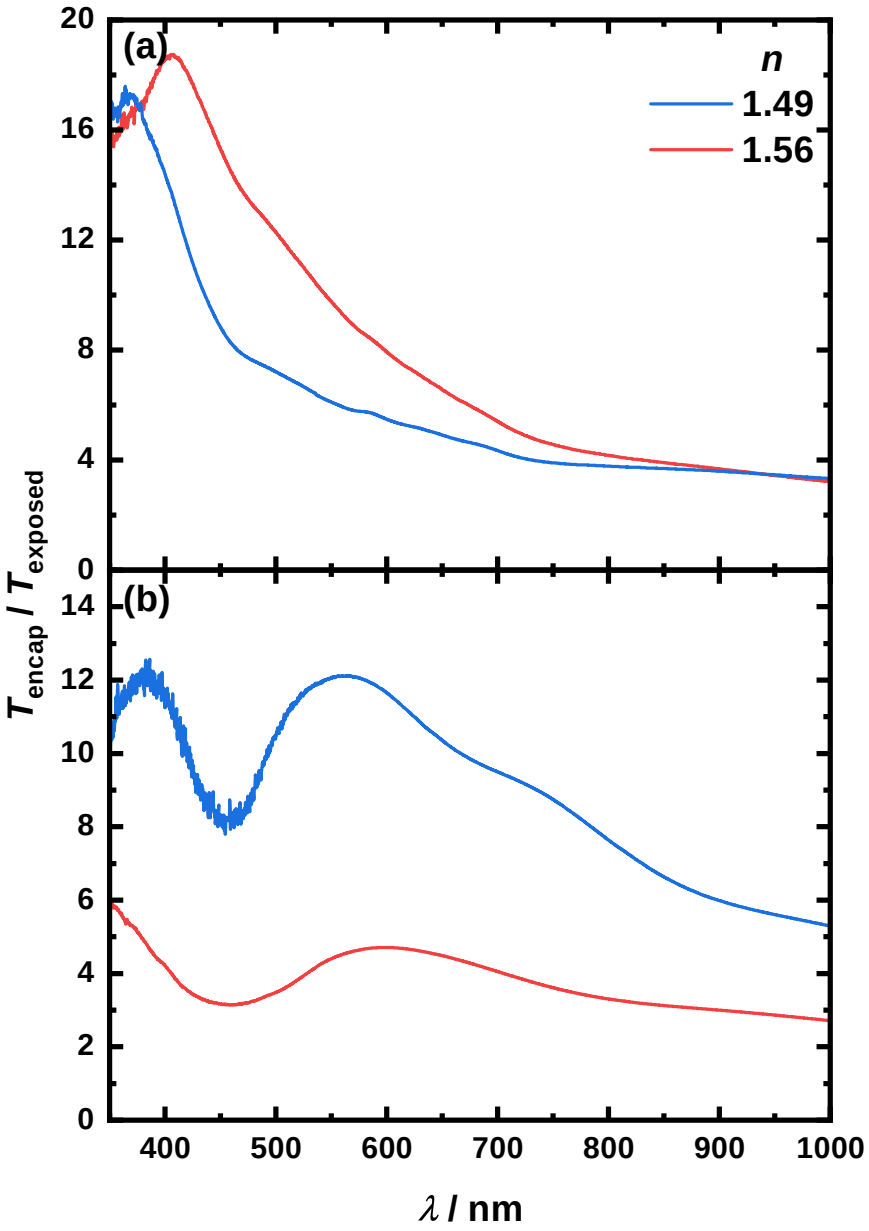

Fig. 3.5 $T_{\text{encap}}/T_{\text{exposed}}$ for (a) Cr–Cr and (b) Fe–Cr PBA films upon encapsulation with cyanoacrylate glue ($n = 1.49$ at 589 nm; blue) and NOA 61 ($n = 1.56$ at 589 nm; red). Adapted from [47].

by cyanoacrylate at every wavelength, suggesting greater index-matching with the latter adhesive in this case.

Irrespective of PBA or adhesive, $T_{\text{encap}}/T_{\text{exposed}}$ was shown to increase with decreasing wavelength. This is consistent with the trend followed by normal dispersion of light in dielectrics where n increases monotonically with frequency. Assuming that the PBAs also follow this behaviour, it is logical that encapsulation affords the greatest performance in the UV where $|n_{\text{film}} - n_{\text{air}}|$ will be greatest. This description appears to fail in the vicinity of the more intense transitions for the two films (e.g. Fe–Cr MM′CT at 450 nm), where $T_{\text{encap}}/T_{\text{exposed}}$ was shown to decrease. This is also consistent with the general behaviour of n, which possesses a derivative shape in the vicinity of frequencies close to resonance; in this region of the spectrum, $|n_{\text{film}} - n_{\text{air}}|$ may be smaller and thus the benefit from encapsulation reduced.

3.5 Magneto-optical hysteresis measured for an encapsulated film

The markedly improved transmittance of films upon encapsulation should be accompanied by increased retention of polarisation when a polarised beam passes through the material. Thus, an encapsulated Cr–Cr PBA film was subject to Faraday rotation measurements at low temperature in order to measure magnetic hysteresis. These results are provided in Fig. 3.6. Note that this film was significantly thicker than most exposed films had been when used in similar previous studies by our group.

The hysteresis loop measured for the film was clearly defined and noise-free. From this, the coercivity, $\mu_0 H_{\text{c}}$, was determined to be 15 mT. This concurs with similar results reported in literature [48, 60] and indicates that encapsulation of Cr–Cr PBA

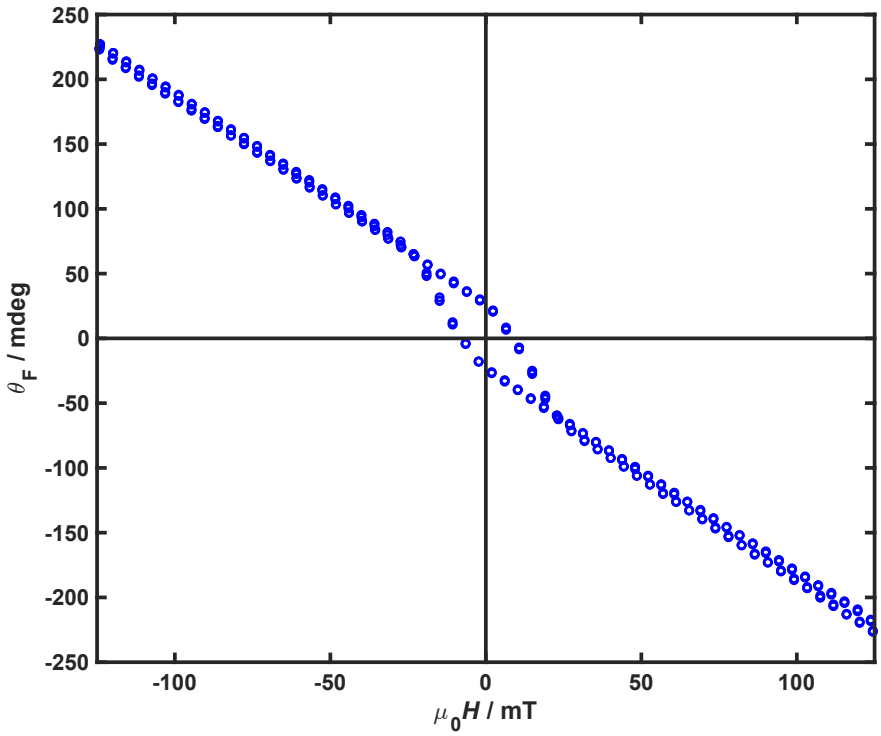

Fig. 3.6 Magnetic hysteresis observed in Cr–Cr PBA encapsulated with NOA 61 using Faraday rotation measurements. Data were collected at $T = 80\,\mathrm{K}$ using a 450 nm diode laser. Note that the linear background arises due to contribution from the film's substrate. Adapted from [47].

films with NOA 61 does not diminish their magnetic properties. Thus, films prepared in this way are fully compatible with transmission-based polarimetric techniques.

The relatively high T_c observed for Cr–Cr PBA allows magnetic ordering to be observed at liquid nitrogen temperatures, which were readily accessible for MO experiments in our lab. Conversely, the T_c reported for Fe–Cr PBA in literature is much lower and lies in the region of 19–24 K [52, 53, 55, 75]. As outlined in Section 2.5.8, the optical cryostat could be cooled to a base temperature of 15 K at the sample mount using liquid helium, which should (in principle) be sufficient to observe magnetic ordering in our Fe–Cr PBA films. However, magnetic hysteresis has not been successfully recorded for this material in our lab. Hence, the effect of encapsulation on its magnetic properties has not explicitly been investigated.

3.6 Conclusion

Encapsulation of polycrystalline PBA thin films with a suitable adhesive result in greatly reduced opacity and enhanced transmittance. This is attributed to better refractive index-matching between the film and adhesive than the film and air (i.e. $|n_{\text{film}} - n_{\text{adhesive}}| < |n_{\text{film}} - n_{\text{air}}|$), which mitigates light scatter at the film's surface due to formation of a uniform optical phase. This has obvious benefits in improved experimental performance when the film is subject to transmission-based spectroscopic or polarimetric techniques, such as TA and MO, and enables the use of thicker films for which the magnitude of the total MO response will be greater. The benefits are not just limited to enhancement of optical properties: encapsulation provides a barrier to the external environment and acts to protect films from abrasion and oxidation, as has also been demonstrated for V–Cr PBA [41, 45, 70] and V[TCNE]$_{x\sim2}$ [71].

It must be acknowledged that the work presented here only trialled two adhesives with very similar n. A logical continuation of this study would investigate the use

of other encapsulation agents with a much wider range of n values in an attempt to optimise the matching even further. Note that the agents employed need not be adhesive in nature; instead, transparent organic polymers could be used. These could be applied through spin coating, which is the method most likely to afford a thin, smooth coating upon the film's surface.

This study was effectively conducted through trial and error, without any *a priori* knowledge of n for the films subject to encapsulation. A more intelligent approach would involve determination of n in the first instance and selecting the most suitable encapsulation agents to employ based on this knowledge. This rationale has already been used in the design of layered photovoltaic structures in an attempt to minimise reflection from each component [76]. Spectroscopic ellipsometry could be used to determine the dielectric function for the film, from which n can be obtained. Ellipsometric characterisation has already been performed for thin films of Prussian blue, which determined n to be between 1.48 and 1.58 at 632.8 nm [77, 78]. While the findings of these investigations could provide a starting point for the optical modelling required, it should be noted that both studies approximated their films as a uniform optical phase. A more rigorous analysis would account for the inherent roughness of the films characterised throughout this chapter; such an approach has previously been demonstrated in $CH_3NH_3PbI_3$ perovskite, where polycrystalline thin films were modelled as a double-layer system comprising both bulk and surface "phases" [79].

While the outcome of this work has provided an overall improvement to thin film transmission, only losses at a single interface (i.e. air–film *vs.* adhesive–film) were considered for the sake of simplicity. In reality, the encapsulated films as presented possessed three material interfaces: air–coverslip, coverslip–adhesive and adhesive–film. Of these, the difference in refractive index for the air–coverslip interface is likely to be the largest ($|n_{\text{coverslip}} - n_{\text{air}}| = 0.52$); as such, the surface of the coverslip is likely to give

the greatest contribution to light scatter in encapsulated films. A more robust study would need to consider and suppress losses from each component, which would involve engineering a sample in which each constituent layer is selected to reduce the difference in n either side of each interface (i.e. minimise $|n_{\text{coverslip}} - n_{\text{air}}|$, $|n_{\text{adhesive}} - n_{\text{coverslip}}|$ and $|n_{\text{film}} - n_{\text{adhesive}}|$ simultaneously). Further to this, the effect of varying the thickness of each layer on the amount of light scatter observed should also be investigated to ensure that there is adequate coverage of the film's surface with the adhesive while also minimising any dispersion/absorption that might occur in the latter.

Note that while refractive index-matching in the films is desirable, this alone does not guarantee suitability of the encapsulation agent. For one, said agent must also not interfere with the techniques being employed. While NOA 61 was deemed to afford better index-matching in Cr–Cr PBA, it also absorbs heavily in the UV: the onset of absorption occurs at 380 nm, thus reducing transmission of UV light through the film and providing a barrier to short-wave optical pumping. In contrast, cyanoacrylate glue is transparent until much shorter wavelengths. The experimental conditions to be used must also be considered. It is notable that films our group have encapsulated with cyanoacrylate glue tend to have shorter shelf-lives: within a few cooling cycles, the coverslip has usually shattered, likely due to mismatch in thermal contraction of glass *vs.* the adhesive. Conversely, films encapsulated with NOA 61 have been subject to numerous experiments and cooling cycles over the course of many months before any delamination is observed.

Chapter 4

Electronic dynamics observed in aqueous hexacyanochromate(III)

4.1 Project background

The photophysics of Cr(III)-based TM complexes were summarised in Section 1.6, which emphasised how these d^3 systems possess low-lying, spin-flipped doublet states that can be accessed indirectly *via* ISC from states populated through photoexcited spin-allowed transitions. This has been demonstrated for $Cr(acac)_3$ in solution on ultrafast timescales by Juban and McCusker [40], which served as inspiration for the model proposed by Johansson *et al.* for the dynamics observed upon photoexcitation of LMCT in V–Cr PBA [41].

However, it should be noted that the optical properties of the hexacyanochromate(III) anion ($[Cr(CN)_6]^{3-}$), which serves as the molecular backbone for Cr(III)-based PBA, are not identical to those of $Cr(acac)_3$. Fundamentally, the nature of M–L bonding associated with the CN^- ligand is different than in $acac^-$: while complexes containing $acac^-$ are characterised by σ-donor/π-donor interactions, CN^- ligands give rise to much stronger σ-donor/π-acceptor interactions. Consequently, the ligand-field

splitting parameter, Δ, is much greater for CN^- than for $acac^-$. Thus, upon consultation of the d^3 Tanabe–Sugano diagram (Fig. 1.8 (a)), we would expect the energetic ordering of the states to be different, which would alter the available relaxation pathways upon photoexcitation. Additionally, the difference in the M–L interactions between $Cr(acac)_3$ and $[Cr(CN)_6]^{3-}$, as well as the reduced number of normal modes in the latter, would be expected to influence any vibrational dynamics observed. All of this could give rise to quite different behaviour in TA experiments.

In this chapter, the ultrafast photophysics observed in $[Cr(CN)_6]^{3-}$ will be presented with the aim of producing a more refined dynamical model to describe localised electronic dynamics in photoexcited Cr(III)-based PBAs, such as Cr–Cr and Fe–Cr thin films. As these are produced through electrodeposition from aqueous solution, TA measurements were performed on $K_3[Cr(CN)_6]$ dissolved in water. The primary reason for this is that experiments on species in solution are procedurally easy to perform compared to crystalline materials. The choice of solvent and counterion were the most appropriate to emulate the environmental conditions that $[Cr(CN)_6]^{3-}$ finds itself in when incorporated into a PBA: non-coordinated, zeolitic H_2O exists in the lattice and also fills A^{II} coordination sites in the proximity of $[Cr(CN)_6]^{3-}$ vacancies, while K^+ is incorporated into interstitial sites throughout the PBA.

4.2 Summary of dynamics in $Cr(acac)_3$

As stated above, the interpretation of the Cr(III)-centred dynamics in V–Cr PBA was based on those observed for ultrafast TA on $Cr(acac)_3$ in solution. While these findings were briefly touched upon in Chapter 1, they will be considered in a greater level of detail here to inform a predictive model for the dynamics in $[Cr(CN)_6]^{3-}$ and later aid in experimental interpretation.

Juban and McCusker reported the observation of a single ESA band in the visible ($\lambda_{max} = 520$ nm) upon ligand-field excitation [40]. This feature formed within their experimental time resolution (<100 fs) and on short timescales conformed to monoexponential kinetics ($\tau = 1.1$ ps). Subsequently, the ESA was not observed to fully decay until protracted timescales ($\tau \sim 700$ ps). This is illustrated in Fig. 4.1(a).

In assigning the ESA feature to a specific transition, the authors considered the electronic structure for both the $^4T_2$ and ^2E states. They concluded that the LMCT transitions from each should have distinct spectra: $^4LMCT \leftarrow {}^4T_2$ would correspond to significantly lower energy than $^2LMCT \leftarrow {}^2E$, although the widths of the two bands would be expected to be similar. This is on account of the electronic configuration of the $^4T_2$ state possessing a vacant t_{2g} orbital into which electron transfer can occur from the ligand. In contrast, the t_{2g} orbitals for the ^2E state are all singly occupied and thus electron transfer from the ligand would require spin pairing; the associated energy penalty would therefore increase the energy of the $^2LMCT \leftarrow {}^2E$ transition. The lack of any significant ESA evolution featuring more than one band indicated that the TA observed pertained to the population dynamics of just a single excited state. Based on the apparent time taken for ground state recovery to occur, this state was judged to be ^2E.

The absence of any spectral signature pertaining to the $^4T_2$ state was attributed to ISC occurring faster than the experimental time resolution, with $\tau_{ISC} < 100$ fs. The

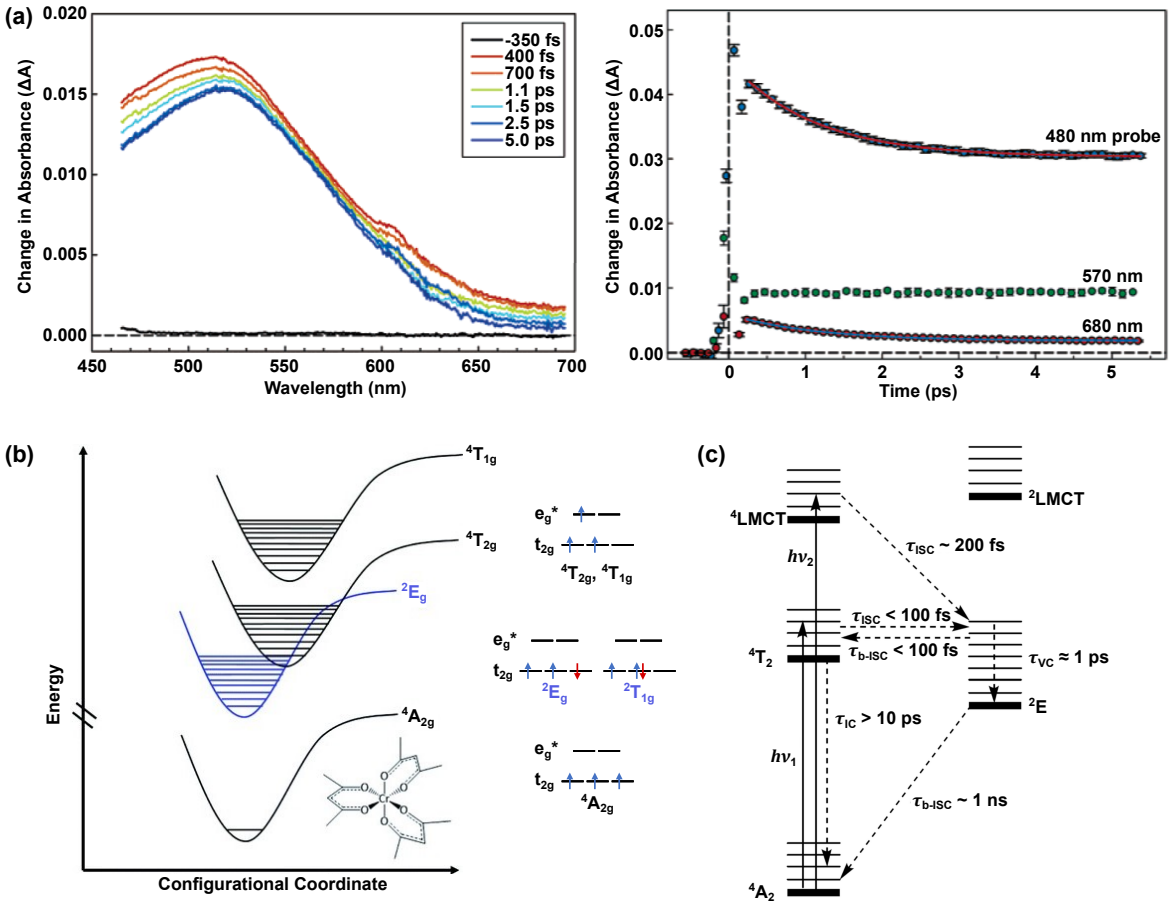

Fig. 4.1 Summary of the dynamics observed upon ligand-field photoexcitation in $Cr(acac)_3$. (a) Experimental difference spectra (left) and kinetic traces with accompanied fits (right). (b) Simplified potential energy surfaces of relevant electronic states and their corresponding electronic configurations. (c) Jablonski diagram illustrating the relaxation pathways available upon photoexcitation of ligand-field (625 nm, $h\nu_1$) and LMCT (335 nm, $h\nu_2$) transitions alongside their associated time constants. Panel (a) taken from [40]; panels (b) and (c) adapted from [80].

remaining fast decay component of the kinetics appeared to coincide with spectral narrowing observed on ∼1 ps timescales, which was attributed to vibrational cooling. While subsequent transient IR absorption studies would largely validate these findings, they identified an additional relaxation pathway which would occur through back-ISC from the doublet to quartet manifold ($^4T_2 \leftarrow {}^2E$) on similar timescales to the forward process (<100 fs). This would then be followed by internal conversion (IC) back to the ground state with $\tau_{IC} = 15$ ps [81, 82]. A Jablonski diagram highlighting the kinetic pathways determined by these experiments is provided in Fig. 4.1(c).

4.3 Photophysics of hexacyanochromate(III)

The photophysics of $[Cr(CN)_6]^{3-}$ in various media have been well-studied since the 1960s. Its electronic spectrum is characterised by spin-allowed ligand-field transitions at 379 nm ($^4T_2 \leftarrow {}^4A_2$) and 308 nm ($^4T_1 \leftarrow {}^4A_2$), and spin-forbidden transitions at 801 nm ($^2E \leftarrow {}^4A_2$) and 525 nm ($^2T_2 \leftarrow {}^4A_2$) [83–86], which are illustrated in Fig. 4.2. The onset of the charge transfer manifold occurs at 260 nm [84, 86, 87], with which a third ligand-field transition ($^4T_1 \leftarrow {}^4A_2$) overlaps.

Calculated values of the Racah parameter B for $[Cr(CN)_6]^{3-}$ range from 480 to 590 cm^{-1} [83, 84, 88]: all of these suggest $\Delta/B > 45$. Within this regime, the energy of the $^4T_2$ state significantly surpasses that of ^2E, between which the intermediate $^2T_2$ state lies. This is summarised in the scaled Jablonski diagram provided in Fig. 4.2 (b).

It is important to note that this differs significantly from the electronic structure of $Cr(acac)_3$, for which $\Delta/B < 30$ and thus the $^4T_2$–^2E energy gap is much narrower. One consequence of this is that upon ligand-field excitation in $[Cr(CN)_6]^{3-}$, any relaxation pathway through the doublet manifold would likely first pass through the higher $^2T_2$ state upon ISC. This would deactivate to ^2E *via* $^2T_1$ [89] through IC, which may add an additional time component into the dynamics *vs.* $Cr(acac)_3$. Note that all three of

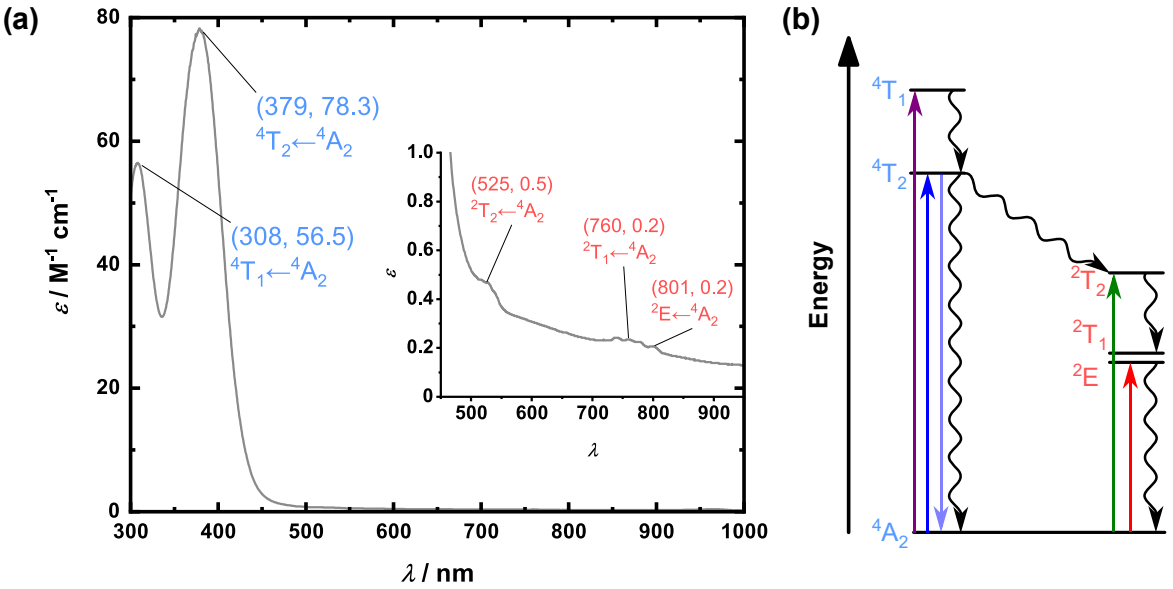

Fig. 4.2 (a) Electronic spectrum for $[Cr(CN)_6]^{3-}$ in aqueous solution, with inset highlighting the region containing spin-forbidden transitions. Peaks are labelled with their assigned transitions. (b) Jablonski diagram illustrating the relative energies of the lowest-lying quartet (blue) and doublet (pink) states.

these doublet states are intraconfigurational: the overall d-electron configuration is $t_{2g}{}^3e_g{}^0$. This means that there will be very little distortion of the complex from ground state geometry, resulting in highly parallel potential energy surfaces that are nested within that of $^4A_2$.

Another thing to consider in the photophysics of $[Cr(CN)_6]^{3-}$ is the efficiency of ISC, which is the fraction of initially populated $^4T_2$ that reaches the doublet manifold [34, 39]. For the complex in solution, this has been determined to be ~0.5 [89, 90], which is low compared to many other Cr(III) complexes [39]. One study has suggested that IC competes effectively with ISC to depopulate the ligand-field state upon photoexcitation, with a purported efficiency of >0.4 [89]. In the presence of coordinating solvents, the efficiency of the ISC pathway will be further hampered by photochemistry: photosubstitution of $[Cr(CN)_6]^{3-}$ has been reported [85, 91–93], where the $^4T_2$ state was identified as being photochemically active [91]. Thus, features arising

from photochemical behaviour may manifest in any potential ultrafast experiment, likely at the expense of signatures relating to the doublet manifold.

On a related note, studies of photoluminescence in $[Cr(CN)_6]^{3-}$ dissolved in dimethylformamide at room temperature have found that the presence of O_2 in solution reduces the doublet emission lifetime by a factor of 10, while the use of H_2O as a solvent instead quenches it altogether [91]. While the mechanism of said action has not been thoroughly investigated, it is clear that the presence of these species in solution provides some alternative relaxation pathway to accelerate deactivation of the ^2E state [91]. This implies that any spectral features in ultrafast TA experiments arising from the doublet manifold could also potentially be very short-lived.

4.4 Ultrafast transient absorption

TA measurements were performed on $[Cr(CN)_6]^{3-}$ with the aim of investigating the dynamics that ensue upon photoexcitation of the first two spin-allowed ligand-field transitions ($^4T_2 \leftarrow {}^4A_2$ and $^4T_1 \leftarrow {}^4A_2$). The specific procedural details are outlined as follows.

The experiments employed the multi-channel detection scheme described in Section 2.5.6 at 1 kHz repetition rate. For ligand-field excitation, pump wavelengths were selected which coincided with the red-end of the corresponding band in order to minimise deposition of excess vibrational energy. To suppress any scattered pump light which could obscure features observed in the TA spectrum, a Glan laser polariser was matched to the probe polarisation and situated after the sample.

For these experiments, $K_3[Cr(CN)_6]$ was dissolved in water to yield a solution of concentration 58 mmol l^{-1} and held in a 1 mm path length flow cuvette. This resulted in an optical density of 0.3 at 400 nm. Because photosubstitution of CN^- by H_2O has been reported [85, 91], efforts were made to mitigate the effect of sample

photodegradation by the pump. The solution itself was flowed at a rate of 16 µl min^{-1}; if the volume of sample excited is approximated as cylindrical with facial area equal to incident pump area and length equal to path length, this flow rate fully exchanged the number of molecules in the beam path every 29 pump pulses.

4.4.1 Ligand-field excitation at 400 nm

The first ligand-field transition was excited using a 400 nm pump. Measurements investigating laser fluence-dependence confirmed that TA response was linear up to the maximum fluence that could be generated at 2.5 mJ cm^{-2}. Within this range, it could be assumed that single-photon absorption would be observed. Thus, the full TA spectrum was recorded for a pump fluence of 2.5 mJ cm^{-2} and polarisation set perpendicular to that of the probe. This is shown in Fig. 4.3.

Upon inspection of the difference spectra, a broad ESA feature centred at 375 nm is observed; this is Gaussian in shape and dominates the TA response at early times. Decay of this feature coincides with growth of a much narrower, secondary ESA feature centred at 383 nm which can only just be observed at 1 ps and has fully formed within 10 ps. The kinetic traces corroborate this, which show monotonic decrease in ΔA for wavelengths either side of the secondary band, but a growth in intensity at the peak within 5 ps. It must also be noted that even by 1 ns, there is still a significant amount of ESA. This suggests that ground-state recovery occurs on much greater timescales.

Determining bleach contribution

It is notable that the ESA appears to overlap almost exactly with the steady-state absorption spectrum, from which we would expect to see negative ΔA contributions as a result of GSB. As the total difference spectra arise from the summation of these components, this would lead to an underestimated magnitude for the ESA feature.

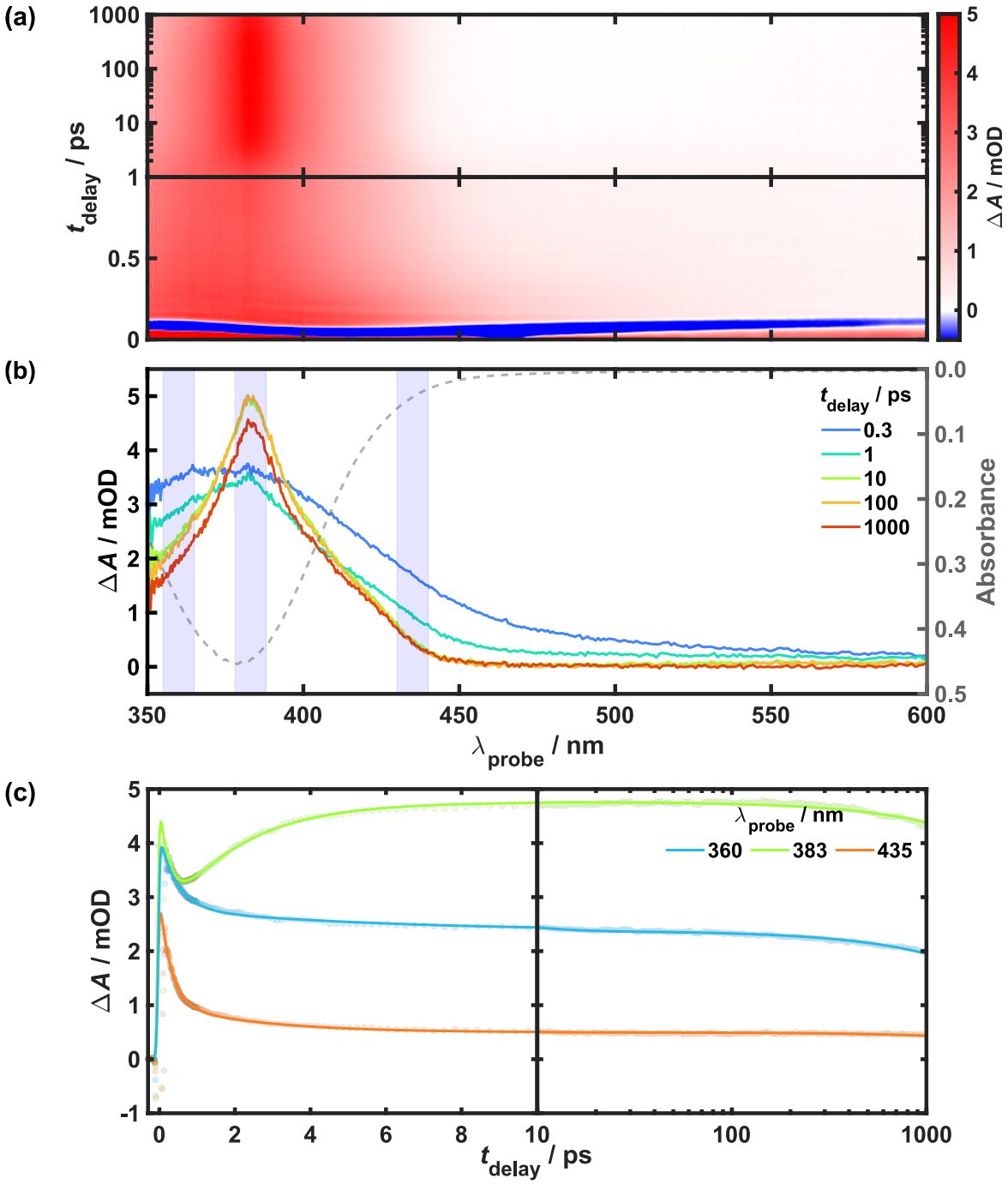

Fig. 4.3 (a) TA spectrum obtained for $[Cr(CN)_6]^{3-}$ in H_2O upon photoexcitation with a 400 nm pump of linear (vertical) polarisation and fluence 2.5 mJ cm^{-2}. Note that the intense bands observed across the whole spectrum at $t_{delay} = 0$ ps arise from non-linear artefacts. (b) Difference spectra obtained at discrete time delays (coloured, left axis). Overlaid is the steady-state absorbance spectrum recorded at the same temperature for reference (dotted, right axis). Wavelength bands of interest for kinetic analysis are highlighted in blue; these regions were averaged and used to construct kinetic traces. (c) Raw kinetic data (circles) for selected wavelength bands and corresponding fits (solid lines).

To investigate the extent of this, the GSB contribution can be estimated using the steady-state absorption spectrum and the fraction of photoexcited molecules.

Firstly, it can be assumed that for a linear (i.e. single-photon) absorption process, the number of photons absorbed can be equated to the number of molecules excited. If transmittance, T, is obtained from absorbance, A, by:

$$T = 10^{-A}$$

then the fraction of photons absorbed is:

$$1 - T = 1 - 10^{-A} \tag{4.1}$$

Using the pump fluence, F, and energy per photon, E, the number of photons incident on a given area is provided by:

$$F/E = F\lambda/hc \tag{4.2}$$

Through combining the expressions 4.1 and 4.2, the number of photons absorbed per unit area is given by:

$$\frac{\left(1 - 10^{-\epsilon c_0 \ell}\right) F\lambda}{hc}$$

where absorbance has been replaced with $A = \epsilon c_0 \ell$, as per the Beer-Lambert law for solution. Assuming a circular beam incident on the sample with radius r, the total number of photons absorbed, N_{photon}, is obtained by:

$$N_{\text{photon}} = \frac{\left(1 - 10^{-\epsilon c_0 \ell}\right) F\lambda\pi r^2}{hc}$$

The volume of the sample irradiated by the pump is again approximated as cylindrical with length ℓ. Therefore, volume V is obtained by:

$$V = \ell \pi r^2$$

and the total number of molecules, $N_{\text{molecules}}$, within this volume is given by:

$$N_{\text{molecules}} = N_A c_0 V = N_A c_0 \ell \pi r^2$$

where N_A is Avogadro's number.

Since N_{photon} is equal to the total number of excited molecules, the fraction of the sample excited can be determined from $N_{\text{photon}}/N_{\text{molecules}}$. This is denoted κ, and is obtained through the expression:

$$\kappa = \frac{\left(1 - 10^{-\epsilon c_0 \ell}\right) F \lambda}{hc N_A c_0 \ell} \tag{4.3}$$

which is independent of r and thus the specific focussing conditions for the pump beam.

Upon substitution of various experimental parameters ($\epsilon_{400\text{nm}} = 56$ M^{-1} cm^{-1}, as obtained from Fig. 4.2; $c_0 = 58$ mmol l^{-1}; $\ell = 1$ mm; $F = 2.5$ mJ cm^{-2}; $\lambda_{\text{pump}} = 400$ nm), κ is estimated to be 0.0008, or <0.1%. Multiplication of the steady-state spectrum by this factor results in an insignificant GSB contribution ($\Delta A_{\text{GSB}} \approx 0.001$ mOD) to the overall signal compared to the ESA. As the ratio of $\Delta A_{\text{ESA}}/\Delta A_{\text{GSB}} \approx 3000$, it can be surmised that $\epsilon_{\text{ESA}} \gg \epsilon_{\text{GSB}}$ and thus the ESA arises from an excited state charge-transfer transition.

Discrete kinetic analysis

In the first instance, kinetic analyses were performed on the time-dependent data presented in Fig. 4.3(c). The initial model assumed a parallel decay scheme consisting of n independent decay pathways that conform to exponential kinetics. This is given by:

$$f(\lambda, t) = \sum_{i=1}^{n} A_i \exp\left(-\frac{(t - t_0)}{\tau_i}\right) \tag{4.4}$$

where A_i and τ_i are the amplitude and time constant of each component i for a given wavelength λ, respectively. $(t - t_0)$ accounts for any slight offset in time-zero which may arise due to imperfect chirp correction by inclusion of t_0 as another fitting parameter.

Note that the kinetic model described above assumes instantaneous excitation of the sample, after which the response immediately decays. In the context of the pump–probe experiment, this is not the case: instead of being infinitely short, the pump pulse possesses a finite width over which the sample acquires its energy. Thus, the signal will possess a finite rise-time and an initially broadened decay that are determined by a cross-correlation function accounting for the temporal width of both the pump and probe pulses. This is known as the instrument response function (IRF), which can be represented by a Gaussian centred at t_0 with width w:

$$IRF(\lambda, t) = \exp\left(-\frac{(t - t_0)^2}{2w^2}\right) \tag{4.5}$$

To properly account for the growth of the signal and thus the early-time dynamics, it is necessary to incorporate the IRF into the kinetic model. This is achieved through convolution of Eq. 4.4 with Eq. 4.5:

$$\begin{aligned} g(\lambda, t) &= [IRF * f](\lambda, t) \\ &= \int_{-\infty}^{\infty} IRF(\lambda, t - u) f(\lambda, u)\, \mathrm{d}u \end{aligned}$$

where expansion of the integral and simplifying the resultant expression yields [94, 95]:

$$g(\lambda, t) = \sum_{i=1}^{n} A_i \exp\left(\frac{w^2}{2\tau_i^2} - \frac{(t-t_0)}{\tau_i}\right)\left[1 + \mathrm{erf}\left(\frac{(t-t_0) - w^2\tau_i}{\sqrt{2}w}\right)\right] \tag{4.6}$$

To aid modelling of the data, the w and t_0 parameters were subject to constraints using information obtained *a priori*. It was assumed that chirp correction was reasonably accurate and that t_0 should not vary by more than 100 fs either side of the already determined time-zero. TA measurements performed on neat solvent using the same experimental conditions (pump wavelength, fluence, array of time delays, etc.) were fitted with a phenomenological model comprising the sum of a Gaussian and its first two derivatives to ascertain w from the non-linear artefact at time-zero, which is an approach suggested in literature [95, 96]. From this, w was determined to range between 40 and 60 fs, depending on probe wavelength. Thus, these were the bounds used for w in the kinetic model. As the presence of XPM would greatly hinder the modelling by providing exaggerated decay rates for early timescales, all ΔA values corresponding to $-0.15 < t_{\mathrm{delay}} < 0.15$ ps were omitted from the fitting.

The model described by Eq. 4.6 was fitted to the three wavelength traces using a non-linear least squares algorithm. The bands all conformed best to triexponential kinetics (i.e. $n = 3$) with $R^2 > 0.99$. The fitted data are presented in Fig. 4.3(c), while the fit parameters obtained are summarised in Table 4.1. All three fits identified fast ($\tau_1 < 0.5$ ps), intermediate ($1.94 < \tau_2 < 5.6$ ps) and very slow ($\tau_3 > 5000$ ps) time components with varying amplitudes. τ_1 in each case was associated with an initial sub-ps decay in each trace, while τ_3 corresponds to a very slow decay that occurs on timescales beyond the maximum time delay that is accessible with the measurement. As such, the uncertainty in this value is particularly large compared to the others. While τ_2 corresponds to an additional decay component in the 360 and 435 nm traces

Table 4.1 Fit parameters obtained from kinetic analysis of the TA data presented in Fig. 4.3(c).

λ_{probe} / nm	Amplitude / mOD			Time constant / ps		
	A_1	A_2	A_3	τ_1	τ_2	τ_3
360	0.7(2)	0.21(2)	1.187(2)	0.47(2)	5.6(4)	5100(100)
383	1.4(2)	−0.123(4)	2.381(2)	0.29(1)	1.94(4)	12000(400)
435	1.1(2)	0.27(5)	0.248(6)	0.300(7)	2.5(1)	7500(900)

either side of the secondary ESA band, this is instead associated with signal growth at the centre of the band and possesses negative amplitude.

Lineshape and spectral decomposition analysis

For assignment of kinetic processes, it is essential to disentangle any change in amplitude of spectral bands from shifts in peak position or bandwidth. In the event of overlapping spectral components, as appears to be the case in the ESA of the spectra presented, this process is non-trivial and is best performed through decomposition analysis. For this purpose, a dedicated software package (KOALA v1.1 [97]) was used to fit difference spectra at any given time delay as the sum of a number of different basis functions used to represent the shapes of the constituent bands.

To assist in the fitting process, the TA data at each time delay was resampled using linear interpolation to conform to an evenly spaced wavelength array consisting of 100 points. The wavelength array was then converted to wavenumber, which is a more appropriate representation for lineshape analysis [95]. Difference spectra were fitted with a phenomenological model comprising the summation of two Gaussian functions to represent the two apparent ESA components. Early time delays ($t_{delay} < 0.2$ ps), where the effect of XPM could be observed in the difference spectra, were omitted from the fitting. The initially formed, broader ESA feature (denoted ESA_1) was allowed to vary in both central position and width over time, while the secondary, narrower ESA

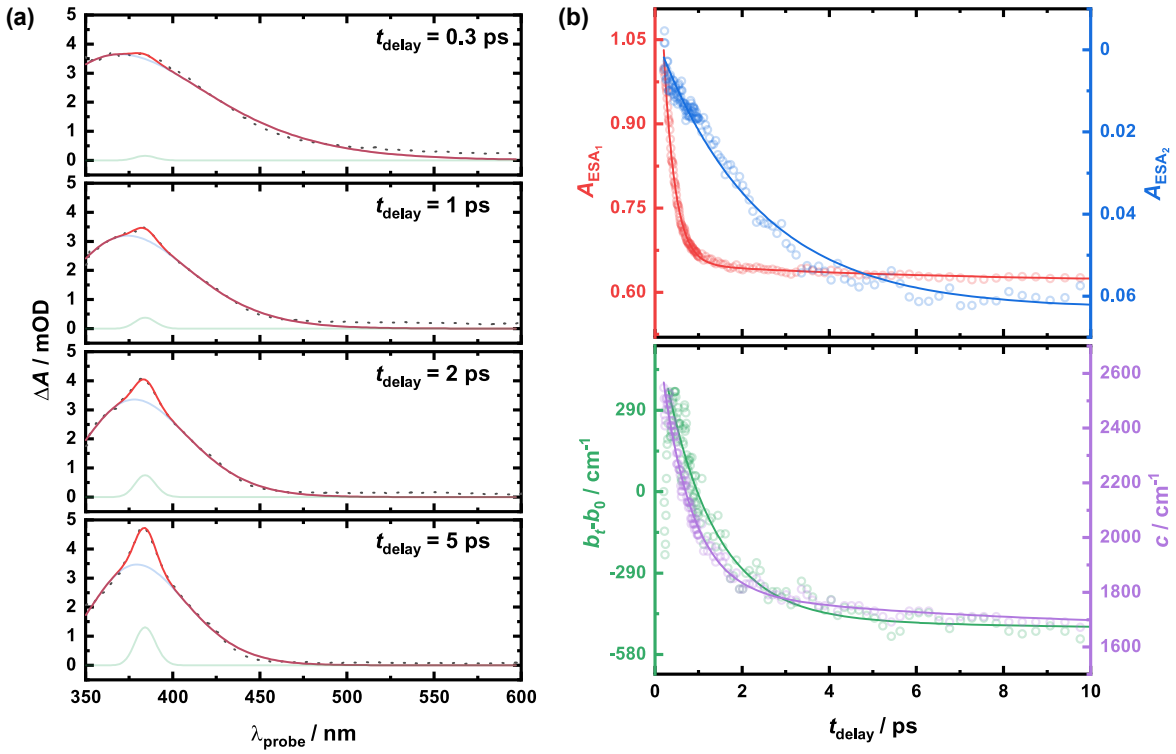

Fig. 4.4 Spectral decomposition of data presented in Fig. 4.3. (a) Difference spectra fitted using a spectral decomposition software package for selected time delays. Overlaid are experimental data (black dots), total fits (red lines), and the two Gaussian functions that comprise the total fit (blue and green lines). (b) Evolution of Gaussian lineshape for the two ESA components with respect to time delay. Top: change in peak area A under each ESA component. Note that the A_{ESA_2} y-scale is reversed for easier visual comparison of kinetic timescales. Bottom: change in central position and bandwidth of ESA_1. Computed values in both panels are represented by hollow circles while fits are represented by solid lines.

(denoted ESA_2) had its central position and width first selected by eye, then fixed. The outcome of the fitting for four time delays is presented in Fig. 4.4(a).

The lineshape fits conformed well to the experimental data at each time delay, with the main disparity being the tail of the ESA beyond 450 nm where signal is close to zero. Note that use of alternative basis functions, such as Lorentzian, did not improve the fit. Likewise, inclusion of the steady-state spectrum as a basis function to account for any GSB contribution did not affect the fit at all as it was assigned near-zero

Table 4.2 Fitted kinetic timescales for time-dependent data presented in Fig. 4.4(b). The value labelled with (*) is associated with growth in amplitude while the others exhibit only decay.

Fit parameter	Time constant / ps		
	τ_{fast}	τ_{int}	τ_{slow}
A_{ESA_1}	0.260	5.8	10^4
A_{ESA_2}	2.33(*)	-	10^6
$b_t - b_0$	1.15	40	-
c	0.7	8	-

amplitude at all time delays. This is consistent with the very small magnitude of the GSB contribution estimated previously.

The adjustable parameters for the two Gaussian components were logged for each time delay. These were fitted with simple multiexponential decays (two or three terms, as appropriate) and are plotted in Fig. 4.4(b), with relevant time constants summarised in Table 4.2.

The areas of the two Gaussian ESA components are observed to evolve at different rates: A_{ESA_1} initially decays on much faster timescales than the growth of A_{ESA_2} ($\tau = 0.260$ *vs.* 2.33 ps). These two values are again consistent with τ_1 and τ_2 obtained for discrete fitting of the 383 and 435 nm traces. The kinetics for A_{ESA_1} also conform to another decay process ($\tau = 5.8$ ps) which has no analogous feature in A_{ESA_2}. This appears to coincide with τ_2 associated with decay at 360 nm. Both A_{ESA_1} and A_{ESA_2} are observed to undergo decay on protracted timescales that exceed the maximum time delay reached in the measurement ($\tau \gg 1500$ ps), which has already been ascribed to ground-state recovery.

For ESA_1, the shift in central band position, $b_t - b_0$, is observed to sharply increase by 300 cm^{-1} between 0.2 and 0.5 ps, indicating an initial blueshift. After this, $b_t - b_0$ decreases to ~ -500 cm^{-1} at a rate conforming to biexponential kinetics with fast and slow components ($\tau_{\text{fast}} = 1.15$ ps and $\tau_{\text{int}} = 40$ ps). Bandwidth c initially starts off

wide and narrows over time; again, this appears to conform to biexponential kinetics with fast and slow components ($\tau_{\text{fast}} = 0.70$ ps and $\tau_{\text{int}} = 8$ ps), with a total reduction of ∼36%. Notably, none of these time components associated with lineshape evolution could be discerned by the discrete kinetic model applied directly to the TA spectrum.

Fourier analysis of oscillations

Oscillations in ΔA could be observed at early times upon close inspection of the data presented in Fig. 4.3(a) which could be an indicator of vibrational coherence. These were investigated through Fourier transform of the residuals obtained from the discrete kinetic analysis, which produced a spectrum indicating the oscillation frequency. This was compared the Fourier spectrum pertaining to TA data for neat solvent acquired under identical experimental conditions (i.e. same pump wavelength, polarisation and fluence), which is presented in Fig. 4.5. Both Fourier transform spectra were shown to possess a sharp peak at 495 cm^{-1}, with no other notable differences. Thus it can be concluded that the oscillations do not arise from coherences induced from $[Cr(CN)_6]^{3-}$ itself. As the intensity profile observed was not consistent with that shown within Raman spectra reported for liquid H_2O in literature [98], it can be assumed that the coherences instead arise from the quartz windows of the flow cuvette used in the experiment.

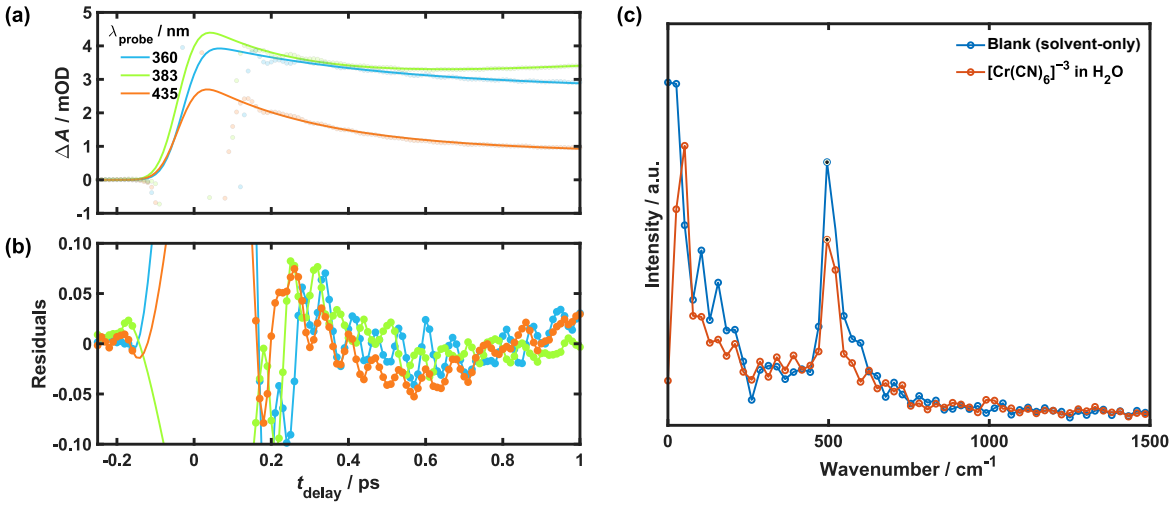

Fig. 4.5 Fourier analysis of oscillations observed in Fig. 4.3(a). (a) Kinetic traces obtained at early t_{delay} with their corresponding fits. (b) Residuals obtained from the kinetic fitting procedure. (c) Fourier transform spectra obtained for neat solvent and aqueous $[Cr(CN)_6]^{3-}$ measurements.

4.4.2 Ligand-field excitation at 325 nm

Experiments were performed that attempted to pump the second ligand-field transition ($^4T_1 \leftarrow {}^4A_2$) to investigate the effect of greater pump photon energy on the dynamics. These measurements used a pump wavelength of 325 nm and 1.3 mJ cm^{-2} fluence, which was the maximum achievable with the laser system. While the effect of varying laser power was not determined at this specific wavelength, the fluence is roughly half of what was used at 400 nm. Given the lower extinction coefficient at 325 nm ($\epsilon = 30$ M^{-1} cm^{-1}), it can be reasonably assumed that the experiment lies within the linear absorption regime, and that the dynamics correspond to single-photon processes.

Shown in Fig. 4.6 are TA data acquired for the two different pump wavelengths under identical acquisition conditions. To account for the disparity in the pump fluence and extinction coefficient between the two measurements, the TA data pertaining to 400 nm photoexcitation was multiplied by a constant factor ($\frac{F_1}{F_2} \times \frac{\epsilon_1}{\epsilon_2} = 0.38$).

The presence of ESA_1 at early time delays and the growth of ESA_2 on timescales >1 ps are consistent in the difference spectra across the two measurements. While no new features are observed upon photoexcitation at 325 nm, it is interesting to note that the initial width of ESA_1 is wider and the peak is apparently blueshifted with respect to measurements using a 400 nm pump. From the kinetic traces for bands centred at 360, 383 and 435 nm, is immediately obvious that the XPM is wider in the experiments using the 325 nm pump. This will arise from the use of additional optics to facilitate the use of this bluer wavelength, which will have the effect of temporally stretching the pulse and thus prolonging the presence of non-linear artefacts in the data. When considering only the time delays unaffected by XPM, the 360 and 383 nm traces appear to be largely parallel for the two excitation wavelengths. This is a coarse indication of similar kinetics. It is interesting to note that the early kinetics (<1 ps) observed at 435 nm is different for two pump wavelengths: the TA response appears to

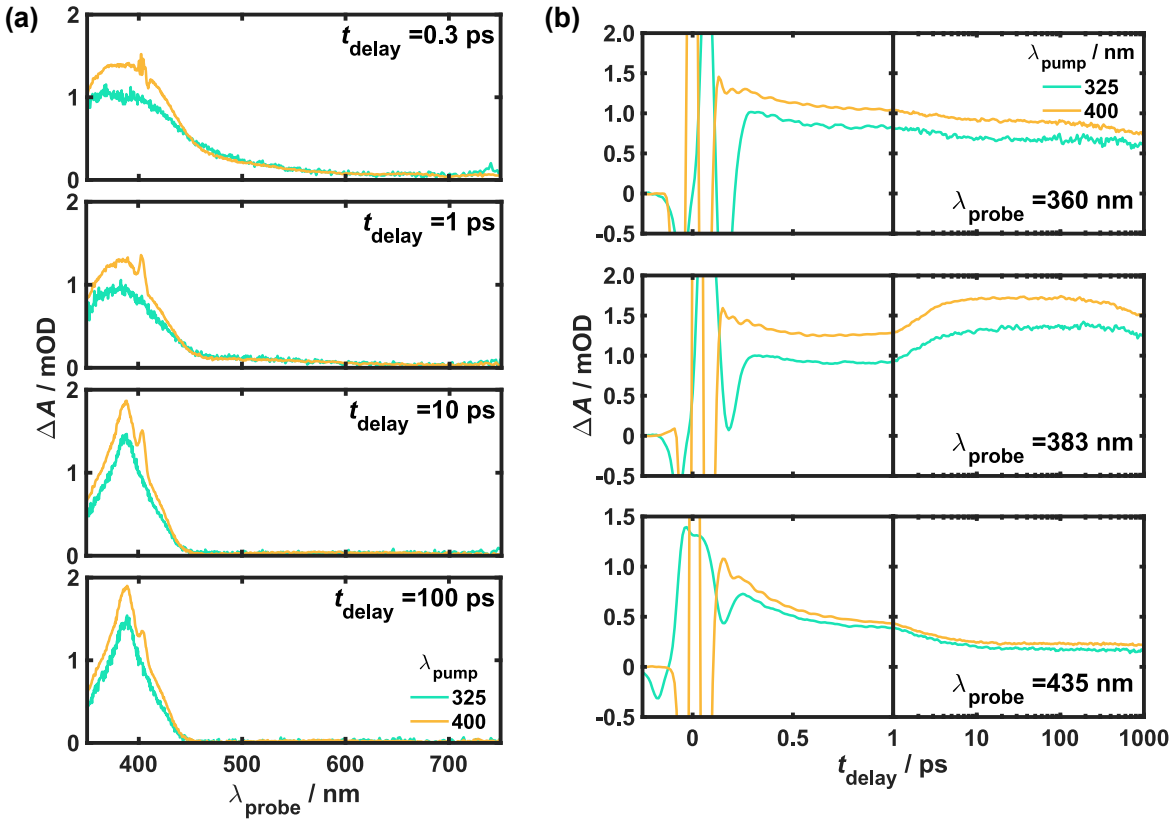

Fig. 4.6 Comparison of TA data acquired upon photoexcitation at 325 and 400 nm. (a) Difference spectra for the two excitation wavelengths (coloured lines) at different time delays. Note that the sharp feature spanning 400–410 nm in the spectra for 400 nm photoexcitation arises due to pump scatter. (b) Kinetic traces obtained for the different excitation wavelengths (coloured lines) at three different probe wavelengths corresponding to different regions of the ESA.

decay faster for 400 nm excitation than for 325 nm. This could indicate slower kinetics pertaining to ESA_1 shifting and narrowing at higher pump energies.

4.5 Interpretation of ultrafast dynamics

The findings of the TA experiments suggest the dynamics that ensue upon ligand-field excitation arise from the population of at least two states, given the presence of two independently evolving ESA bands. Firstly, parallels can be drawn between ESA_1 in $[Cr(CN)_6]^{3-}$ and the equivalent band in $Cr(acac)_3$: both appear within the time-resolution of their respective experiments, decay quickly to a plateau with no appreciable decay for prolonged timescales, and undergo both redshift and narrowing within ∼1 ps. However, the key distinction in the dynamics of $[Cr(CN)_6]^{3-}$ is the growth of ESA_2 in the middle of the first band with $\tau = 2.33$ ps, which only appears to decay on >5 ns timescales. This has no analogous feature in $Cr(acac)_3$.

Based solely on the electronic structure presented in Section 4.3, there are two likely origins for the ESA bands: ^{4}LMCT ← $^4T_2$ or ^{2}LMCT ← ^{2}E. However, the same discussion also raised the issue of photochemical activity: as photoaquation has been reported in the literature, it is possible that optical pumping of $[Cr(CN)_6]^{3-}$ may generate a heteroleptic complex, such as $[Cr(CN)_5(H_2O)]^{2-}$. The reported photochemical quantum yield for such processes is thought to be 10–15% [85, 91]. This would be compounded by the low flow rate in the measurements, as almost 30 opportunities would be presented for photosubstitution in the sample volume exposed to the pump beam before it is fully exchanged. Thus, it is also plausible that ESA may arise from said photoproducts. Electronic spectra for $[Cr(CN)_5(H_2O)]^{2-}$ in literature report ligand-field transitions for this complex are redshifted with respect to $[Cr(CN)_6]^{3-}$ and are observed at 428 and 334 nm, respectively [99]. Given the reasonably low photochemical quantum yield and lack of any observable GSB component to the TA

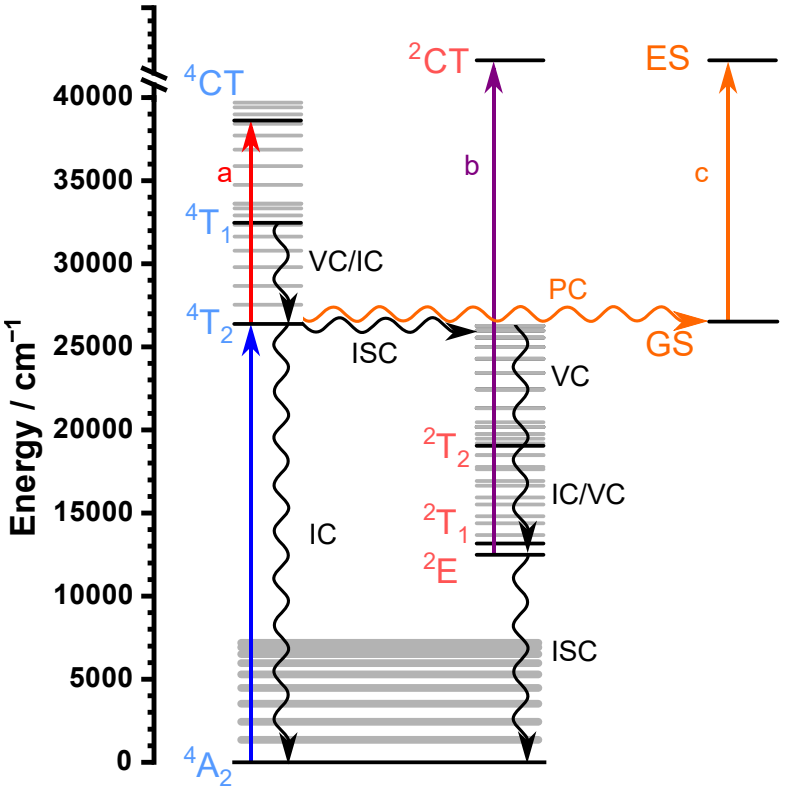

Fig. 4.7 Jablonski diagram illustrating the relevant electronic states/superimposed vibrational levels, likely ESA transitions and possible relaxation pathways for $[Cr(CN)_6]^{3-}$ upon photoexcitation of $^4T_2 \leftarrow {}^4A_2$ based on current understanding of its photophysics. Relaxation processes are abbreviated as follows: vibrational cooling (VC), intersystem crossing (ISC), internal conversion (IC), photochemistry (PC). The predicted LMCT transitions from the ligand-field excited state and the doublet manifold are labelled a and b, respectively, while c represents an excited state transition arising from a potential photoproduct.

from $[Cr(CN)_6]^{3-}$, it can be assumed that these additional absorption features will also have negligible contribution. Therefore, any ESA contribution due to these must arise from a transition with large ϵ, i.e. charge-transfer.

The relevant states for each of these three scenarios and the possible excitation/relaxation pathways are summarised in Fig. 4.7. To account for the two ESA bands observed, there are three hypotheses which consider the potential spectroscopic assignments. Each interpretation will be discussed in turn.

Hypothesis 1: Excited state absorption from doublet manifold and photoproducts

The simplest hypothesis is that the photoinduced dynamics in $[Cr(CN)_6]^{3-}$ are similar to those in $Cr(acac)_3$: ESA_1 arises from population of the doublet manifold (Fig. 4.7 b) through ISC on timescales faster than the experimental resolution and subsequently undergoes vibrational relaxation, in line with the findings of Juban and McCusker [40]. As these encompass the lowest-lying doublet states, the growth of ESA_2 would then arise from a photoproduct (Fig. 4.7 c).

The narrowing of the ESA_1 band is concomitant with some form of vibrational relaxation: progression to the bottom of the potential energy surface will confine Franck-Condon factors to a narrower range of nuclear coordinates, resulting in good vibrational wavefunction overlap with a reduced number of sublevels on the higher-lying excited state potential [40]. This process conformed to biexponential kinetics ($\tau_{fast} = 0.7$ and $\tau_{int} = 8$ ps), which could be an indication that a cascade of multiple vibrational relaxation pathways and possibly IC takes place, as would be expected given the energetic arrangement of the doublet states illustrated in Fig. 4.7. Also in line with $Cr(acac)_3$ is the long-lived nature of ESA_1, as might be expected of spin-flipped states.

However, issues with this interpretation arise when the second ESA band is considered. It is notable that the kinetics obtained through spectral decomposition analysis for the decay of ESA_1 ($\tau_{fast} = 0.260$ and $\tau_{int} = 5.8$ ps) and growth of ESA_2 ($\tau = 2.33$ ps) are not consistent, which would be expected of a simple conversion process. Furthermore, previous studies have demonstrated that it is the ligand-field state that is photochemically active in $[Cr(CN)_6]^{3-}$ rather than the doublet manifold [91], which would suggest that the $^4T_2$ state should still be populated at least on the timescales associated with the growth in ESA_2. Thus, if the second band did indeed arise from

photoproducts, it would be expected that a third ESA feature arising from this excited quartet state should be present. However, no such feature appears regardless of whether the lower or higher pump energy is used, even fleetingly (Fig. 4.6).

Hypothesis 2: Excited state absorption from quartet and doublet manifolds

The second hypothesis is that the two ESA bands are simply characteristic of the two spin manifolds: ESA_1, which is present within the time resolution of the experiment, arises from the $^4T_2$ state (Fig. 4.7 a) while ESA_2 arises from the doublet manifold (Fig. 4.7 b), which is populated at early times. In this scheme, the rate of ISC would be slower than that observed in $Cr(acac)_3$. This is perhaps not unexpected given the relatively low efficiency of ISC in $[Cr(CN)_6]^{3-}$ discussed in Section 4.3, although this interpretation is also flawed in that the kinetics for the decay/growth kinetics of the two bands are not consistent with a simple conversion process. It is also clear from the kinetics that the state responsible for ESA_2 is relatively long-lived as there is no appreciable decay for hundreds of ps. This would appear to be inconsistent with the outcome of the photoluminescence study also outlined in Section 4.3, which found that the doublet state is rapidly deactivated by the presence of H_2O.

Further doubt is cast on these assignments when the shape and position of the observed bands are considered: ESA_2 is completely overlapped by ESA_1 and possesses a much narrower width. This is inconsistent with Juban and McCusker's assertion that the widths of the excited state ^{4}LMCT and ^{2}LMCT transitions would be similar and that the latter should occur at higher energy [40].

Hypothesis 3: Excited state absorption from quartet manifold and photoproducts

The third hypothesis is that ESA_1 is indicative of the $^4T_2$ state population (Fig. 4.7 a) while ESA_2 arises from photoproducts (Fig. 4.7 c). In this scheme, ESA_1 may decay as it is depopulated through ISC, IC, or photochemical reaction, while ESA_2 grows as photoproducts are produced. The absence of a third feature from the doublet manifold would suggest that it is either optically silent or transitions from it occur outside of the detection window for the experiment. Like the aforementioned hypotheses, this interpretation is supported by the kinetics of ESA_2 but fails to account for either the energetics or kinetics of ESA_1.

4.6 Conclusion

Photoexcitation of ligand-field transitions $[Cr(CN)_6]^{3-}$ in aqueous solution gives rise to an ESA that comprises two features: a primary, broader band centred at 375 nm and a secondary, narrower band centred at 383 nm which overlaps with the first. Both are attributed to charge-transfer transitions arising from at least one excited state, although the specific states involved remain undetermined.

The evolution of the primary band is consistent with observations of Juban and McCusker in $Cr(acac)_3$: narrowing and a slight redshift is observed over a few ps, which had been attributed in their work to vibrational cooling. The appearance of the secondary band is completely new, and its origins remain unknown. Three interpretations have been proposed to explain the nature of the two bands, which assign them as spectroscopic signatures of the ^{4}LMCT state, the doublet manifold, or photoaquated Cr(III) cyanide complexes. All three schemes have their merits and drawbacks. However, what is clear is that the dynamics observed in $[Cr(CN)_6]^{3-}$ are

clearly not dominated by the doublet manifold as is the case in $Cr(acac)_3$ and thus care should be taken when using the dynamics observed in the latter system as a model for the interpretation of those observed in Cr(III)-based PBAs.

To definitively identify whether the secondary band arises from photochemical activity, it would be necessary to perform the same experiment again using $[Cr(CN)_6]^{3-}$ dissolved in a non-coordinating solvent; the absence of photosubstitution would cause the second band to disappear if it were a feature of photoproducts. As $K_3[Cr(CN)_6]$ is only soluble in H_2O or alcohol, an alternative salt, such as $[NBu_4]_3[Cr(CN)_6]$, would be required. Care would need to be taken to ensure that the combination of counterion and solvent would not shift the LMCT transitions into a region where they overlap with the ligand-field transitions used for optical pumping. In the same vein, it may also be expected for any ESA features to significantly shift as stability/instability is afforded to these states in different solvent environments.

Alternatively, direct excitation into the doublet manifold at 760 nm would serve to establish whether the primary band arises from the doublet state, as it still would be observed if this were the case. This would also avoid photochemical activity, which has been purported to only occur from interconfigurational states [91]. However, the low extinction coefficients associated with the spin-forbidden transitions ($\epsilon \leq 1$ M^{-1} cm^{-1}) would provide a considerable obstacle. While this could in principle be overcome with higher solution concentration, the sample would then become quite opaque to UV, which would be further compounded by ESA. The most feasible alternative would be to increase laser fluence; however, with that comes the risk of exciting multi-photon processes at excessively high fluences, as well as the introduction of oscillations/artefacts from the cuvette/solvent which would obscure the dynamics. Indeed, the latter issue was encountered when attempting to perform the same experiment using an 800 nm pump with a fluence of 8 mJ cm^{-2}.

Any issues arising from photochemical behaviour or rapid deactivation of the doublet state may also be overcome by performing ultrafast experiments on a solid sample containing $[Cr(CN)_6]^{3-}$, such as single crystals of $K_3[Cr(CN)_6]$ or having incorporated it into an alternative crystalline host, such as $K_3[Co(CN)_6]$. This latter approach has been shown to be successful in previously reported photoluminescence studies [100]. However, preparation of a sample in this form which is suitable for transmission-based TA measurements is practically challenging given the propensity of small, imperfect crystals to scatter light. While attempts were made to grind $K_3[Cr(CN)_6]$ into a fine powder and incorporate it into a mull using NOA 61, establishing the conditions required for a suitable sample were difficult: samples that were too concentrated were opaque to the probe beam due to light scatter, while dilute samples did not appear to show much absorbance at all. The optimisation of such a process is one possible avenue to explore.

Chapter 5

Electronic and magnetisation dynamics in Cr–Cr Prussian blue analogue

5.1 Project background

Currently at the forefront of ultrafast magnetism is non-thermal perturbation of long-range magnetic order using light. Section 1.2 summarised a few TR-MO studies in which this has been reported for crystalline dielectrics through photoinduced change in anisotropy [8, 9]. However, it is notable that there is a distinct lack of reports in the literature that have used all-optical pump–probe techniques to extend this treatment to molecular-based systems; to date, the work of Johansson *et al.* is the only example [41].

The study on mixed-valence V–Cr PBA investigated the dynamics associated with the optical pumping of a LMCT transition and concluded that population of localised doublet states on Cr(III) sites gave rise to the magnetisation dynamics that ensued [41]. One key question which arose from these findings was whether the same localised

spin-flips would also dominate the magnetisation dynamics of other Cr(III)-based PBAs possessing different A^{II} cations.

While a variety of other Cr(III)-based PBAs exist, mixed-valence Cr–Cr PBA is notable as — like V–Cr PBA — it also possesses a high T_c, which can range from 160–240 K depending on the stoichiometric ratio of Cr^{III}:Cr^{II}. This is convenient for MO measurements, as magnetic ordering can be readily achieved at liquid N_2 temperatures. Compared to V–Cr PBA, the electronic spectrum for Cr–Cr PBA is dramatically different; while the MM′CT transition in V–Cr PBA is particularly broad and extends across much of the visible region (500–900 nm), the same transition in Cr–Cr PBA is reported to occur in the UV (<400 nm). This could unmask additional ESA features in Cr–Cr PBA that may have previously been obscured by the strong GSB in V–Cr PBA.

Thus, this chapter reports investigations into the ultrafast dynamics of Cr–Cr PBA using a combination of TT and TR-MO measurements to relate changes in electronic state to magnetisation dynamics. Note that this is the expansion of a project first initiated by Dr. Luke Hedley (PhD, 2020) as part of his doctoral studies in the Johansson group. While the overarching themes are the same, the improvements in sample preparation reported in Chapter 3 and development of the experimental setup have greatly increased the quality of both spectral and magneto-optical data. The SQUID magnetometric data presented herein was acquired by the Johansson group's collaborator Dr. Oscar Céspedes at the University of Leeds. All spectroscopic and MO data and analyses presented are my own.

5.2 Physical properties of Cr–Cr Prussian blue analogue

The primary method of characterising the composition of Cr–Cr PBA thin films was through inspection of their electronic and vibrational spectra, which were outlined in Section 2.2. It is important to note that there was considerable variation in the spectral and magnetic properties of Cr–Cr PBA, even amongst films produced in the same batch and seemingly under the same conditions. This is due to the highly variable stoichiometry of this material, in which both Cr^{III} and Cr^{II} may be present in either A- or B-sites. Thus, it is necessary to consider the impact of oxidation on the films.

5.2.1 The effects of film oxidation

The work of Buschmann *et al.* extensively investigated the effects of oxidation state in Cr–Cr PBA films on many of their physical properties using techniques such as electronic and vibrational spectroscopy, magnetometry, scanning electron microscopy and X-ray diffraction [60]. While oxidation state in their investigations was systematically controlled through electrochemical means, Coronado *et al.* have reported that their films undergo air-oxidation within hours [49]. This was indicated by suppression of an IR band at 2066 cm^{-1} attributed to low-spin $B = Cr^{II}_{LS}$ moieties over time while the band at 2186 cm^{-1} attributed to $B = Cr^{III}$ grew in intensity, which was consistent with the electrochemical investigation by Buschmann and co-workers. Thus, IR measurements provide a quick and efficient means of determining the level of oxidation in these films.

It was notable that the macroscopic appearance of our films changed significantly in the time after synthesis: while they started out a murky brown colour, they became significantly paler within hours, and heavily aged films appeared white in colour. While a few electronic spectra for Cr–Cr PBA have been reported in literature [49, 54, 101]

and the original work by Mallah *et al.* stated that NIR absorption occurred exclusively when B = Cr^{II}_{LS} was present [19], only Buschmann *et al.* have determined any variation in the UV-visible region due to oxidation state [60]. They reported that absorbance of their electrochemically produced films actually increased upon oxidation, while the opposite trend appeared to be the case in our films. However, it is notable that absolutely none of their spectra are consistent with any others that have been reported for Cr–Cr PBA [49, 54, 101] nor our own [47], irrespective of oxidation state.

Given the importance of identifying film composition, the discrepancies in the electronic spectral trends observed for our films with respect to oxidation *vs.* those determined by Buschmann *et al.* warranted investigation. To this end, IR reflectance spectra were recorded for a freshly made film within 18 hours of synthesis, which had been stored in a glovebox under an inert (N_2) atmosphere overnight. These were compared against the spectrum recorded for a film exposed to air for over one year. Likewise, UV-visible-NIR transmittance was also recorded for a film shortly after synthesis and after several weeks' air exposure for comparison. These are presented in Fig. 5.1.

In accordance with the findings of Coronado and Buschmann, the second IR band at 2075 cm^{-1} is present in the spectrum for the freshly made film but completely absent in the aged one. The UV-visible-NIR transmittance spectra show an increased transmittance across the visible upon film ageing *vs.* when freshly made, consistent with our observations by eye. A starker difference is observed in the NIR, where there is considerably more transmission when the film is aged; this is consistent with the aforementioned NIR absorption band reported by Mallah *et al.* in their material containing B = Cr^{II}_{LS} [19]. Note that the transmittance upon encapsulation matches the typical absorption profile reported in literature [49, 54, 101].

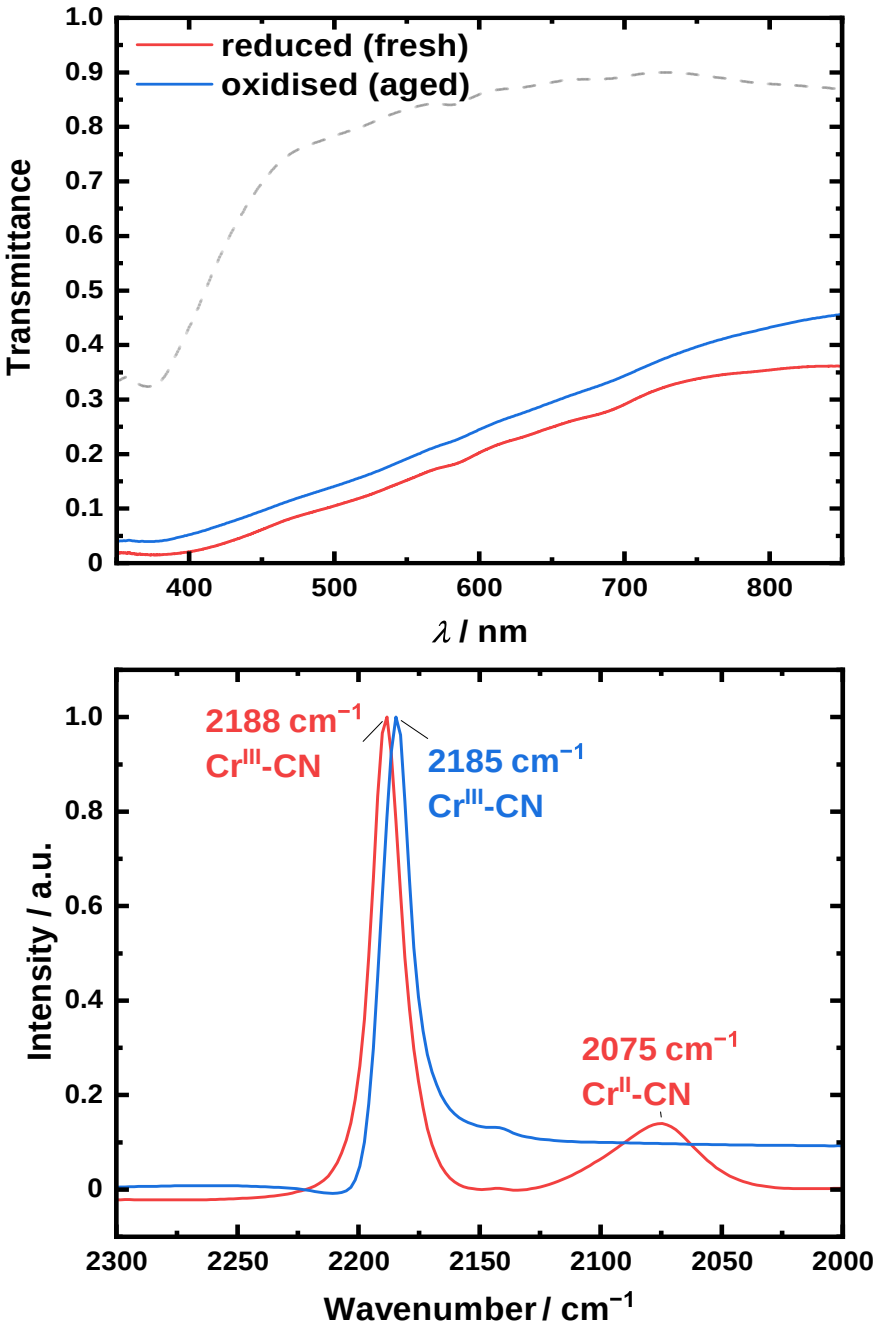

Fig. 5.1 Spectroscopic characterisation of Cr–Cr PBA films upon significant air exposure. Top panel: UV-visible-NIR transmittance spectra recorded for a single exposed film shortly after synthesis and again after ageing for several weeks. Overlaid is the transmittance for the same film sealed with NOA 61 upon ageing (dotted line). Bottom panel: IR reflectance spectra recorded for a freshly made film *vs.* a film exposed to air for several months. The legend used is the same as that shown in the top panel. Vibrational peaks and their assigned origins are labelled. Note that the change in IR baseline for the aged film is an artefact resulting from the unlevel substrate surface.

In addition to its effect on spectroscopic properties, the oxidation state of Cr in Cr–Cr PBA also heavily affects the magnetic properties. Mallah *et al.* determined that the inclusion of B = Cr^{II}_{LS} acted to suppress the magnetic ordering temperature in their powdered samples (T_c = 190 K) compared to a material where B-sites were exclusively populated by Cr^{III} (T_c = 240 K) [19]. This was attributed to the inefficiency of SEI pathways in providing magnetic order given the presence of only two unpaired t_{2g} electrons in Cr^{II}_{LS}. These findings are echoed in Buschmann's study on Cr–Cr thin films, which also found that coercivity increased with increasing B = Cr^{II}_{LS} content [60]. This was ascribed to "single-ion anisotropy" which arises from the d^4 electron configuration of Cr^{II}; both high-spin (^{5}E, $t_{2g}{}^3e_g{}^1$) and low-spin (^{3}T, $t_{2g}{}^4e_g{}^0$) states are configurationally-degenerate, which in each case will be removed through geometric distortion of the respective coordination spheres [60]. This deviation from octahedral geometry provides an easy-axis along which the localised moments on these sites will align, thus accounting for the increased external field required for magnetisation reversal.

Magnetometric data recorded for two of our films exhibiting spectral properties consistent with oxidation and reduction also show the behaviour reported by Buschmann *et al.*, as presented in Fig. 5.2. Magnetic hysteresis for the oxidised film, recorded using SQUID magnetometry, is narrow ($\mu_0 H_c$ = 3 mT) and magnetic-ordering temperature high (T_c = 235 K). Conversely, the hysteresis for the reduced film, recorded through Faraday ellipticity (FE) measurements outlined in Section 2.5.7, is wider ($\mu_0 H_c$ = 15 mT) and the estimated ordering temperature lower ($T_c \sim$ 160 K).

While high T_c in Cr–Cr PBA is obviously desirable for its procedural convenience, the suppression of electronic absorption bands results in reduced flexibility for the purposes of all-optical pump–probe experiments. Additionally, the presence of any magnetic anisotropy — as is the case with more B = Cr^{II}_{LS} content — opens the possibility of perturbing this property using light in order to optically manipulate

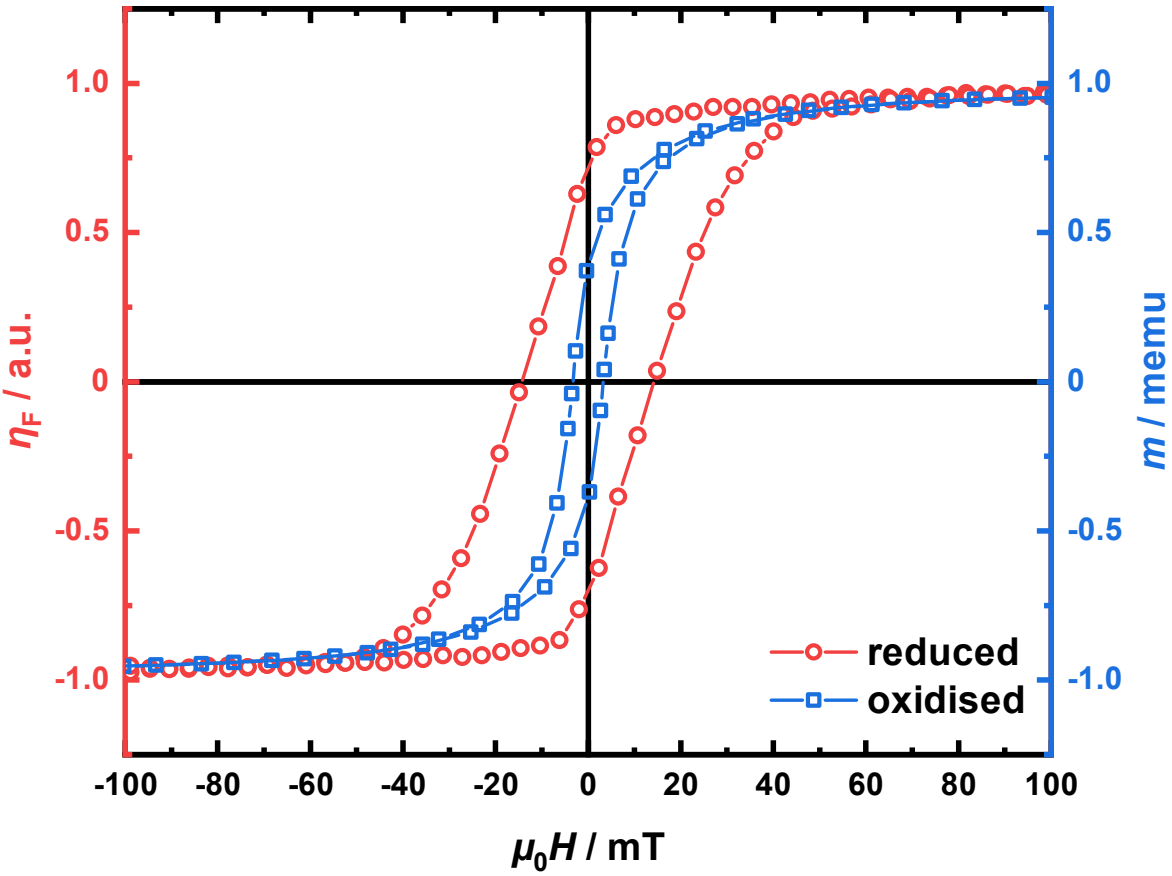

Fig. 5.2 Magnetic hysteresis loops recorded for oxidised and reduced films at 80 K. Data for the reduced film were obtained through FE measurements using a 400 nm beam originating from the OPA at a repetition rate of 20 kHz (red, left axis), while data for the oxidised film were obtained through SQUID magnetometry (blue, right axis).

the magnetisation, as reported by Hansteen *et al.* [8] in the work summarised in Section 1.2. Thus, more heavily reduced Cr–Cr PBA films were sought for TT and TR-MO experiments.

5.2.2 Steady-state spectroscopic assignments

Unlike many other PBAs, the electronic spectrum for Cr–Cr PBA lacks any distinctive features in the visible region. Typically, a single strong transition is observed at 380 nm while a series of smaller, presumably forbidden transitions occur at various other wavelengths across the visible. As discussed previously, the presence of B = Cr^{II}_{LS} content gives rise to an additional absorption feature in the NIR beyond 800 nm.

There appears to be a distinct lack of consensus in the literature with regard to spectroscopic assignments of Cr–Cr PBA, which likely arises from how the oxidation state of Cr enables various permutations of the material to exist. In the interest of settling this issue, it would be helpful to compare electronic spectra for Cr–Cr PBA films with different levels of oxidation to spectra obtained for independent Cr-based chromophores. This is demonstrated in Fig. 5.3. Note that because Cr^{II}-based complexes rapidly oxidise in air, it is difficult to disentangle their spectroscopic transitions from those pertaining to Cr^{III} [102]. Thus, the spectra for relevant Cr^{II} chromophores have not been recorded.

From electronic spectra for both reduced and oxidised Cr–Cr PBA, a significant absorption edge is observed towards the UV ($\lambda_{max} < 350$ nm) with large absorption coefficient, consistent with spectra reported by both Ohkoshi and Coronado [49, 54, 101] and density functional calculations by Rogers and Johansson [103]. Given the expectation that both A = Cr^{II}_{HS} and B = Cr^{III} should be present in each film, this can be attributed to MM′CT between the two.

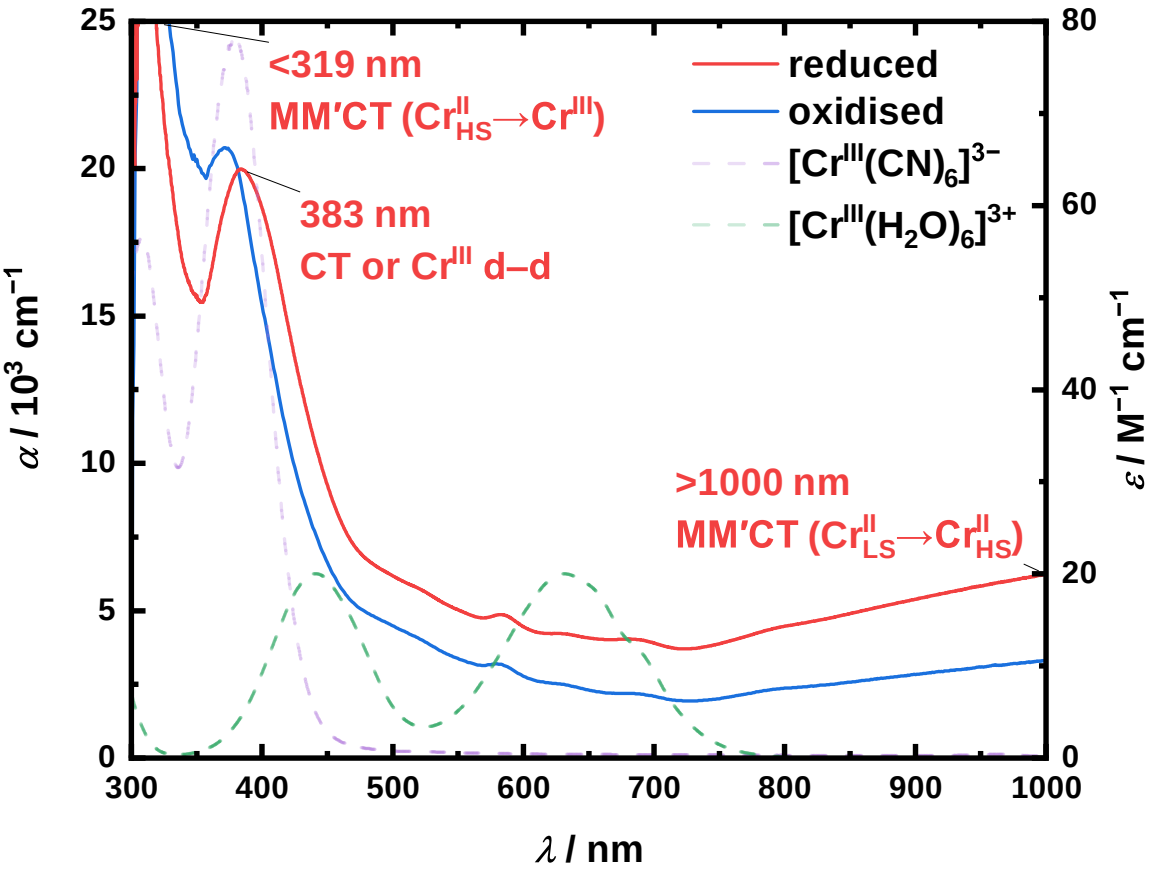

Fig. 5.3 Electronic spectra recorded for reduced and oxidised Cr–Cr PBA, where α has been calculated using film thickness (left axis). Peaks of note are labelled with their assigned transitions. Superimposed are electronic spectra for related Cr^{III} complexes with different ligand-field strengths for comparison (right axis).

It is interesting to note the presence of an intense peak at around 380 nm that appeared in most of our spectra for Cr–Cr PBA; this is sometimes a weak shoulder for more oxidised films, but is better defined in reduced films. This is clearly observed in Fig. 5.3. While attributed to MM′CT by Coronado *et al.*, this is somewhat inconsistent with the aforementioned density functional calculations which predicted that the first Cr^{II}–Cr^{III} MM′CT lies at 284 nm [103]. Instead, this peak appears to match the energy of the $^4T_2 \leftarrow {}^4A_2$ transition observed in $[Cr^{III}(CN)_6]^{3-}$, which forms the backbone of the PBA. At the opposite end of the spectrum lies a broad absorption band in the NIR ($\lambda_{max} > 1000$ nm), which is much more intense for the more reduced film. This is in agreement with the work of Mallah *et al.*, who had tentatively ascribed it to a second MM′CT between $B = Cr^{II}_{LS}$ and $A = Cr^{II}_{HS}$ [19]. Indeed, the observation of such features in the NIR is not uncommon for mixed-valence systems [104–106]. An alternative interpretation is provided by spectroscopic reflectance data reported for crystals of $K_4[Cr^{II}(CN)_6]$, which indicate that a broad NIR transition is observed for Cr^{II}_{LS} at a similar wavelength ($\lambda_{max} = 1100$ nm) [107]. Thus, it is plausible that the peaks observed at around 380 and >1000 nm in Cr–Cr PBA possess contributions from localised B-site Cr^{III} and $B = Cr^{II}_{LS}$ transitions, respectively.

The spectra for Cr–Cr PBA show a number of poorly resolved peaks between 500 and 750 nm that are much weaker than any of the already assigned transitions and appear to be consistent with similar features observed by Ohkoshi *et al.* [54, 101]. This matches the description of Mallah's $B = Cr^{III}$ material as possessing an electronic spectrum that is a simple superposition of the constituent ionic species [19]. As discussed in Section 1.6, three spin-allowed ligand-field transitions may be observed for Cr^{III}-containing species ($^4T_2, {}^4T_1, {}^4T_2 \leftarrow {}^4A_2$). Consultation of the d^4 Tanabe–Sugano diagram indicates that one spin-allowed ligand-field transition may be observed in high-spin Cr^{II}-containing species ($^5T_2 \leftarrow {}^5E$), while four closely lying transitions would

be observed for low-spin Cr^{II} ($^3E, ^3T_2, ^3A_1, ^3A_2 \leftarrow {}^3T_1$). If the effect of tetragonal distortion is also considered at the Cr^{II} sites, the number of possible ligand-field transitions increases even further. As $A = Cr^{II}_{HS}$, $B = Cr^{II}_{LS}$ and $B = Cr^{III}$ are expected to be present in the Cr–Cr PBA films presented, this may account for some of these peaks.

To support assignment of the spectroscopic transitions in Cr–Cr PBA, it is helpful to draw comparison to other systems which exhibit similar characteristics. The physical properties of many mixed-valence coordination compounds have been summarised in a review by Robin and Day, who noted consistent trends amongst distinct groups of materials [108]. Using these observations alongside theoretical predictions of electron delocalisation across sites of differing valencies, a system was devised which could broadly categorise mixed-valence compounds into one of four classes based on their spectra, magnetic properties and conductivity [108]. Under this scheme, the characterisation of Cr–Cr PBA is consistent with so-called "class II" materials which possess only slight delocalisation: different valencies are present in coordination environments of similar symmetry (octahedral Cr^{II} and Cr^{III}), the material is magnetically dilute and orders at low temperature ($T_c \sim 160$ K), and its electronic spectrum appears to conform to the superposition of those from its constituent ions with additional, more intense transitions between them (weak transitions which appear to coincide with Cr^{III}, alongside an MM′CT in the UV). This is consistent with the characterisation of Prussian blue itself, which is also considered a class II material [108]. Nevertheless, it is notable that the intensities of the peaks at 383 and >1000 nm and the breadth of the latter appear to far exceed those expected for localised ligand-field transitions and seem to be more in line with charge transfer.

While the aforementioned spectroscopic assignments are sensible upon consultation of existing literature, they could also be tested experimentally. This could be achieved

through temperature-dependent transmittance measurements, as ligand-field transitions would be expected to decrease in intensity at low temperature (i.e. greater transmittance observed at lower T) [84] due to their reliance on vibronic coupling to overcome the Laporte-selection rule. Conversely, charge-transfer transitions have been observed to increase in intensity at low temperature (i.e. lower transmittance observed at lower T) [84]. To this end, transmittance spectra for the reduced Cr–Cr PBA film were recorded for six temperatures between 296 and 80 K; these are provided in Fig. 5.4. Note that the spectra presented were obtained using supercontinuum generated in CaF_2 as a light source, previously described in Section 2.5.4. To counteract the effects of film inhomogeneity which may manifest in the spectra due to the heavily focussed (∼50 µm-wide) beam, a reference spot was marked on the film and used consistently for all steady-state spectroscopic characterisation conducted using the optical setup.

Transmittance of Cr–Cr PBA is largely shown to decrease monotonically with decreasing temperature, concomitant with increased absorption. The effect is clearer at <550 nm, where absorption bands become better defined and slightly redshift at lower temperatures. This would appear to be inconsistent with the peak at 383 nm corresponding to a ligand-field transition and more in line with charge-transfer. However, as said peak overlaps with the red edge of the MM′CT transition, the apparent decrease in transmittance may instead result from greater sensitivity of this latter component to temperature. Similarly, the lower transmittance observed towards 750 nm upon cooling to 80 K would indicate that the NIR transition is likewise more consistent with charge-transfer than ligand-field. However, as transmittance data from this region of the spectrum does not appear to conform to a uniform trend between 200 and 80 K, conclusions drawn from these observations should be treated with caution.

Interestingly, a redshift and increased gradient in the absorption edge (<500 nm) was observed at low temperatures, with the greatest change occurring between 160 and

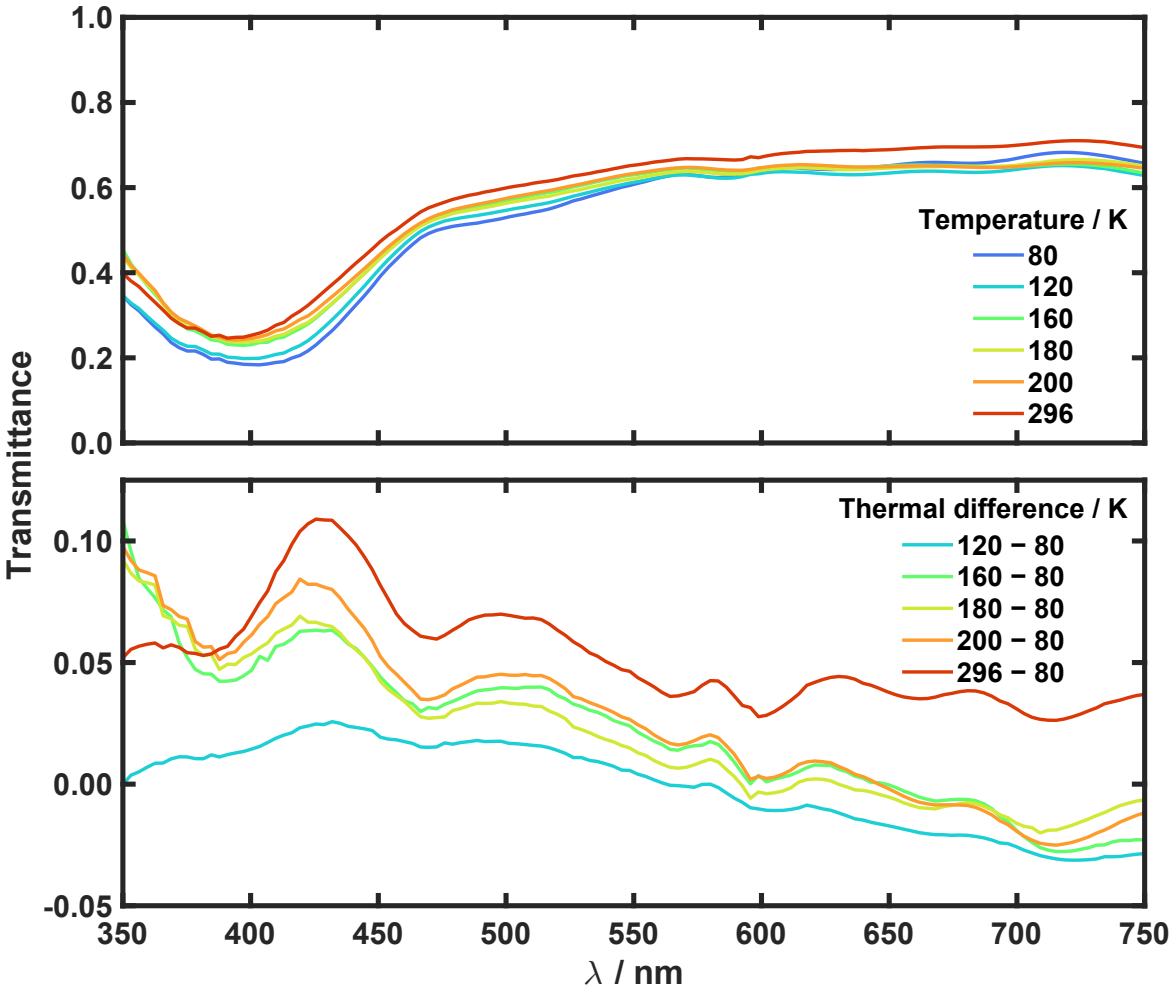

Fig. 5.4 Temperature-dependent electronic spectra recorded for the reduced Cr–Cr PBA film using white-light supercontinuum as a light source. Top panel: UV-visible-NIR transmittance spectra recorded at six temperatures between 80 and 296 K. Bottom panel: Thermal difference spectra calculated to emulate temperature-induced changes observed upon heating the film from 80 K.

120 K. This seemed to coincide with the T_c for this film, which had been estimated through the onset of coercivity in hysteresis loops recorded at various temperatures. Inspection of the thermal difference spectra calculated for the material reveals markedly different shape for the transmittance profiles corresponding to heating the film to room temperature ($296 - 80$ K) *vs.* heating the film to just above the T_c ($200 - 80$ K).

In the context of all-optical pump–probe studies, it is clear that there are multiple transitions which could be photoexcited to induce some change in magnetic order. The MM′CT bands in the UV and NIR, and the as-yet unassigned transition at 383 nm are ideal candidates as their different origins would, in principle, give rise to different dynamical behaviour. However, the adhesive used to encapsulate the films absorbs heavily in the UV ($\lambda_{max} = 365$ nm), which precludes the use of shorter wavelengths for optical pumping. Thus, only pump energies which are resonant with the blue-edge of the NIR MM′CT and the red-edge of the transition at 383 nm are practically viable for the pump–probe measurements.

5.2.3 Faraday spectra at low temperature

As the techniques to determine the magnetisation dynamics in Cr–Cr PBA are magneto-optical in origin, it is important to consider the steady-state MO properties of the material. While Faraday spectra have been reported for thin films of ternary PBAs containing A = $Cr^{II}_{HS}, Fe^{II}_{HS}$ and B = Cr^{III} [101], it would seem that no spectrum pertaining to exclusively Cr–Cr PBA has appeared in the literature to date. Therefore, it was pertinent to record the Faraday spectra — MORD and MCD — for the reduced film, which could be used to explain the bandshape of any signals observed in the TR-MO.

MORD and MCD spectra were recorded to probe both the magnetically saturated (field applied during acquisition) and remanence-only (zero applied field) response of the

reduced film at 80 K, which are shown in Fig. 5.5. The procedure for recording Faraday spectra conformed to the differential transmission/absorption methods described in Section 2.3.2 and used the multi-channel detection scheme described in Section 2.5.6. Note that these spectra were also obtained using supercontinuum generated in CaF_2 as a light source. As the spectra were produced through the measurement of very small differences in transmittance upon application of equivalent magnetic fields in opposite directions, they were heavily susceptible to fluctuations in the white-light intensity: a single outlier spectrum could completely skew the result. To mitigate this, many pairs of acquisitions (up to 30) were recorded and the Faraday spectrum calculated from each. The resultant array of Faraday spectra was then subject to a median filter which discarded spectra that lay outwith a set threshold (80th percentile) before averaging the remainder. Equivalent measurements were performed for both the encapsulated film and a control spot comprising bare substrate, adhesive and coverslip; the difference between the two was then calculated to yield the film-only response.

In the MCD spectrum, a small positive peak is observed at 385 nm while a large negative peak is observed at 433 nm. The latter appears to coincide with the onset of absorption at 470 nm in the electronic spectrum, which suggests that it arises from the corresponding spectroscopic transition. A broad, negative signal spans much of the red-end of the spectrum (>470 nm), which has been observed upon repeated measurements. This feature grows in intensity at shorter wavelengths, which is consistent with the absorption shoulder observed between 475–570 nm. When considering the effect of applied field, it is apparent the shape of the spectrum is maintained at zero-field and thus must arise from the remanence of the material. Upon applying a field to saturate the film, the strength of the MCD response is enhanced; however, there is insufficient consistency across different measurements to ascertain whether this is restricted to specific regions of the spectrum.

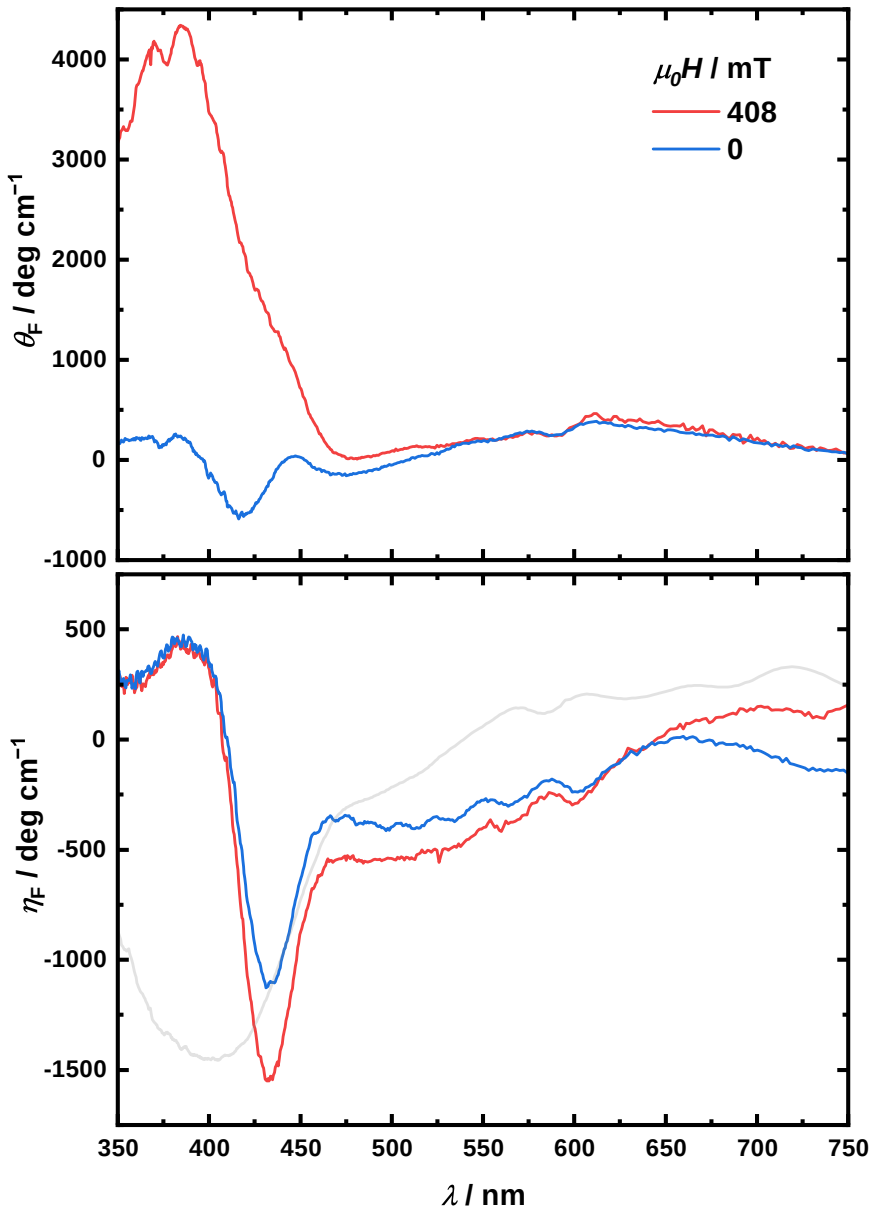

Fig. 5.5 Faraday spectra recorded for the reduced Cr–Cr PBA film at 80 K with different applied fields. Top panel shows MORD; bottom panel shows MCD, with transmittance overlaid in grey. For $\mu_0 H = 0$ mT measurements, a 408 mT field is briefly applied before each acquisition to align the magnetisation of the film, but no field is applied during data collection.

It is interesting to note that the two peaks in the UV collectively form a derivative shape, which is consistent with transition to an excited state with degeneracy removed by the magnetic field (associated with the so-called Faraday "$\mathcal{A}$-term"). That the two peaks possess different intensity may be a result of overlapping features from other Faraday terms, which arise from the mixing of different excited states in the presence of magnetic field (Faraday "$\mathcal{B}$-term") or removal of ground-state degeneracy by magnetic field (Faraday "$\mathcal{C}$-term", with its origin illustrated in Fig. 2.7 of Section 2.3.2). However, to decisively assign any features in a spectrum expected to possess components arising from a multitude of electronic states with different spins is non-trivial, and at the very least would require a comprehensive account of electronic structure, including characterisation of excited states, and reliable temperature-dependent MO data.

In the MORD observed for the film, it is clear that magnetic saturation introduces a large peak at 350 nm which eclipses the rest of the spectrum and has no analogue in the spectrum measured from remanence-only. While completely unexpected, it was reproducible on different occasions. As Faraday rotation may be observed even in diamagnetic materials with applied magnetic field, it is possible that this is an artefact introduced by the substrate or NOA 61/coverslip and has not been adequately accounted for in background subtraction. If the remanence-only spectrum is considered, which should not possess any contribution from the substrate due to zero applied field, the spectrum possesses a dispersive shape in the UV with an inflection point at around 431 nm, which matches the greatest MCD peak. This behaviour is typical of MORD spectra, and has been observed in studies of V–Cr and ternary Fe/Cr–Cr PBA films [43, 101].

5.3 Ultrafast transient absorption

Broadband TT/TR-MCD measurements were performed on the reduced Cr–Cr PBA film to investigate the dynamics that occur upon photoexcitation of the MM′CT in the NIR. The specific procedural details are outlined as follows.

The experiments employed the multi-channel detection scheme outlined in Section 2.5.6 at 1 kHz repetition rate. The pump wavelength was chosen to be 800 nm, as this could be blocked after the sample using an available dichroic mirror that was transparent in the UV. The probe polarisation was set to circular to enable the measurement of TR-MCD, as previously described in Section 2.3.2.

Before measurements commenced in earnest, the resilience of the Cr–Cr PBA sample to photodegradation by the pump was tested by measuring the TT signal, S, at a single wavelength for a prolonged period under similar experimental conditions as would be expected for a broadband TT measurement. The data acquired are provided in Fig. 5.6, which show <5% loss in TT response with respect to the initially observed signal, S_0, upon optical pumping for 30 minutes. As this far exceeded the time taken for a typical TR-MCD scan to be acquired for a single position on the sample, the sample was deemed to exhibit enough photostability to make the measurements viable.

For the measurements proper, the Cr–Cr PBA film was housed in an optical cryostat under vacuum and held at constant temperature. TT measurements were performed pairwise: each spectrum was recorded with applied field in either the positive or negative direction, and the sequence of these fields was reversed for each pair (i.e. $+H$ then $-H$ for pair one, $-H$ then $+H$ for pair two, *etc.*). For each pair of scans, the film was translated to a new position with a transmittance which matched that of the marked reference point. This was to mitigate any thermal or photodegradation effects that could incorrectly manifest as a TR-MCD signal while also minimising the impact of sample inhomogeneity.

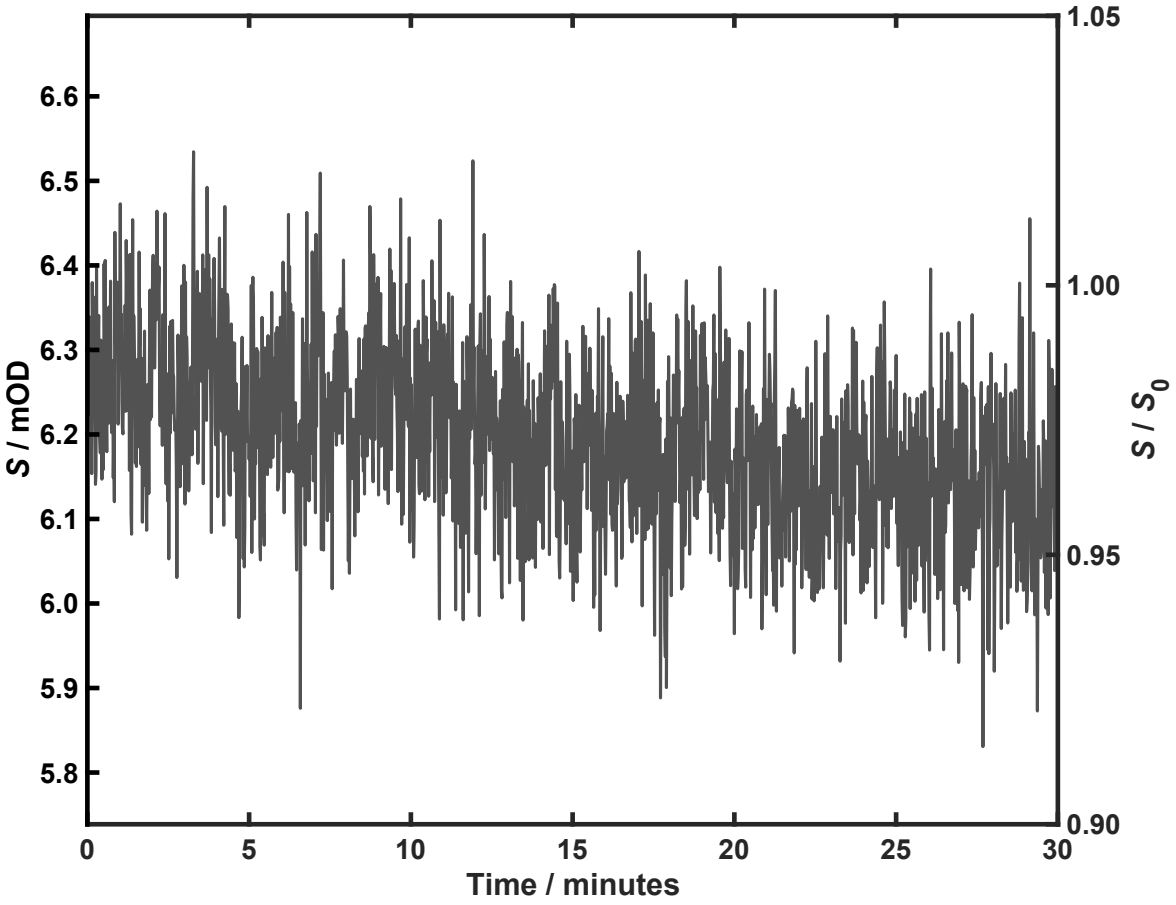

Fig. 5.6 TT response observed in 420 nm probe at fixed time delay upon prolonged photoexcitation of Cr–Cr PBA with an 800 nm pump of linear polarisation and fluence 4.2 mJ cm^{-2} at 296 K. Data were acquired every second with a 500 Hz repetition rate for the pump.

Once data had been collected, all scans for a given applied field direction were collated and subject to both time-zero and chirp correction before being averaged to yield the specific response for that particular field. The overall TT spectrum was calculated from averaging the spectra for the two opposite field directions and is reported in terms of percent transmittance change, $\Delta T/T$. Consequently, spectral features corresponding to GSB and ESA are inverted with respect to TA spectra reported in Chapter 4 — i.e. $\Delta T/T > 0$ represents GSB and $\Delta T/T < 0$ represents ESA (see Section 2.4.1).

5.3.1 Room-temperature measurements

As the primary carrier of magnetic moment in the material, it is first important to observe the electronic behaviour of the Cr–Cr PBA film in response to photoexcitation since evolution of the electronic structure will greatly influence the magnetisation dynamics. The first step of this was to determine the TT response of the film at ambient conditions, where it is magnetically disordered. Thus, the full TT spectrum was recorded for a pump fluence of 4.2 mJ cm^{-2} and linear (vertical) polarisation at room temperature (296 K), which is shown in Fig. 5.7.

A broad, largely symmetric ESA feature is observed across the visible, with a dip in intensity at 585 nm coinciding with ground-state absorption. A weaker ESA is also observed at bluer wavelengths ($\lambda_{max} = 470$ nm at 0.3 ps) which appears to be distinct from the much broader band. Both of these are shown to undergo monotonic decay within 10 ps, after which little change in intensity is observed. A strong GSB peak is observed in the UV ($\lambda_{max} = 398$ nm at 0.3 ps) which is shown to rapidly decay to a minimum within 10 ps, undergoes growth on 100 ps timescales, then decays once again on protracted timescales (>1 ns). It is notable that the GSB also appears to undergo a redshift at early time delays ($\lambda_{max} = 407$ nm at 10 ps). This, combined with both

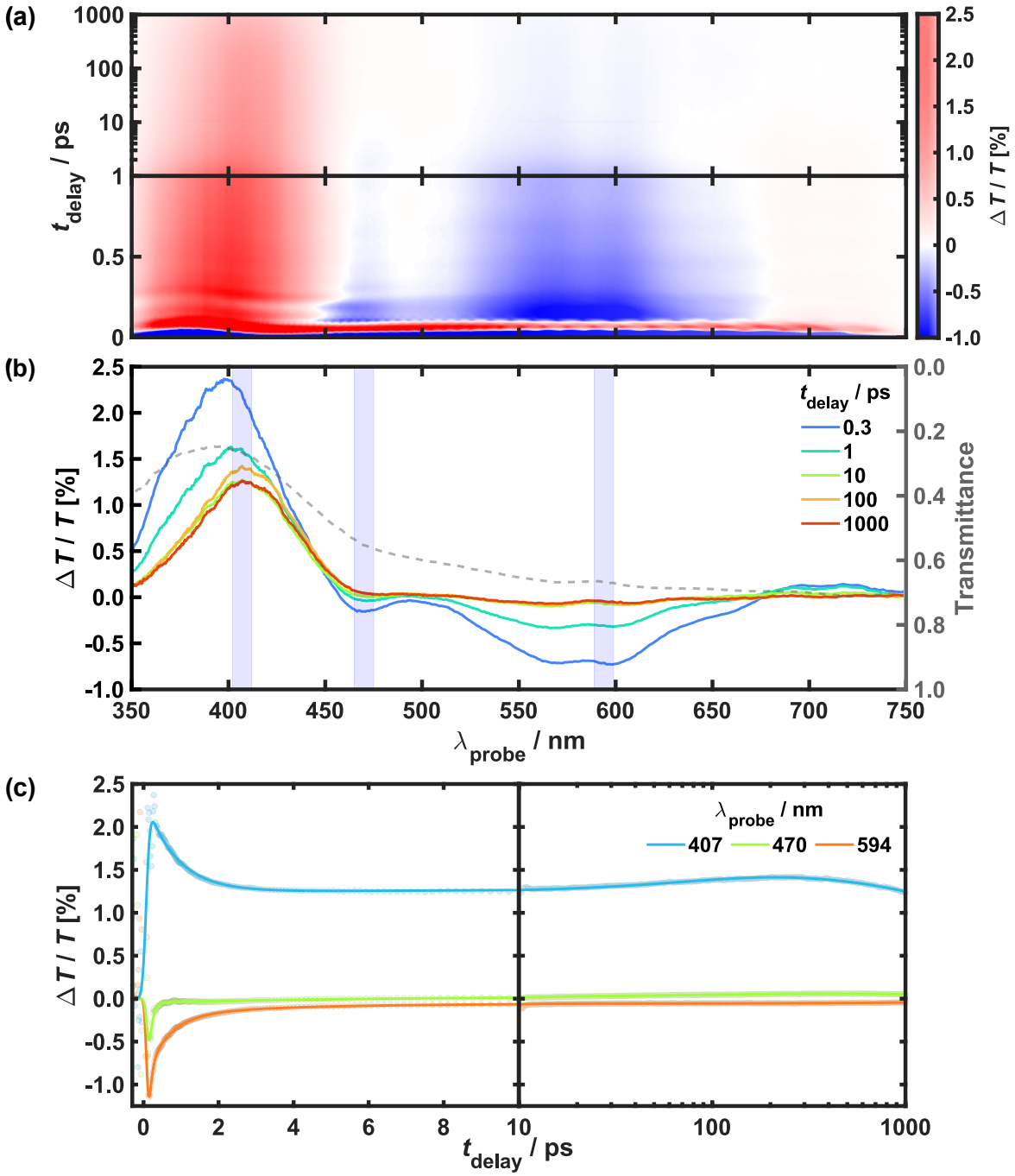

Fig. 5.7 (a) TT spectrum obtained for Cr–Cr PBA upon photoexcitation with an 800 nm pump of linear polarisation and fluence 4.2 mJ cm^{-2} at 296 K. Note that the intense bands observed across the whole spectrum at $t_{\mathrm{delay}} = 0$ ps arise from non-linear artefacts. (b) Difference spectra obtained at discrete time delays (coloured, left axis). Overlaid is the steady-state transmittance spectrum recorded at the same temperature for reference (dotted, right axis). Wavelength bands of interest for kinetic analysis are highlighted in blue; these regions were averaged and used to construct kinetic traces. (c) Raw kinetic data (hollow circles) for selected wavelength bands and corresponding fits (solid lines).

the apparent growth in intensity and the narrow width of the peak compared to the static transmittance spectrum, indicates the presence of at least one overlapping ESA component.

The kinetic traces for the three highlighted bands were subject to fitting using the same multiexponential decay scheme described in Section 4.4.1. The IRF was once again determined from a blank measurement, which in this case involved translation of the sample to an area not covered by the film to capture the background response (i.e. from coverslip, adhesive and substrate only). For an 800 nm pump, w was determined to range between 50 and 80 fs, which were the bounds used for w in the kinetic model. To remove the influence of XPM, which was particularly wide for this pump wavelength, all $\Delta T/T$ values corresponding to $-0.5 < t_{\text{delay}} < 0.13$ ps were omitted from the fitting. Time zero, t_0, was constrained between -0.1 and 0.1 ps, as before.

The fitted kinetic data are presented in Fig. 5.7(c), while the fit parameters obtained are summarised in Table 5.1. The band centred at 407 nm (primarily GSB) conformed well to tri-exponential kinetics, although the bands at 470 and 584 nm (ESA overlapped with GSB) required four exponential components to better represent the kinetics at all timescales. For each of the fitted bands, $R^2 > 0.97$, suggesting that — statistically — the exponential-based model provides a good description of the kinetics over the time interval sampled.

The kinetics for the three traces appear to conform to five characteristic timescales. The slowest component ($\tau_5 > 1500$ ps) is common to all three bands and corresponds to decay towards $\Delta T/T = 0$. This can likely be attributed to ground-state recovery; the larger uncertainty in these values indicates that the time delays accessible in the measurement are insufficient to capture this process, and thus it can be concluded that full ground state recovery takes several ns.

Table 5.1 Fit parameters obtained from kinetic analysis of the TT data presented in Fig. 5.7(c). Time constants possessing similar values across different wavelengths and their corresponding amplitudes have been assigned the same label.

λ_{probe} / nm	Amplitude		Time constant / ps	
407	A_2	0.52(1)	τ_2	0.82(3)
	A_4	−0.125(8)	τ_4	90(10)
	A_5	0.745(8)	τ_5	5600(400)
470	A_1	−0.6(1)	τ_1	0.077(6)
	A_3	−0.035(2)	τ_3	6.3(7)
	A_4	−0.021(2)	τ_4	120(30)
	A_5	0.033(2)	τ_5	4000(1000)
594	A_1	−0.6(1)	τ_1	0.067(6)
	A_2	−0.334(8)	τ_2	0.60(2)
	A_3	−0.070(4)	τ_3	3.5(2)
	A_5	−0.0285(3)	τ_5	4000(400)

Both the 470 and 594 nm bands undergo a very rapid decay on timescales similar to that of the IRF ($\tau_1 = 0.077$ and 0.067 ps, respectively) and consistent within each other's error bounds. This could indicate that both bands are distinct ESA contributions from a single state (tentatively MM′CT) initially accessed upon photoexcitation, which is depopulated through some relaxation pathway on these timescales. A second decay component on the order of a few ps ($\tau_3 = 6.3$ and 3.5 ps) is also present in both; this timescale is consistent with vibrational relaxation processes, which is supported by the much lower decay amplitude than that seen for the more rapid process (5–10%). As the two bands appear to be energetically distinct and have very different widths, these likely arise from transitions to different higher-lying states which possess potential energy surfaces with different curvature. It can thus be assumed that the Franck-Condon factors for the two transitions will evolve differently over time, which may account for the 3 ps discrepancy in the time constants.

The 407 and 594 nm bands exhibit two sub-ps decays (τ_2 = 0.82 and 0.60 ps). These corresponding to GSB and ESA, respectively, and having similar magnitude could indicate a fast pathway for ground-state recovery. However, as the both bands do not fully decay on these timescales and instead still persist at protracted time delays, such a relaxation process might be expected to have an efficiency far less than unity. This is consistent with a trap state with a potential barrier to deactivation. Alternatively, the apparent decay of the GSB could instead arise from the growth of an overlapping ESA component; that this would grow on a similar timescale to the decay of the 594 nm band would indicate transfer of population from the initially accessed state to a second excited state from which a more energetic ESA can be observed.

It is interesting to note that the 407 and 470 nm bands each possess a slower component (τ_4 = 90 and 120 ps) that are consistent within their error bounds and correspond to an increase in $\Delta T/T$. This results in an apparent "growth" of the 407 nm band and the 470 nm band crossing $\Delta T/T = 0$. The most plausible explanation is this is the result of a decay in an ESA component which overlaps significantly with the red side of the GSB, which is consistent with the apparent redshift in the peak as discussed above.

Decomposition analysis may be used to disentangle the kinetics associated with the overlapping spectral components, as reported for $[Cr(CN)_6]^{3-}$ in Chapter 4. However, this procedure must be exercised with caution when it comes to TT study of solid materials: other ultrafast studies on semiconductor thin films have revealed that significant thermal contributions to the TT response can manifest as ESA and can dominate the spectrum [67, 68, 109]. Thus, any attempt to fit the difference spectra must first account for these. While thermal difference spectra were recorded for this film (Fig. 5.4), the range of temperatures did not include any above that at which

these TT measurements were conducted. For this reason, spectral decomposition has not been performed for this dataset.

5.3.2 Low-temperature measurements

To follow up the investigation of electronic dynamics in Cr–Cr PBA at room temperature, the TT response was subsequently measured at low temperature when the film was magnetically ordered. Thus, the full TT spectrum was recorded for an 800 nm pump with a fluence of 4.2 mJ cm^{-2} and linear (vertical) polarisation at 80 K, which is shown in Fig. 5.8.

Cooling of the sample to 80 K produced marked changes in the TT response; GSB is observed to quadruple, and the balance of GSB/ESA contributions is shifted such that the former dominates the blue end of the spectrum (350–550 nm), while the latter dominates the red (550–750 nm). From the difference spectra (Fig. 5.8(b)), finer details can be more clearly discerned. The largest GSB signal observed ($\lambda_{max} = 422$ nm) is much less symmetric than at room temperature; there is a drop-off towards the blue that is not consistent with the overlaid static transmittance spectrum, which suggests overlap with at least one ESA component, as before. The shift in peak intensity towards the red and its increased sharpness suggest the overlapping ESA contributions have appreciably shifted upon cooling the film to 80 K. It is also notable that there is no longer an apparent redshift in peak wavelength with respect to time delay, indicating that the overlapping ESA contributions do not shift in energy over time at low temperature. The weaker ESA band observed in the blue at 296 K ($\lambda_{max} = 470$ nm) manifests as a trough in the band dominated by GSB (i.e. ESA < GSB) at 80 K, which splits the bleach band and results in the formation of a second peak centred at around 500 nm. TT response at both 422 and 470 nm appear to decay with similar kinetics: a

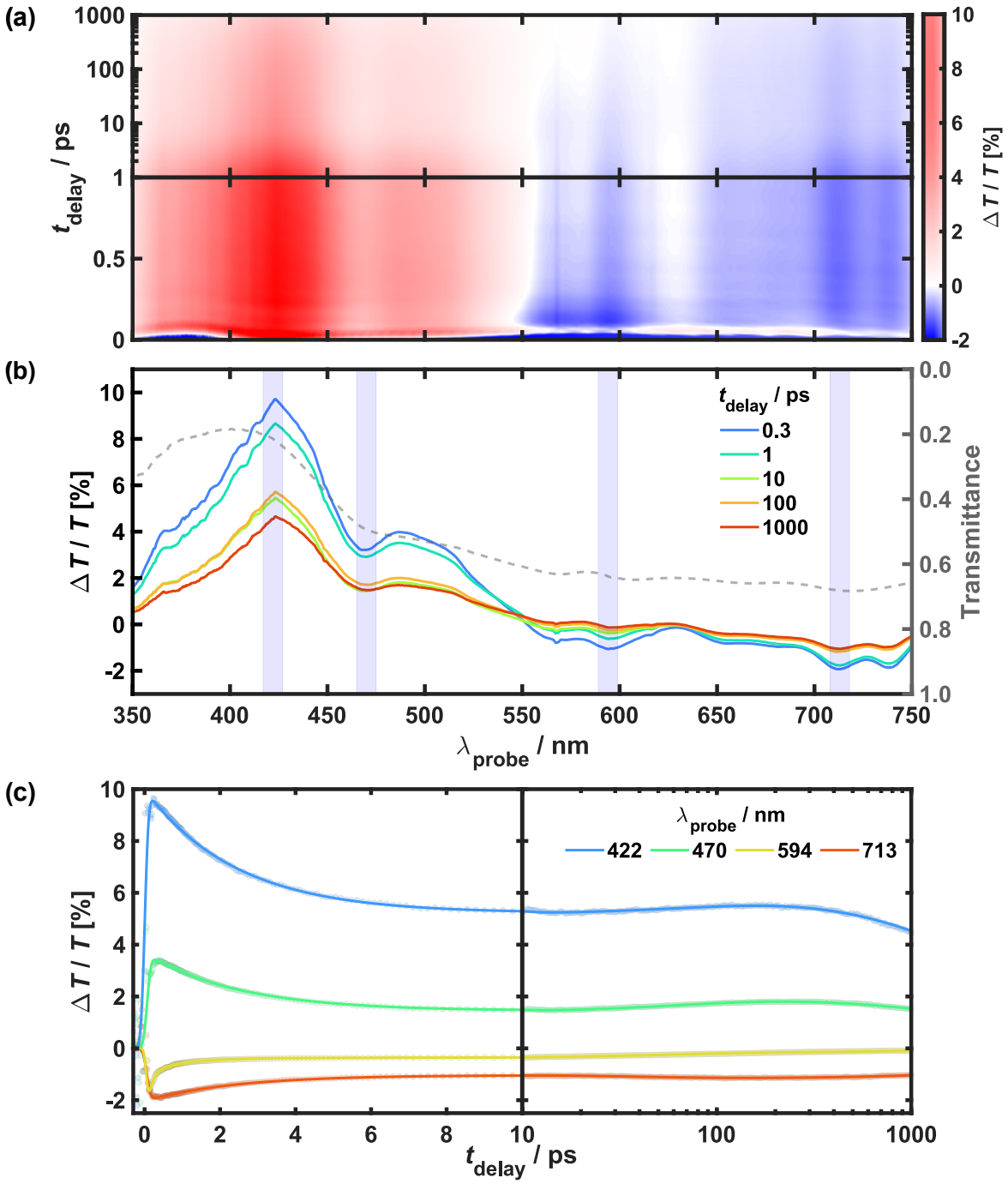

Fig. 5.8 (a) TT spectrum obtained for Cr–Cr PBA upon photoexcitation with an 800 nm pump of linear polarisation and fluence 4.2 mJ cm^{-2} at 80 K. (b) Difference spectra obtained at discrete time delays (coloured, left axis). Overlaid is the steady-state transmittance spectrum recorded at the same temperature for reference (dotted, right axis). Wavelength bands of interest for kinetic analysis are highlighted in blue; these regions were averaged and used to construct kinetic traces. (c) Raw kinetic data (hollow circles) for selected wavelength bands and corresponding fits (solid lines).

monotonic decay in intensity is observed until 10 ps, followed by growth within 200 ps, then subsequent decay on ns timescales.

The broad ESA feature observed in the middle of the visible region ($\lambda_{max} = 594$ nm) appears to possess similar intensity at both temperatures, despite the significant increase in GSB at 80 K. The width of this feature is significantly narrower at the lower temperature, likely a result of increased overlapping GSB contributions at the extremes of the band that act to reduce the intensity observed at the edges. The kinetics associated with this band are unique and are observed to decay monotonically with no apparent growth in intensity at any stage.

An additional ESA feature in the red comprising two peaks ($\lambda_{max} = 713$ and 738 nm, respectively) appears only at 80 K; this region was instead occupied only by a weak GSB contribution at 296 K. The kinetics for this band appear to reflect that of the GSB and exhibit at least two decays and a growth on similar timescales.

Discrete kinetic analysis

The kinetic traces for the four highlighted bands were subject to fitting using a multiexponential model, as before. The fitted kinetic data are presented in Fig. 5.8(c), while fitted parameters are summarised in Table 5.2. As was the case at room temperature, four exponential terms were required to fit the 594 nm band; the other bands were sufficiently described using only three components. For each of the fitted traces, $R^2 > 0.995$, again indicating the model presented a good representation of the data.

The kinetics for each of the traces conformed to five characteristic timescales, as was the case at room temperature. The slowest component ($\tau_5 > 1500$ ps) is common to all bands and once more is attributed to ground-state recovery.

Table 5.2 Fit parameters obtained from kinetic analysis of the TT data presented in Fig. 5.8(c). Time constants possessing similar values across different wavelengths and their corresponding amplitudes have been assigned the same label.

λ_{probe} / nm	Amplitude		Time constant / ps	
422	A_3	2.42(1)	τ_3	2.43(3)
	A_4	−0.37(1)	τ_4	98(8)
	A_5	3.00(1)	τ_5	3810(90)
470	A_3	1.114(7)	τ_3	2.58(4)
	A_4	−0.278(7)	τ_4	75(5)
	A_5	0.965(7)	τ_5	4300(200)
594	A_1	−0.78(1)	τ_1	0.114(4)
	A_2	−0.308(7)	τ_2	0.85(2)
	A_4	−0.103(2)	τ_4	54(2)
	A_5	−0.089(2)	τ_5	1460(70)
713	A_3	−0.503(3)	τ_3	2.49(4)
	A_4	0.083(3)	τ_4	43(3)
	A_5	−0.583(2)	τ_5	8600(300)

The 594 nm band undergoes rapid decay with two time constants ($\tau_1 = 0.114$ and $\tau_2 = 0.85$ ps) which are not observed in the kinetics for any of the other fitted bands at this temperature. This suggests that the origin of this feature is unique within the TT spectrum. That the band does not decay to zero until protracted time delays is again consistent with the previous suggestion that it arises due to an ESA from an initially accessed state with long lifetime. It is notable that both time constants have increased at lower temperature (*cf.* $\tau_1 = 0.067$ and $\tau_2 = 0.60$ ps at 296 K), which suggests that the rapid relaxation pathways are thermally activated.

The third time constant is observed in the evolution of the 422, 470 and 713 nm bands ($\tau_3 = 2.43$, 2.58 and 2.49 ps, respectively) and is associated with large-amplitude decay in all three. This process has no analogue in the measurements conducted at room temperature. When considering that the 713 nm band has opposite amplitude to the other two ($\Delta T/T < 0$) and is thus concomitant with ESA, it would be reasonable

to attribute the decay in all three bands to another inefficient ground-state relaxation pathway. However, it is notable that this component does not appear at all in the kinetics for the band at 594 nm. An alternative explanation might be that the apparent decay in the 422 and 470 nm bands actually corresponds to a growth in ESA that results from transfer of population from a state that gives rise to the ESA at 713 nm.

The fourth time constant is used to describe the kinetics in all four traces and is found to decrease at longer probe wavelengths (τ_4 = 98, 75, 54 and 43 ps at 422, 470, 594 and 713 nm, respectively). This is associated with another decay channel in TT response at 594 nm, but low-amplitude growth in the three other reported traces. Given the protracted timescale for this process, it may be related to a thermal effect that depends on lattice thermalisation. The thermal difference spectra previously shown in Fig. 5.4 indicate that the effect of film heating from 80 K to, say, 200 K would increase transmittance at bluer wavelengths and decrease transmittance in the NIR. In the context of a TT experiment, this would manifest as GSB at 422, 470 and 594 nm and as ESA at 713 nm, which is consistent with the apparent behaviour of the kinetics on these timescales. However, what is perplexing is the fact that τ_4 for each wavelength is different and appears to grow across the spectrum from the red to the blue rather than conforming to uniform kinetics.

Lineshape and spectral decomposition analysis

To disentangle the kinetics associated with the overlapping spectral components, the difference spectra were subject to decomposition analysis using the same procedure outlined in Chapter 4. As before, the TT data at each time delay was resampled using linear interpolation to conform to an evenly spaced array and represented in terms of wavenumber. While a number of different phenomenological models were trialled, the simplest model was afforded when difference spectra were fitted with a

thermal difference component derived from data presented in Fig. 5.4 to account for the effect of sample heating and two Gaussian functions to represent apparent ESA components observed in Fig. 5.8(b): one centred at 350 nm (ESA_1) and the second at 550 nm (ESA_2). Both ESA components possessed fixed width ($c_{ESA_1} = 1301$ cm^{-1} and $c_{ESA_2} = 1402$ cm^{-1}) and variable amplitude. Both the central positions and widths for the two ESA components were kept fixed over time. Difference spectra at early time delays ($t_{delay} < 0.3$ ps) were omitted from the analysis, and contributions from all included components could be observed immediately from the outset. The outcome of fitting difference spectra for four discrete time delays is presented in Fig. 5.9, alongside the variation in the integrated signal for each component with respect to time.

The lineshape fits provide a coarse approximation of the experimental data at early time delays, although fit quality is improved at later times. This lends support the notion that there is a significant thermal contribution to the difference spectrum alongside at least two overlapping ESA components: one in the UV which accounts for the asymmetry of the primary GSB band and one in the middle of the visible which coincides with the ESA previously shown in Fig. 5.8(b). In the kinetics obtained from the spectral decomposition, the thermal contribution dominated from the outset and could be fitted with three components. This undergoes an early decay process ($\tau = 2.35$ ps), low amplitude growth at prolonged timescales ($\tau = 120$ ps), and a final decay process on ns timescales ($\tau > 2000$ ps). These are consistent with the discrete kinetic analyses for the 422, 470 and 713 nm bands. The ESA components have comparatively small amplitudes, and both conform to tri-exponential kinetics on different timsecales. ESA_2 decays monotonically with fast ($\tau = 0.80$ ps), intermediate ($\tau = 12.7$ ps) and slow components ($\tau = 690$ ps).

In addition to the aforementioned analysis, alternative models were also trialled for spectral decomposition which involved incorporating a GSB component. Inclusion

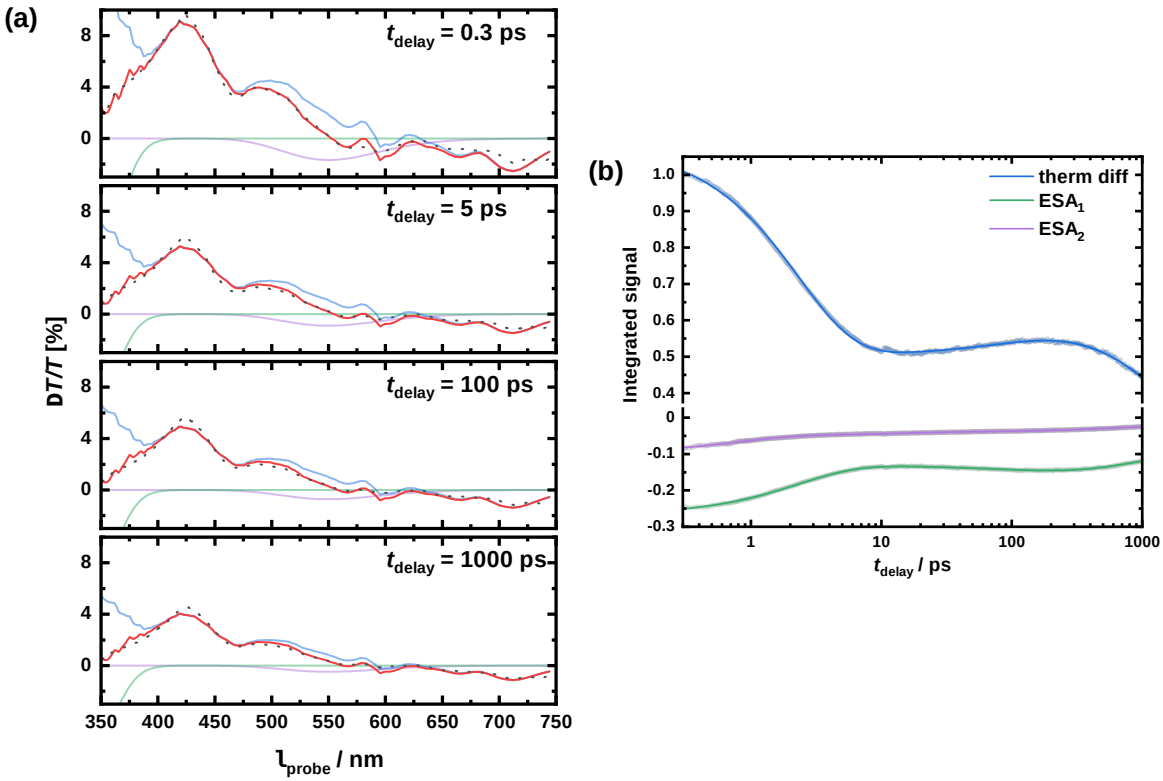

Fig. 5.9 Spectral decomposition analysis for TT data recorded at 80 K. (a) Difference spectra fitted using a spectral decomposition software package for selected time delays. Overlaid are experimental data (black dots), total fits (red lines), and the three component basis functions that comprise the total fit: the thermal difference spectrum obtained by heating to 180 K (blue) and two Gaussians for ESA contributions (green and purple). (b) Kinetics associated with evolution of component function amplitude. Computed values are represented by hollow circles, fits represented by solid lines.

of this in addition to the thermal difference component was found to make minimal improvement on the quality of the fitting; the thermal contribution was found to dominate over the bleach (i.e. thermdiff $> 10 \times$ GSB) at all time delays, while the latter would decay to zero at much faster rates than even the ESA components. This is unsurprising given that the spectral shape of the static and thermal difference spectra is quite similar across most of the visible, which may result in the two being indistinguishable in the context of the analysis. Conversely, if the thermal difference component is omitted but GSB contribution included, it takes a significantly more complicated model to provide an adequate fit to the difference spectra: namely, a GSB and 5 ESA components. In this event, the GSB is observed to increase in intensity over 100 ps timescales in place of the thermal component. The physicality of this is questionable given that the bleach is effectively an indicator of ground-state population; for a pure bleach component to grow would suggest that the ground state is being further depopulated well after photoexcitation. As such, it was deemed necessary to include a thermal difference component as a minimum to obtain a reasonable and sensible fit while the GSB appeared to be redundant.

The apparent dominance of the thermal component at prolonged time delays is not without precedent: previous TT investigations on haematite and $BiVO_4$ thin films also reported primarily thermal contributions after 100 ps [68, 109]. In the latter study, the effects of sample heating were first observed after 10 ps, which is consistent with the onset of the signal growth observed in the data presented here. Thus, the kinetics associated with the slow growth in TT response and indeed the spectral-dependence at long time delays can be ascribed to slower heating effects that occur following photoexcitation.

5.4 Ultrafast magneto-optics

The ultrafast magnetisation dynamics were investigated for the reduced Cr–Cr PBA film using a combination of broadband TR-MCD measurements to determine the spectral-dependence of the transient MO response and single-wavelength time-resolved Faraday ellipticity (TR-FE) investigate the kinetics. These measurements are complementary to those reported so far in this chapter and thus also probe the dynamics upon photoexcitation of the MM′CT at 800 nm. The specific procedural details for each arm of the study are outlined as follows.

Broadband TR-MCD response was determined from the TT data discussed in Section 5.3 through subtracting the spectra obtained for the two applied field directions (i.e. calculating the field-dependent TT response) and is reported as a change in angle, $\Delta\eta_{\mathrm{F}}$, in mdeg.

Single-wavelength TR-FE measurements were conducted using a 20 kHz repetition rate to afford enhanced signal-to-noise using the single-channel detection scheme. Modulation and attenuation of the pump beam at this rate were previously outlined in Section 2.5.3. A 400 nm probe was generated using 800 nm signal output from the OPA, as described in Section 2.5.7. Consecutive TR-FE traces were recorded for magnetic fields of equivalent strength but opposite directions and carefully inspected for any indicators of sample photodegradation or macroscopic heating as a result of the increased repetition rate. When the data were deemed reliable (i.e. no baseline shift before time-zero and similar response upon consecutive scans), traces for each field direction were averaged and the difference calculated to yield only the field-dependent aspect of the ellipticity.

5.4.1 Spectral-dependence of time-resolved magneto-optics

Using the same rationale as the TT experiments, the TR-MCD response of the Cr–Cr PBA film was measured at both room temperature and 80 K to establish the contributions that arise from the paramagnetic phase and magnetically-ordered phase, respectively. These are presented in Fig. 5.10 alongside the steady-state MCD spectra recorded at each respective temperature.

At room temperature, no TR-MCD response is observed that is discernible from baseline noise at any time delay. Likewise, the steady-state MCD spectrum also exhibits no strong features. In contrast, measurements at 80 K shows a clear TR-MCD response, suggesting that magnetic-ordering is required to provide a strong enough $\boldsymbol{B}$-field within the sample for the effect to be measurable.

The low-temperature TR-MCD from the outset closely resembles the shape of the corresponding steady-state MCD at the blue end (<550 nm) of the spectrum, but with opposite sign. This indicates an overall decrease of the MCD across the spectrum upon photoexcitation, which is consistent with demagnetisation and can be viewed as a bleach-like effect. The strength of the response is shown to decay within 10 ps, after which it appears to remain at a constant value for the time delays shown.

It would be expected upon photoexcitation that the shape of the MCD may change: additional peaks may arise as transitions to higher-lying states come into resonance. However, the only noticeable difference between the spectral profiles of the TR-MCD and steady-state MCD is beyond 550 nm, where the former is shown to tail off to zero while the latter is still shown to be negative. The lack of any time-dependence in TR-MCD at these wavelengths would appear to exclude there being an overlapping feature in this region that gives rise to the discrepancy, suggesting that any potential excited-state MCD features are either very weak compared to the bleach contribution or lie outside of the detectable wavelength range.

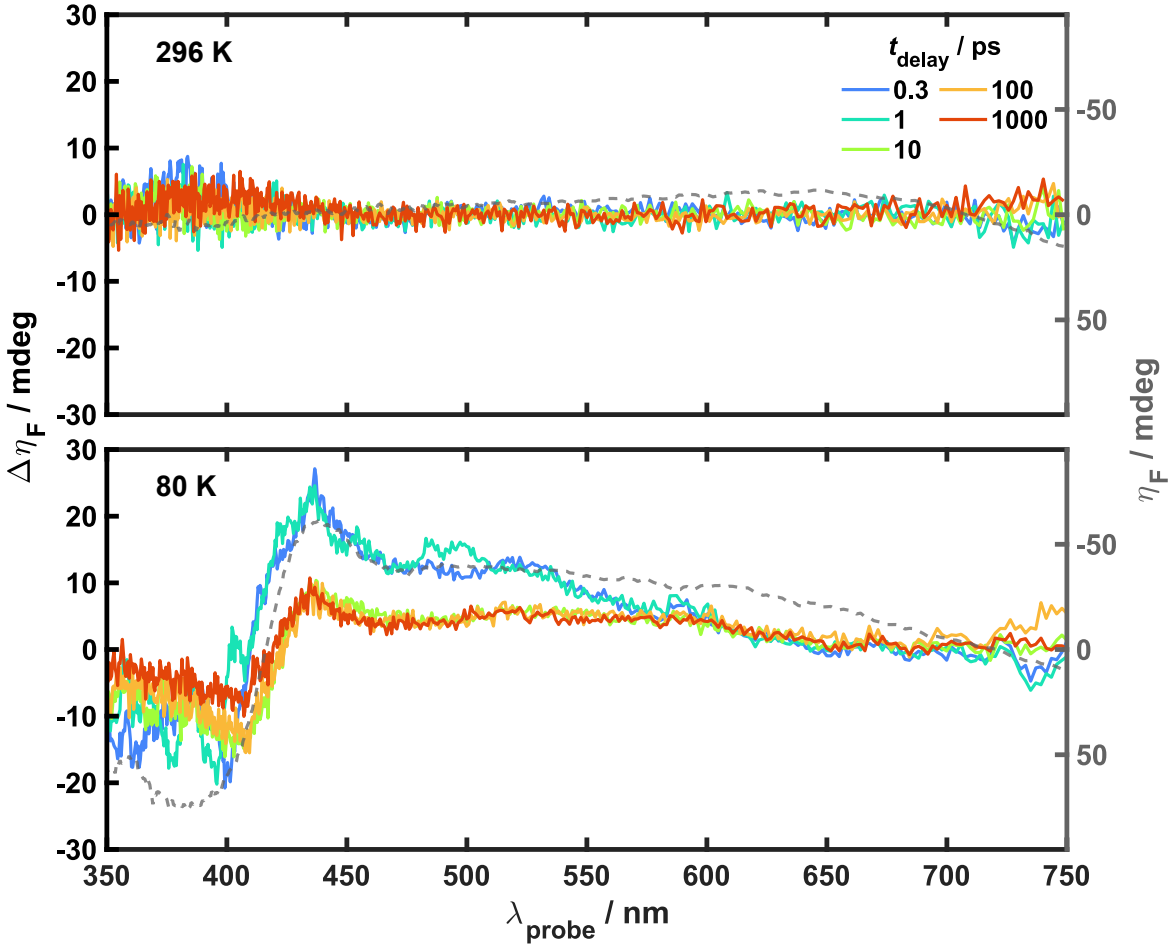

Fig. 5.10 TR-MCD difference spectra obtained for Cr–Cr PBA upon photoexcitation with an 800 nm pump of circular polarisation and fluence 4.2 mJ cm^{-2} under an applied field of 407 mT. Spectra were recorded at 296 K (top) and 80 K (bottom). Overlaid are the steady-state MCD spectra obtained at each respective temperature (grey dotted line, right axis). Note that the y-axes for the steady-state spectra are reversed.

5.4.2 Kinetics of time-resolved magneto-optics

The time-dependence of the magnetisation dynamics was observed using polarimetric TR-FE measurements at 80 K under an applied field of 65 mT (enough to magnetically saturate the film) having been photoexcited at 800 nm with a 4.2 mJ cm^{-2} circularly-polarised pump pulse. The resultant kinetic trace was compared to data obtained from broadband TT measurements at 1 kHz. To match the conditions of the polarimetric experiment as much as possible, the TT data were recorded using an equivalent pump fluence and polarisation. From this, a kinetic trace was generated through the Gaussian-weighted average of the spectrally-resolved data with a central wavelength (400 nm) and bandwidth (5.89 nm) selected to match those expected of the probe in the polarimetric experiments. Both traces were fitted using identical triexponential models; these are illustrated in Fig. 5.11, while fitted parameters are tabulated in Table 5.3.

It is clear from the raw data that the traces follow similar kinetics for the first few ps before there is some divergence; while there is slight growth in the TT at prolonged time delays, the amplitude is dramatically increased in the TR-FE trace and the magnitude of $\Delta\eta_F$ is observed to exceed the initial maximum observed immediately after photoexcitation ($\Delta\eta_F = -20.3$ mdeg at 1000 ps *vs.* -17.7 mdeg at 0.2 ps). Kinetic analyses indicate that the time constants for each exponential component are similar between the two experiments, suggesting that each decay/growth channel originates from the same dynamical processes. The difference in the late signal growth is instead accounted for in the corresponding amplitudes: the ratio $|A_2/A_1|$ observed for the TR-FE vastly exceeds that of the TT (1.15 *vs.* 0.1).

The dramatic difference in the late growth between the TT and TR-FE can be attributed to the greater sensitivity of the magnetisation dynamics to temperature compared to the electronic component. For instance, the thermal difference spectra (Fig. 5.4) indicate that an increase in transmittance of 0.07 ($\sim$1/3 of the original value)

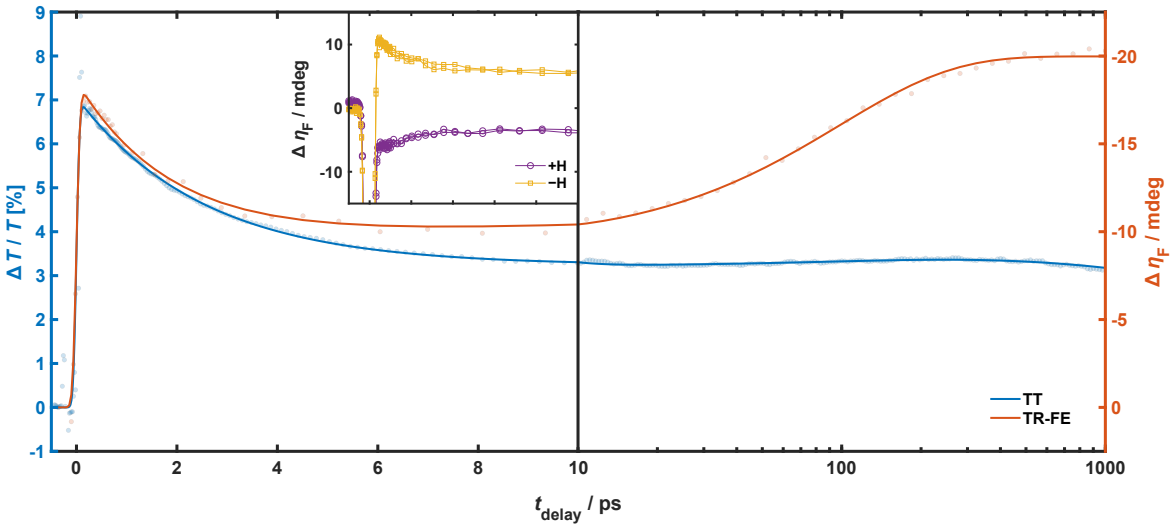

Fig. 5.11 TT and TR-FE kinetics observed in 400 nm probe upon photoexcitation at 800 nm with a circularly-polarised pump of fluence 4.2 mJ cm^{-2}. The sample was held at 80 K and under an applied field of 65 mT. Recorded values are represented by filled circles, fits represented by solid lines. Note that the TR-FE y-scale is reversed for easier visual comparison of kinetic timescales. Inset: Consecutive TR-FE traces obtained for each applied field direction.

Table 5.3 Fit parameters obtained from kinetic analyses of the TT and TR-FE data presented in Fig. 5.11.

Experiment	Amplitude			Time constant / ps		
	A_1	A_2	A_3	τ_1	τ_2	τ_3
TT	1.9(1)	−0.132(7)	1.740(7)	2.52(1)	130(10)	≫1000
TRFE	−4.62(9)	5.3(2)	−10.0(2)	1.9(1)	99(7)	≫1000

is observed when heating the film from 80 to 296 K. A proportionally greater change in the MO response might be observed as this temperature increase would bring the film to well-above the T_c and thus to the paramagnetic phase regime where magnetisation is extremely weak by comparison.

Fluence-dependence

In principle, the amount of macroscopic heating observed will be determined by the laser fluence used for optical pumping as higher fluence will excite more sites within the sample and provide more point sources of heat. Thus, the fluence-dependence of the TR-FE can give credence to thermal effects dominating the late-time dynamics. Thus, TR-FE data were acquired at 80 K having excited with seven different laser fluences and subject to the same kinetic analysis as before. The resultant kinetic traces and their fits are provided in Fig. 5.12 while the fitted parameters are summarised in Table 5.4.

Visual inspection of the kinetic traces reveals that the initial TR-FE response appears to increase consistently with fluence, while there is quite a stark difference between the levels of slow growth observed at 3.3 and 4.2 mJ cm^{-2} compared to the lower fluences. Kinetic analyses of the traces revealed no discernible trends in the timescales with respect to growth, other than greater precision in the time constants associated with growth at the higher fluences. Conversely, there were clearer relationships between fluence and the amplitudes for the fast decay and slow growth processes: A_1 was broadly linear with respect to fluence while A_2 clearly deviated from linear behaviour at the highest fluence. $|A_2/A_1|$ can be used to represent the relative strength of the growth with respect to the initial decay and is observed to provide a minor contribution ($|A_2/A_1| < 1$) to the late dynamics until 4.2 mJ cm^{-2} where is it seen to dominate ($|A_2/A_1| > 1$). These findings are consistent with heating effects as outlined previously:

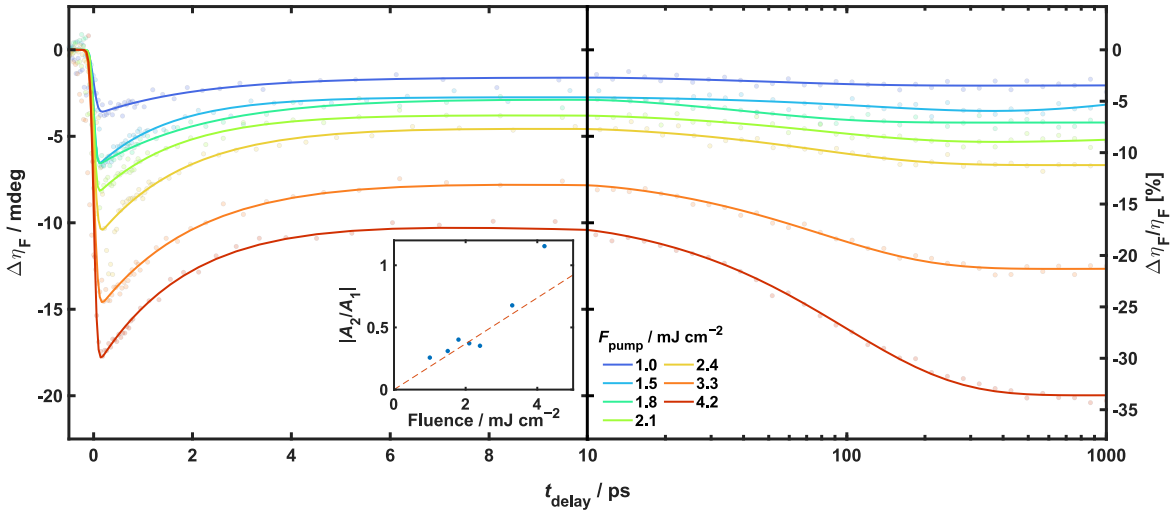

Fig. 5.12 TR-FE kinetics observed for a 400 nm probe upon photoexcitation at 800 nm with a circularly-polarised pump of varied fluence. Recorded values are represented by filled circles, fits represented by solid lines. The scale on the right axis indicates the relative change in TR-FE observed with respect to the steady-state spectrum. Inset: fluence-dependence of the amplitude-ratio for slow growth/fast decay obtained from kinetic analysis.

Table 5.4 Fit parameters obtained from kinetic analyses of the fluence-dependent TR-FE data presented in Fig. 5.12. Values labelled with (*) possess an uncertainty much greater than the quantity itself.

Fluence	Amplitude			Time constant / ps		
/ mJ cm^{-2}	A_1	A_2	A_3	τ_1	τ_2	τ_3
1.0	−1.14(8)	0.29(9)	−1.03(8)	2.2(4)	50(40)	≫1000
1.5	−2(∗)	0.6(∗)	−2(∗)	1.5(1)	160(100)	≫1000
1.8	−2.2(2)	0.88(9)	−2.11(6)	2.4(2)	40(10)	≫1000
2.1	−2.48(7)	0.9(1)	−2.7(1)	1.7(1)	80(20)	≫1000
2.4	−3.4(1)	1.2(1)	−3.3(1)	1.8(1)	80(20)	≫1000
3.3	−4.1(1)	2.8(1)	−6.3(1)	2.1(1)	79(9)	≫1000
4.2	−4.62(9)	5.3(2)	−10.0(2)	1.9(1)	99(7)	≫1000

higher pump fluence deposits more energy in the sample, with the onset of non-linear behaviour likely occurring when the sample is heated to temperatures closer to the T_c.

5.4.3 Time-resolved hysteresis

To test the field-dependence of the magnetisation dynamics, which could provide additional information such as any change in coercivity, the time-resolved hysteresis was determined for the film at 80 K. These involved measurement of TR-FE hysteresis loops for finite time delays at the pump-modulated frequency. As acquisition time for these measurements was considerably long and laser repetition rate high, an 800 nm pump of lower fluence (2.1 mJ cm^{-2}) was used to mitigate sample heating and photodegradation. Static hysteresis loops recorded before and after the measurements were identical, indicating that these mitigation efforts were successful. The resultant loops are provided in Fig. 5.13. Note that these loops show the change in ellipticity ($\Delta\eta_F$) at each time delay rather than the absolute ellipticity.

The shape of the hysteresis loops was observed to match that of the static measurements (Fig. 5.2) but reflected in the y-axis. This indicates that the absolute value of η_F decreases towards zero upon measurement; thus, larger values of $\Delta\eta_F$ correspond to a greater loss of magnetisation.

The saturation values of $\Delta\eta_F$ (i.e. maxima observed when $|\mu_0 H| > 50$ mT) appear to follow the same trend as the TR-FE kinetics: an initially strong demagnetisation ($t_{delay} = 0.3$ ps) which decays to weaker values within a few ps ($t_{delay} = 3, 20$ ps) before growing again at protracted timescales ($t_{delay} = 130, 1000$ ps). The coercivity for all positive time delays is slightly smaller than that observed for the static hysteresis measurement ($\mu_0 H_c$ = 11–13 mT *vs.* 15 mT). However, the inherent noise in the time-resolved data — particularly at the earlier time delays — hinders calculation of precise values. Nevertheless, the lower coercivity upon optical pumping is consistent

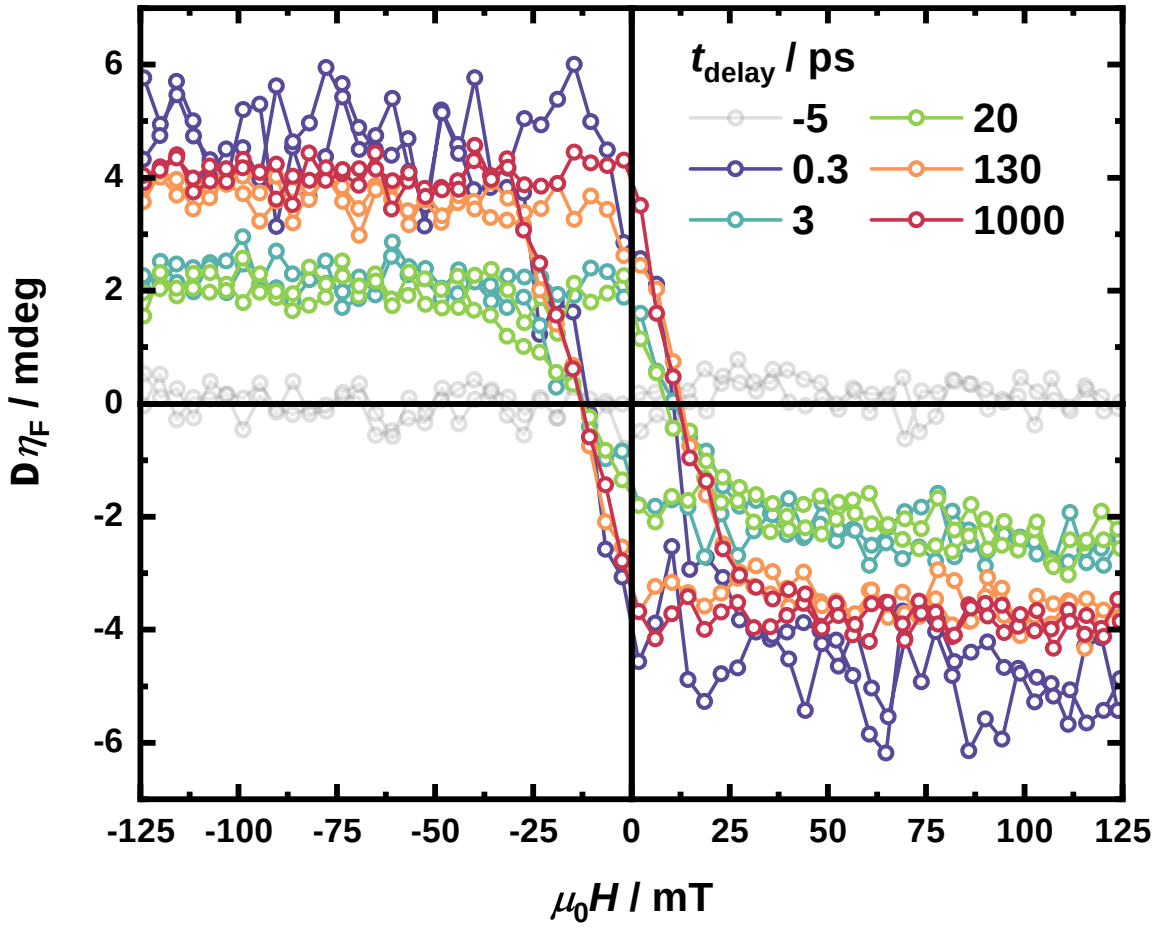

Fig. 5.13 Time-resolved magnetic hysteresis loops recorded at 80 K with an 800 nm pump of fluence 2.1 mJ cm^{-2} and circular polarisation. Data was obtained through TR-FE using a 400 nm probe beam originating from the OPA at a repetition rate of 20 kHz.

with either a thermal effect or a change in magnetic anisotropy. However, given the apparent prevalence of thermal effects in both the TT and TR-FE kinetics, this is more likely to be the dominant cause here.

5.5 Interpretation of ultrafast dynamics

In summary, photoexcitation of the NIR MM′CT transition in Cr–Cr PBA at 800 nm induces an ultrafast TT and TR-FE response whose kinetics both conformed to the same timescales under similar pump and probe conditions: the initial response appears within the width of the IRF (<0.1 ps), decays on fast timescales ($\tau \sim 2.5$ ps), undergoes a much slower growth ($\tau \sim 100$ ps) and appears to relax on protracted timescales that far exceed the time delays accessible with the experiments ($\tau \gg 1000$ ps). All this indicates that the electronic and magnetisation dynamics are inextricably linked.

Comparison of TT data at later time delays to steady-state thermal difference spectra highlighted key similarities, suggesting that the long-term electronic dynamics observed are a result of sample heating. The slow growth in the TT and TR-FE occurs on timescales consistent with heating effects reported in ultrafast pump–probe studies of semiconductor thin films in literature [67, 68, 109]. While variation of pump fluence was found to have no discernible impact on the kinetic timescales of the TR-FE response, it did have a profound effect on the amplitude of the growth; this showed non-linear dependence with increasing fluence and actually dominated over the initial demagnetisation at the highest fluences. As increased pump fluence results in more sites being excited throughout the material and thus generation of more heat, these observations are also consistent with heating effects.

Attribution of the early-time dynamics in both the TT and TR-FE is more ambiguous, given that there appears to be wavelength-dependence in the former. Kinetic analyses of four bands scattered across the TT spectrum at low temperature indicated

that most of it evolves on the same timescales summarised previously, suggesting a common point of origin. The exception to this was the band situated at 594 nm where the kinetics were unique: the TT response appeared from the outset, conformed to multiexponential decay on two sub-ps timescales and was not shown to grow in magnitude at any stage. That this exhibits distinct early kinetics from the other three wavelengths would indicate that the early dynamics involve at least two independent excited states which are both populated either upon pump absorption or on timescales that are faster than the IRF of the measurement. Spectral decomposition analysis indicated that the feature at 594 nm was a genuine ESA superimposed onto a broad, primary component that could be described by the thermal difference spectrum, even at these early time delays.

First guesses to a model for the electronic dynamics can be made based on the interpretation of the steady-state electronic spectrum. Section 5.2.2 discussed the origin of the NIR absorption band which arises when $B = Cr^{II}_{LS}$ is present in the material and was attributed to MM′CT between these and neighbouring $A = Cr^{II}_{HS}$. This will transiently generate highly distorted Cr^{III} and Cr^{I}; while the former is a stable configuration and commonly forms TM complexes, the latter is generally not found on account of its low stability and tendency to oxidise to Cr^{III}. Thus, a short lifetime would be expected for such a state and the primary decay channel to be through back-electron transfer (BET) between the original two sites. The presence of the visible ESA component from the outset and its rapid decay are consistent with this, and thus could be assigned to a transition from this initially populated state. This tentative assignment echoes the findings of two separate ultrafast studies on colloidal suspensions of Prussian blue nanoparticles. In both cases, the red-side of the MM′CT was pumped and probed at 800 nm; immediately following photoexcitation, GSB was observed within the IRF and found to decay within 1 ps [110, 111]. This process was

also attributed to BET giving rise to a vibrationally hot ground state from which an ESA could subsequently be observed [111].

While the aforementioned assignments of the visible ESA kinetics and slow heating effects seem plausible and are supported by literature, there are a number of outstanding issues. The first is that the origin of the early kinetics exhibited by the 422, 470 and 713 nm bands in the TT measurements is not immediately intuitive. Since they manifest as a GSB peak, a GSB trough (likely an overlapping ESA) and another ESA peak, respectively, logic would suggest that these arise from a second low-lying state that is populated either directly by the pump pulse or faster than the experimental time resolution. That these signals are long-lived and are only observed to undergo decay on ∼2 ps timescales suggests that said state may possess a thermal barrier to deactivation that may only be overcome at early times when still vibrationally hot. When considering the mixed-valence nature of this material, in which both Cr^{II} and Cr^{III} can be found in both A- and B-sites with various ligand-field strengths, assignment of this unidentified state is difficult without the aid of computational insight. Nevertheless, given the common kinetics, it is clear that pinpointing the origin of these dynamics is key to understanding what gives rise to the magnetisation dynamics observed in the TR-FE.

It is interesting to note that all three of the aforementioned TT bands appeared to conform well to the shape of the thermal difference spectrum from the outset of the dynamics. While this conveniently provides a common origin and thus accounts for the similar early kinetics, attributing their origin to a heating effect on ultrafast timescales is questionable; as already established, thermalisation is not an instantaneous process and its effects would be expected to grow in over time. Use of the steady-state spectrum as a basis function to account for GSB at early times provides a model that seems more physical, although it then becomes necessary to include a number of additional ESA

components (at least four) to account for the above features which were previously described well by the thermal difference spectra.

The composition of the overall sample — a thin film of Cr–Cr PBA deposited onto a conductive glass substrate and encapsulated with adhesive and a glass coverslip — must be taken into consideration in order to ensure that only dynamics pertaining from the material of interest are being investigated. To this end, complementary pump–probe measurements were performed on a blank position of the sample with no film coverage under the same experimental conditions (i.e. temperature, pump wavelength and fluence) to determine any unwanted background response. Said measurements concluded that there is no significant TT or TR-MCD signal beyond XPM around time-zero. Nevertheless, it is possible that there are unwanted, non-spectroscopic contributions to the dynamics. For instance, the intensity of the pump pulse may be high enough to excite vibrational overtone and/or combination bands within the adhesive which could induce secondary heating in the film. Thus, it may be helpful to characterise the vibrational spectrum of the adhesive and ascertain whether any reasonable combination of fundamental vibrational frequencies and their harmonics may match the energy provided by the 800 nm pump in order to rule out said effects.

5.6 Conclusion

The electronic and magnetisation dynamics in mixed-valence Cr–Cr PBA have been investigated using a combination of TT and TR-MCD/TR-FE measurements. Experiments involving photoexcitation at 800 nm at low temperature indicated that both the magnetisation and electronic dynamics are quite similar, which have been attributed to the population an as-yet unidentified electronic state. A second TT feature evolves with distinctively different dynamics and is assigned to ESA arising from a pump-induced MM′CT that undergoes rapid decay upon BET, as has previously been observed in literature [110, 111]. Slow growth in the kinetics observed at long-time delays is consistent with thermal effects [67, 68, 109] and underlines the importance of sensibly accounting for these in the interpretation of the TT spectra.

In the discussion of the steady-state spectrum provided in Fig. 5.3, a second transition at 383 nm (tentatively attributed to Cr^{III}) was identified as a potential target for optical pumping in further experiments. This was previously the focus of our work, but came with an increased risk of photodegradation which could be observed much more quickly than when exciting at 800 nm. While it was our intention to return to these measurements, the film used in the study delaminated before the opportunity arose, which prevented any more reliable data from being collected. In the same vein, TT and TR-MCD experiments have also been performed having photoexcited the shoulder observed at 514 nm; analysis of this data is ongoing, and as such, these measurements have not been presented in this work.

To provide a comprehensive view of the dynamics observed in photoexcited Cr–Cr PBA, it is crucial to assign the unidentified state observed in the TT and TR-FE. In Section 5.5, quantum mechanical calculations were touted as a means to narrow down the list of sensible candidates from a large number of possible states. The density functional calculations reported by Rogers and Johansson used a $Cr^{II}_{HS}(NC)_5-NC-Cr^{III}(CN)_5$

dimeric unit to approximate Cr^{II}_{HS}–Cr^{III} PBA; these identified the frontier orbitals, their atomic contributions and the transition energy associated with the MM′CT [103]. The same approach has also been used to inform the ultrafast dynamics observed in Co–Fe PBA with reasonable success [32]. Thus, this treatment could also be applied to dimers used to represent the remaining stoichiometric permutations that might be expected to be present in the material studied (i.e. Cr^{II}_{HS}–Cr^{II}_{LS}, Cr^{III}–Cr^{II}_{LS} and Cr^{III}–Cr^{III}) and the energetics of the lower-lying states used to exclude some of the possibilities. Additional insight into any states involved could also be provided experimentally. For instance, the unique C≡N stretch frequencies observed for Cr^{III}–CN and Cr^{II}–CN coordination environments, previously outlined in Section 2.2.2, renders the use of time-resolved IR measurements employing an optical pump/IR probe viable. These experiments could identify whether an excited state populated at any given time delay is simply localised on A/B-sites or involves both (i.e. charge-transfer) depending on how the vibrational bands of each coordination environment are affected, thus providing information that is complementary to the TT measurements. Likewise, time-resolved X-ray spectroscopies may also be used to the same effect, as demonstrated by Cammarata *et al.* in their studies on Co–Fe PBA [32]. However, as the latter techniques require the use of advanced light sources only available only at large facilities (i.e. synchrotrons and X-ray free electron lasers), such measurements would be subject to beamtime availability and funding restrictions.

The current interpretation of the dynamics that ensue upon photoexcitation of Cr–Cr PBA at 800 nm is based on attribution of the NIR feature observed in its electronic spectrum to MM′CT. However, as suggested in Section 5.2.2, there remains some ambiguity in this assignment: since the material's physical properties conform to those characteristic of class II mixed-valence systems [108] and isolated Cr^{II}_{LS} has also been observed to possess a broad peak at 1100 nm [107], it is possible that this

localised transition may contribute to the NIR absorption. While the temperature-dependent transmittance spectra presented in Fig. 5.4 sought clarification on this, said measurements were limited to the visible region and lacked the sensitivity to provide consistent results with decreasing temperature. Thus, it is pertinent that the nature of said transition — and indeed the rest of the resolvable spectral features — be confirmed with further work. This might be realised with the aforementioned computational studies, which would involve matching calculated transition energies and oscillator strengths to experimentally observed spectral features upon factoring in material stoichiometry into their intensities. Likewise, the same outcome could also be achieved with further experiments. For instance, the comparison of Cr–Cr PBA spectra to those of relevant Cr^{III} systems presented in Fig. 5.4 could be extended to also include isolated HS and LS Cr^{II} complexes, provided that the risk of air-oxidation of these species could be mitigated. If the stoichiometry were again taken into consideration, the superposition of the individual spectra should overlap well with corresponding features in the spectrum for Cr–Cr PBA, and any additional features observed could be attributed to MM′CT. Alternatively, spectroelectrochemistry could determine how a film's electronic spectrum is changed in response to electrochemical reduction or oxidation, which would help to characterise the features associated with the two extremes of Cr^{III}–Cr^{III} (fully oxidised) and Cr^{II}_{HS}–Cr^{II}_{LS} (fully reduced) and any intermediates [106, 112] without the need for comprehensive stoichiometric evaluation.

Both existing literature and the studies presented in this chapter have shown that performing a complete determination of the structural, spectral and magnetic properties of Cr–Cr PBA is not trivial. The numerous different sample requirements for various characterisation techniques — exposed films for reflection IR and AFM, transparent films for UV–visible–NIR transmission, awkward dimensions for SQUID magnetometry, *etc.* — make complete characterisation of a single film without risk

of air-oxidation virtually impossible. Thus, this work has relied on identifying trends observed upon characterisation of different films and inferring physical properties based on this. Nevertheless, there is still a lack of quantitative stoichiometric analysis of our films; as the preceding discussion has highlighted, this would greatly aid in efforts to assist both the assignment of the steady-state spectrum and consequently the interpretation of the ultrafast dynamics observed in the material. Stoichiometric evaluation reported for PBAs in literature is typically performed using elemental analysis on powders, with the assignment of oxidation states in mixed-valence systems performed by considering charge balance requirements [19, 48, 49, 60, 113]. Non-destructive techniques that are capable of characterising mixed-valence systems include an array of X-ray spectroscopies, namely X-ray photoemission [60, 70, 114], absorption and fluorescence [115–118]. However, the energy separation of features associated with different oxidation states can be too narrow to resolve with commercially available laboratory apparatus, which again limits the use of these techniques to specialised facilities such as synchrotrons. It is possible to instead obtain a partial stoichiometric evaluation by following an approach used Buschmann *et al.* in their studies of Cr–Cr PBA films. This involved comparison of IR peak integrals for the characteristic C≡N stretch bands associated with the $Cr^{III}-CN$ and $Cr^{II}-CN$ coordination environments having normalised the intensity for each using vibrational spectra obtained for films exhibiting the two extremes of stoichiometry (i.e. Cr^{III}–Cr^{III} and Cr^{II}_{HS}–Cr^{II}_{LS}), which was able to provide the Cr^{III}/Cr^{II} ratio for B-sites [60].

Chapter 6

Summary and outlook

This thesis detailed the preparation of Cr(III)-based PBA thin films suitable for study using all-optical pump-probe techniques. These samples were then subject to investigation using complementary TT and TR-MO measurements to determine the nature of their photoinduced electronic and magnetisation dynamics. Alongside this, a parallel TA study was conducted on $[Cr(CN)_6]^{3-}$ in an attempt to confirm the current model being used to describe the dynamics that ensue upon photoexcitation of localised Cr(III) transitions in relevant PBAs.

The adapted sample preparation procedure involved encapsulation of thin films by a transparent adhesive — either self-cured cyanoacrylate glue or a UV-cured optical adhesive — and glass coverslip. The process was found to dramatically increase transmittance when applied to both Cr–Cr and Fe–Cr PBA, even when the films were of considerable thickness, and is thought to be the result of a refractive index-matching effect that effectively smooths the rough surface of the films to form a uniform optical phase and reduce scatter. The ability of two adhesives of known refractive index to reduce opacity was compared, although neither consistently outperformed the other. Vibrational spectra taken before and after encapsulation with the UV-cured adhesive indicated that the this does not undergo reaction with the films. This was supported

by MO hysteresis loops measured for encapsulated films, which exhibited the expected magnetic properties.

The TA study on $[Cr(CN)_6]^{3-}$ dissolved in H_2O identified a single, broad ESA feature in the UV which appeared to narrow and grow in intensity over time. Spectral decomposition analysis indicated that this actually consisted of two overlapping ESA bands which evolve with distinct kinetics: a primary, broad feature appears within the time-resolution of the experiment and undergoes fast decay to a plateau within a few ps, while a secondary, narrower feature grows in to reach a plateau over a few ps. Ground state relaxation is not observed within the timescales accessible with the measurement, indicating that the states giving rise to both features are long-lived. Three hypotheses have been proposed for the origin of the bands: these attribute them to a combination of an excited quartet state, an excited spin-flipped doublet state, and a feature arising from a photoproduct generated by optical pumping. Future measurements conducting the same study but in different solvent may help to narrow down the possibilities.

Ultrafast TT and TR-MO studies focussed on films of mixed-valence Cr–Cr PBA on account of their accessible T_c and consistently measurable magnetic properties. Steady-state spectroscopic and magnetometric characterisation indicated that more heavily reduced Cr–Cr PBA exhibited more intense absorption bands and higher coercivity, thus making them more amenable to all-optical experiments than their oxidised counterparts. Two clear features in the electronic spectrum — a peak at 380 nm and a broad rising absorption in the NIR — have been identified as viable candidates for optical pumping. Photoexcitation at 800 nm was found to produce strong TT features and consistent results in TR-MO measurements with a low risk of photodegradation. The TT spectrum consists of a broad, complex feature reminiscent of thermal difference spectrum with a superimposed ESA, while the shape of the TR-MCD closely matched that of the reversed steady-state MCD spectrum and thus

is analogous to GSB. Kinetic analyses of the TT and TR-MO indicate that the early dynamics for both evolve on identical timescales, similarly to V–Cr PBA. Both TT and TR-MO then exhibit effects consistent with sample heating at prolonged time delays. Efforts are ongoing to assign the electronic states responsible for the dynamics; given the complexity of the material, this is likely to require further characterisation and computational insight.

While it was the intention to expand the magnetisation studies to Fe–Cr PBA, we have so far been unable to detect magnetic ordering using the equipment here in Edinburgh because of its low T_c. Nevertheless, the improvements in sample preparation and development of a suitable framework to aid in the measurement of electronic and magnetisation dynamics in polycrystalline thin films may facilitate these measurements in the future.

References

[1] S. N. Piramanayagam. Perpendicular recording media for hard disk drives. *Journal of Applied Physics*, 102(1):011301, jul 2007.

[2] C. Chappert, A. Fert, and F. Nguyen Van Dau. The emergence of spin electronics in data storage. *Nature Materials*, 6(11):813–823, nov 2007.

[3] S. Kasap and P. Capper, editors. *Magnetic Information-Storage Materials*, pages 1185–1223. Springer International Publishing, 2017.

[4] M.H. Kryder, E.C. Gage, T.W. McDaniel, W.A. Challener, R.E. Rottmayer, Ganping Ju, Yiao-Tee Hsia, and M.F. Erden. Heat assisted magnetic recording. *Proceedings of the IEEE*, 96(11):1810–1835, nov 2008.

[5] A. Kirilyuk, A. V. Kimel, and T. Rasing. Ultrafast optical manipulation of magnetic order. *Reviews of Modern Physics*, 82(3):2731–2784, sep 2010.

[6] M. Faraday. I. experimental researches in electricity.—nineteenth series. *Philosophical Transactions of the Royal Society of London*, 136:1–20, dec 1846.

[7] E. Beaurepaire, J.-C. Merle, A. Daunois, and J.-Y. Bigot. Ultrafast spin dynamics in ferromagnetic nickel. *Physical Review Letters*, 76(22):4250–4253, may 1996.

[8] F. Hansteen, A. V. Kimel, A. Kirilyuk, and T. Rasing. Nonthermal ultrafast optical control of the magnetization in garnet films. *Physical Review B*, 73(1), jan 2006.

[9] A. Stupakiewicz, K. Szerenos, D. Afanasiev, A. Kirilyuk, and A. V. Kimel. Ultrafast nonthermal photo-magnetic recording in a transparent medium. *Nature*, 542(7639):71–74, jan 2017.

[10] J. S. Miller and A. J. Epstein. Molecule-based magnets—an overview. *MRS Bulletin*, 25(11):21–30, nov 2000.

[11] D. R. Talham and M. W. Meisel. Thin films of coordination polymer magnets. *Chemical Society Reviews*, 40(6):3356, 2011.

[12] M. B. Robin. The color and electronic configurations of Prussian Blue. *Inorganic Chemistry*, 1(2):337–342, may 1962.

[13] D. Davidson and L. A. Welo. The nature of Prussian Blue. *The Journal of Physical Chemistry*, 32(8):1191–1196, jan 1927.

[14] A. Ito, M. Suenaga, and K. Ôno. Mössbauer study of soluble Prussian Blue, insoluble Prussian Blue, and Turnbull's Blue. *The Journal of Chemical Physics*, 48(8):3597–3599, apr 1968.

[15] F. Herren, P. Fischer, A. Ludi, and W. Haelg. Neutron diffraction study of Prussian Blue, $Fe_4[Fe(CN)_6]_3.xH_2O$. Location of water molecules and long-range magnetic order. *Inorganic Chemistry*, 19(4):956–959, apr 1980.

[16] M. Verdaguer and G. S. Girolami. Magnetic prussian blue analogs. In *Magnetism: Molecules to Materials V*, pages 283–346. Wiley-VCH Verlag GmbH & Co. KGaA, jul 2005.

[17] H. Tokoro and S. i. Ohkoshi. Novel magnetic functionalities of Prussian blue analogs. *Dalton Transactions*, 40(26):6825, 2011.

[18] Kim R. Dunbar and Robert A. Heintz. Chemistry of transition metal cyanide compounds: Modern perspectives. In *Progress in Inorganic Chemistry*, pages 283–391. John Wiley & Sons, Inc., mar 1996.

[19] T. Mallah, S. Thiebaut, M. Verdaguer, and P. Veillet. High-T_c Molecular-Based Magnets: Ferrimagnetic Mixed-Valence Chromium(III)-Chromium(II) Cyanides with T_c at 240 and 190 Kelvin. *Science*, 262(5139):1554–1557, dec 1993.

[20] E. Ruiz, A. Rodríguez-Fortea, S. Alvarez, and M. Verdaguer. Is It Possible To Get High T_C Magnets with Prussian Blue Analogues? A Theoretical Prospect. *Chemistry - A European Journal*, 11(7):2135–2144, jan 2005.

[21] R. Klenze, B. Kanellakopulos, G. Trageser, and H. H. Eysel. Manganese hexacyanomanganate: Magnetic interactions via cyanide in a mixed valence Prussian blue type compound. *The Journal of Chemical Physics*, 72(11):5819–5828, jun 1980.

[22] W.-D. Griebler and D. Babel. Röntgenograpliische und magnetische Untersuchungen an perowskitverwandten Cyanoverbindungen $CsM^{II}M^{III}(CN)_6$ / X-Ray and Magnetic Studies of Perovskite-Related Cyano Compounds $CsM^{II}M^{III}(CN)_6$. *Zeitschrift für Naturforschung B*, 37(7):832–837, jul 1982.

[23] V. Gadet, T. Mallah, I. Castro, M. Verdaguer, and P. Veillet. High-T_C molecular-based magnets: a ferromagnetic bimetallic chromium(III)-nickel(II) cyanide with $T_C = 90$ K. *Journal of the American Chemical Society*, 114(23):9213–9214, nov 1992.

[24] M. Verdaguer, A. Bleuzen, V. Marvaud, J. Vaissermann, M. Seuleiman, C. Desplanches, A. Scuiller, C. Train, R. Garde, G. Gelly, C. Lomenech, I. Rosenman, P. Veillet, C. Cartier, and F. Villain. Molecules to build solids: high T_C molecule-based magnets by design and recent revival of cyano complexes chemistry. *Coordination Chemistry Reviews*, 190-192:1023–1047, sep 1999.

[25] S. Ferlay, T. Mallah, R. Ouahès, P. Veillet, and M. Verdaguer. A room-temperature organometallic magnet based on Prussian blue. *Nature*, 378(6558):701–703, dec 1995.

[26] O. Sato, T. Iyoda, A. Fujishima, and K. Hashimoto. Photoinduced magnetization of a cobalt-iron cyanide. *Science*, 272(5262):704–705, may 1996.

[27] O. Sato, Y. Einaga, T. Iyoda, A. Fujishima, and K. Hashimoto. Reversible photoinduced magnetization. *Journal of The Electrochemical Society*, 144(1):L11–L13, jan 1997.

[28] O. Sato, Y. Einaga, A. Fujishima, and K. Hashimoto. Photoinduced long-range magnetic ordering of a cobalt-iron cyanide. *Inorganic Chemistry*, 38(20):4405–4412, sep 1999.

[29] H. Kamioka, Y. Moritomo, W. Kosaka, and S. Ohkoshi. Dynamics of charge-transfer pairs in the cyano-bridged Co^{2+}–Fe^{3+} transition-metal compound. *Physical Review B*, 77(18):180301, may 2008.

[30] Y. Moritomo, H. Kamioka, T. Shibata, S. Nozawa, T. Sato, and S. i. Adachi. Photoinduced Phase Transition into a Hidden Phase in Cobalt Hexacyanoferrate as Investigated by Time-Resolved X-ray Absorption Fine Structure. *Journal of the Physical Society of Japan*, 82(3):033601, mar 2013.

[31] S. Zerdane, M. Cammarata, L. Balducci, R. Bertoni, L. Catala, S. Mazerat, T. Mallah, M. N. Pedersen, M. Wulff, K. Nakagawa, H. Tokoro, S. i. Ohkoshi, and E. Collet. Probing Transient Photoinduced Charge Transfer in Prussian Blue Analogues with Time-Resolved XANES and Optical Spectroscopy. *European Journal of Inorganic Chemistry*, 2018(3-4):272–277, jul 2017.

[32] M. Cammarata, S. Zerdane, L. Balducci, G. Azzolina, S. Mazerat, C. Exertier, M. Trabuco, M. Levantino, R. Alonso-Mori, J. M. Glownia, S. Song, L.Catala, T. Mallah, S. F. Matar, and E. Collet. Charge transfer driven by ultrafast spin transition in a CoFe Prussian blue analogue. *Nature Chemistry*, 13(1):10–14, dec 2020.

[33] T. H. Maiman. Stimulated optical radiation in ruby. *Nature*, 187(4736):493–494, aug 1960.

[34] L. S. Forster. The photophysics of chromium(III) complexes. *Chemical Reviews*, 90(2):331–353, mar 1990.

[35] A. D. Kirk. Photochemistry and photophysics of chromium(III) complexes. *Chemical Reviews*, 99(6):1607–1640, may 1999.

[36] L. S Forster. Thermal relaxation in excited electronic states of d^3 and d^6 metal complexes. *Coordination Chemistry Reviews*, 227(1):59–92, apr 2002.

[37] C. Förster and K. Heinze. Photophysics and photochemistry with earth-abundant metals – fundamentals and concepts. *Chemical Society Reviews*, 49(4):1057–1070, 2020.

[38] Y. Tanabe and S. Sugano. On the absorption spectra of complex ions II. *Journal of the Physical Society of Japan*, 9(5):766–779, sep 1954.

[39] L. S. Forster. Intersystem crossing in transition metal complexes. *Coordination Chemistry Reviews*, 250(15-16):2023–2033, aug 2006.

[40] E. A. Juban and J. K. McCusker. Ultrafast Dynamics of ^{2}E State Formation in $Cr(acac)_3$. *Journal of the American Chemical Society*, 127(18):6857–6865, apr 2005.

[41] J. O. Johansson, J.-W. Kim, E. Allwright, D. M. Rogers, N. Robertson, and J.-Y. Bigot. Directly probing spin dynamics in a molecular magnet with femtosecond time-resolution. *Chemical Science*, 7(12):7061–7067, 2016.

[42] M. Mizuno, S. Ohkoshi, and K. Hashimoto. Electrochemical Synthesis of High-T_c, Colored, Magnetic Thin Films Composed of Vanadium(II/III)–Chromium(II) Hexacyanochromate(III). *Advanced Materials*, 12(24):1955–1958, 2000.

[43] S. i. Ohkoshi, M. Mizuno, G. j. Hung, and K. Hashimoto. Magnetooptical effects of room temperature molecular-based magnetic films composed of vanadium hexacyanochromates. *The Journal of Physical Chemistry B*, 104(40):9365–9367, oct 2000.

[44] A. Asahara, M. Nakajima, R. Fukaya, H. Tokoro, S.i. Ohkoshi, and T. Suemoto. Ultrafast dynamics of reversible photoinduced phase transitions in rubidium manganese hexacyanoferrate investigated by midinfrared CN vibration spectroscopy. *Physical Review B*, 86(19):195138, nov 2012.

[45] L. Hedley, M. D. Horbury, F. Liedy, and J. O. Johansson. Observation of excited state absorption in the V-Cr Prussian blue analogue. *Chemical Physics Letters*, 687:125–130, nov 2017.

[46] G. Azzolina, H. Tokoro, K. Imoto, M. Yoshikiyo, S.i. Ohkoshi, and E. Collet. Exploring ultrafast photoswitching pathways in RbMnFe Prussian blue analogue. *Angewandte Chemie International Edition*, jul 2021.

[47] H. A. Lewis, J. Kirkpatrick, and J. O. Johansson. Preparation of thin films of molecule-based magnets for optical measurements. *Thin Solid Films*, 732:138767, aug 2021.

[48] O. Sato, T. Iyoda, A. Fujishima, and K. Hashimoto. Electrochemically Tunable Magnetic Phase Transition in a High-T_c Chromium Cyanide Thin Film. *Science*, 271(5245):49–51, jan 1996.

[49] E. Coronado, M. Makarewicz, J. P. Prieto-Ruiz, H. Prima-García, and F. M. Romero. Magneto-Optical Properties of Electrodeposited Thin Films of the Molecule-Based Magnet $Cr_{5.5}(CN)_{12}{\cdot}11.5H_2O$. *Advanced Materials*, 23(37):4323–4326, aug 2011.

[50] H. Prima-Garcia, E. Coronado, Juan P Prieto-Ruiz, and F. M Romero. Tailoring magnetic properties of electrodeposited thin films of the molecule-based magnet $Cr_{5.5}(CN)_{12}11.5H_2O$. *Nanoscale Research Letters*, 7(1), apr 2012.

[51] P. Bhatt, S. M. Yusuf, R. Bhatt, and G. Schütz. Magnetic properties of electrochemically prepared crystalline films of Prussian blue-based molecular magnets $K_jCr^{II}_k[Cr^{III}(CN)_6]_l \cdot mH_2O$. *Journal of Solid State Electrochemistry*, 17(5):1285–1293, jan 2013.

[52] S. i. Ohkoshi, Y. Einaga, A. Fujishima, and K. Hashimoto. Magnetic properties and optical control of electrochemically prepared iron–chromium polycyanides. *Journal of Electroanalytical Chemistry*, 473(1-2):245–249, sep 1999.

[53] P. Bhatt, S. M. Yusuf, M. D. Mukadam, and J. V. Yakhmi. Enhancement of Curie temperature in electrochemically prepared crystalline thin films of Prussian blue analogs $K_jFe^{II}_k[Cr^{III}(CN)_6]_l \cdot mH_2O$. *Journal of Applied Physics*, 108(2):023916, jul 2010.

[54] S. i. Ohkoshi, A. Fujishima, and K. Hashimoto. Transparent and colored magnetic thin films: $(Fe^{II}_xCr^{II}_{1-x})_{1.5}[Cr^{III}(CN)_6]$. *Journal of the American Chemical Society*, 120(21):5349–5350, jun 1998.

[55] E. Coronado, M. Fitta, J. P. Prieto-Ruiz, H. Prima-García, F. M. Romero, and A. Cros. MOKE magnetometry as a probe of surface magnetic impurities in electropolymerized magnetic thin films of the Prussian blue analogue $Fe_3[Cr(CN)_6]_2 \cdot 15H_2O$. *Journal of Materials Chemistry C*, 1(42):6981, 2013.

[56] D. F. Shriver, S. A. Shriver, and S. E. Anderson. Ligand field strength of the nitrogen end of cyanide and structures of cubic cyanide polymers. *Inorganic Chemistry*, 4(5):725–730, may 1965.

[57] D. B. Brown, D. F. Shriver, and L. H. Schwartz. Solid-state reactions of iron(II) hexacyanochromate(III). *Inorganic Chemistry*, 7(1):77–83, jan 1968.

[58] J. E. House and J. C. Bailar. Kinetics of the linkage isomerization in iron(II) hexacyanochromate(III). *Inorganic Chemistry*, 8(3):672–673, mar 1969.

[59] E. Reguera, J.A. Bertrán, and L. Nuñez. Study of the linkage isomerization process in hexacyanometallates. *Polyhedron*, 13(10):1619–1624, may 1994.

[60] W. E. Buschmann, S. C. Paulson, C. M. Wynn, M. A. Girtu, A. J. Epstein, H. S. White, and J. S. Miller. Reversed (Negative) Magnetization for Electrochemically Deposited High-T_c Thin Films of Chromium Hexacyanide Magnets. *Chemistry of Materials*, 10(5):1386–1395, apr 1998.

[61] M. F. Dumont, O. N. Risset, E. S. Knowles, T. Yamamoto, D. M. Pajerowski, M. W. Meisel, and D. R. Talham. Synthesis and size control of iron(II) hexacyanochromate(III) nanoparticles and the effect of particle size on linkage isomerism. *Inorganic Chemistry*, 52(8):4494–4501, apr 2013.

[62] S. F. A. Kettle, E. Diana, E. M. C. Marchese, E. Boccaleri, and P. L. Stanghellini. The vibrational spectra of the cyanide ligand revisited: the $\bar{\nu}$(CN) infrared and Raman spectroscopy of Prussian blue and its analogues. *Journal of Raman Spectroscopy*, 42(11):2006–2014, may 2011.

[63] A. Szilágyi. Emanim: Interactive visualization of electromagnetic waves. Web application available at URL, 2019.

[64] G. X. Du, S. Saito, and M. Takahashi. Fast magneto-optical spectrometry by spectrometer. *Review of Scientific Instruments*, 83(1):013103, jan 2012.

[65] E. Sutcliffe and J. O. Johansson. A femtosecond magnetic circular dichroism spectrometer. *Review of Scientific Instruments*, 92(11):113001, nov 2021.

[66] M. Lorenc, M. Ziolek, R. Naskrecki, J. Karolczak, J. Kubicki, and A. Maciejewski. Artifacts in femtosecond transient absorption spectroscopy. *Applied Physics B: Lasers and Optics*, 74(1):19–27, jan 2002.

[67] S. Y. Smolin, A. K. Choquette, J. Wang, S. J. May, and J. B. Baxter. Distinguishing thermal and electronic effects in ultrafast optical spectroscopy using oxide heterostructures. *The Journal of Physical Chemistry C*, 122(1):115–123, dec 2017.

[68] J. K. Cooper, S. E. Reyes-Lillo, L. H. Hess, C.-M. Jiang, J. B. Neaton, and I. D. Sharp. Physical origins of the transient absorption spectra and dynamics in thin-film semiconductors: The case of $BiVO_4$. *The Journal of Physical Chemistry C*, 122(36):20642–20652, aug 2018.

[69] K. Barlow, J. Eng, I. Ivalo, M. Coletta, E. K. Brechin, T. J. Penfold, and J. O. Johansson. Photoinduced Jahn–Teller switch in Mn(III) terpyridine complexes. *Dalton Transactions*, 51(28):10751–10757, 2022.

[70] L. Hedley, N. Robertson, and J. O. Johansson. Electrochromic Thin Films of the V-Cr Prussian Blue Analogue Molecular Magnet. *Electrochimica Acta*, 236:97–103, may 2017.

[71] I. H. Froning, M. Harberts, Y. Lu, H. Yu, A. J. Epstein, and E. Johnston-Halperin. Thin-film encapsulation of the air-sensitive organic-based ferrimagnet vanadium tetracyanoethylene. *Applied Physics Letters*, 106(12):122403, mar 2015.

[72] S. i. Ohkoshi, K. i. Arai, Y. Sato, and K. Hashimoto. Humidity-induced magnetization and magnetic pole inversion in a cyano-bridged metal assembly. *Nature Materials*, 3(12):857–861, nov 2004.

[73] N. Ozaki, H. Tokoro, Y. Miyamoto, and S. i. Ohkoshi. Humidity dependency of the thermal phase transition of a cyano bridged Co–W bimetal assembly. *New J. Chem.*, 38(5):1950–1954, 2014.

[74] X. Qi, S. Pillet, C. Graaf, M. Magott, E.-E. Bendeif, P. Guionneau, M. Rouzières, V. Marvaud, O. Stefańczyk, D. Pinkowicz, and C. Mathonière. Photoinduced mo-CN bond breakage in octacyanomolybdate leading to spin triplet trapping. *Angewandte Chemie International Edition*, 59(8):3117–3121, feb 2020.

[75] E. Coronado, M. C. Giménez-López, G. Levchenko, F. M. Romero, V. García-Baonza, A. Milner, and M. Paz-Pasternak. Pressure-tuning of magnetism and linkage isomerism in iron(II) hexacyanochromate. *Journal of the American Chemical Society*, 127(13):4580–4581, mar 2005.

[76] M. Soldera, A. Koffman-Frischknecht, and K. Taretto. Optical and electrical optimization of all-perovskite pin type junction tandem solar cells. *Journal of Physics D: Applied Physics*, 53(31):315104, jun 2020.

[77] D. J. Beckstead, D. J. De Smet, and J. L. Ord. An Ellipsometric Investigation of the Formation and Conversion of Prussian Blue Films. *Journal of The Electrochemical Society*, 136(7):1927–1932, jul 1989.

[78] L. M. N. Assis, J. R. Andrade, L. H. E. Santos, A. J. Motheo, B. Hajduk, M. Łapkowski, and A. Pawlicka. Spectroscopic and microscopic study of Prussian blue film for electrochromic device application. *Electrochimica Acta*, 175:176–183, sep 2015.

[79] P. Löper, M. Stuckelberger, B. Niesen, J. Werner, M. Filipič, S.-J. Moon, J.-H. Yum, M. Topič, S. De Wolf, and C. Ballif. Complex Refractive Index Spectra of $CH_3NH_3PbI_3$ Perovskite Thin Films Determined by Spectroscopic Ellipsometry and Spectrophotometry. *The Journal of Physical Chemistry Letters*, 6(1):66–71, dec 2014.

[80] B. C. Paulus and J. K. McCusker. On the use of vibronic coherence to identify reaction coordinates for ultrafast excited-state dynamics of transition metal-based chromophores. *Faraday Discussions*, 237:274–299, 2022.

[81] E. M. S. Maçôas, R. Kananavicius, P. Myllyperkiö, M. Pettersson, and H. Kunttu. Relaxation Dynamics of $Cr(acac)_3$ Probed by Ultrafast Infrared Spectroscopy. *Journal of the American Chemical Society*, 129(29):8934–8935, jun 2007.

[82] E. M. S. Maçôas, S. Mustalahti, P. Myllyperkiö, H. Kunttu, and M. Pettersson. Role of Vibrational Dynamics in Electronic Relaxation of $Cr(acac)_3$. *The Journal of Physical Chemistry A*, 119(11):2727–2734, jan 2015.

[83] R. Krishnamurthy and W. B. Schaap. A quartet-doublet transition in hexacyanochromate(III) anion. *Inorganic Chemistry*, 2(3):605–608, jun 1963.

[84] J. J. Alexander and H. B. Gray. Electronic structures of hexacyanometalate complexes. *Journal of the American Chemical Society*, 90(16):4260–4271, jul 1968.

[85] A. Chiang and Arthur W. Adamson. Photochemistry of aqueous $Cr(CN)_6^{3-}$. *The Journal of Physical Chemistry*, 72(11):3827–3831, oct 1968.

[86] M. F. A. Hendrickx, V. S. Mironov, L. F. Chibotaru, and A. Ceulemans. An Ab Initio Study of the Ligand Field and Charge-Transfer Transitions of $Cr(CN)_6^{3-}$ and $Mo(CN)_6^{3-}$. *Journal of the American Chemical Society*, 125(13):3694–3695, apr 2003.

[87] E. Wasielewska. Theoretical interpretation of the photochemical behaviour of $[Cr(CN)_6]^{3-}$ ion by the SlNDO/FEMP method. *Inorganica Chimica Acta*, 122(1):L1–L2, dec 1986.

[88] H. Witzke. Semi-empirical evaluations of the Racah B and C parameters from the crystal field spectra of chromium(III) complexes. *Theoretica Chimica Acta*, 20(2):171–185, 1971.

[89] N. Sabbatini, M. A. Scandola, and V. Balzani. Intersystem crossing efficiency in the hexacyanochromate(III) ion. *The Journal of Physical Chemistry*, 78(5):541–543, feb 1974.

[90] F. Bolletta, M. Maestri, and V. Balzani. Efficiency of the intersystem crossing from the lowest spin-allowed to the lowest spin-forbidden excited state of some chromium(III) and ruthenium(II) complexes. *The Journal of Physical Chemistry*, 80(22):2499–2503, oct 1976.

[91] H. F. Wasgestian. Evidence against the doublet hypothesis. Photolysis of hexacyanochromate(III) in dimethylformamide. *The Journal of Physical Chemistry*, 76(14):1947–1951, jul 1972.

[92] A. Marchaj and Z. Stasicka. Photosubstitution in some cyanide complexes of chromium(III)(1). *Polyhedron*, 2(6):485–487, jan 1983.

[93] A. Marchaj and F. Wasgestian. Ligand field photolysis of $[Cr(CN)_6]^{3-}$ in acetonitrile. *Inorganica Chimica Acta*, 102(1):L13–L15, aug 1985.

[94] C. Ruckebusch, M. Sliwa, P. Pernot, A. de Juan, and R. Tauler. Comprehensive data analysis of femtosecond transient absorption spectra: A review. *Journal of Photochemistry and Photobiology C: Photochemistry Reviews*, 13(1):1–27, mar 2012.

[95] J. S. Beckwith, C. A. Rumble, and E. Vauthey. Data analysis in transient electronic spectroscopy – an experimentalist's view. *International Reviews in Physical Chemistry*, 39(2):135–216, apr 2020.

[96] S. A. Kovalenko, A. L. Dobryakov, J. Ruthmann, and N. P. Ernsting. Femtosecond spectroscopy of condensed phases with chirped supercontinuum probing. *Physical Review A*, 59(3):2369–2384, mar 1999.

[97] M. P. Grubb, A. J. Orr-Ewing, and M. N. R. Ashfold. KOALA: A program for the processing and decomposition of transient spectra. *Review of Scientific Instruments*, 85(6):064104, jun 2014.

[98] M. H. Brooker, G. Hancock, B. C. Rice, and J. Shapter. Raman frequency and intensity studies of liquid H_2O, $H_2{}^{18}O$ and D_2O. *Journal of Raman Spectroscopy*, 20(10):683–694, oct 1989.

[99] E. Zinato and P. Riccieri. Pentacyanochromate(III) complexes: ground- and excited-state chemistry. *Coordination Chemistry Reviews*, 211(1):5–24, jan 2001.

[100] F. D. Camassei and L. S. Forster. Relaxation of Excited States in Cr(III) Complexes. *The Journal of Chemical Physics*, 50(6):2603–2613, mar 1969.

[101] S. i. Ohkoshi, J. Shimura, K. Ikeda, and K. Hashimoto. Magnetization-induced second- and third-harmonic generation in transparent magnetic films. *Journal of the Optical Society of America B*, 22(1):196, jan 2005.

[102] J. P. Fackler and D. G. Holah. Properties of Chromium(II) Complexes. I. Electronic Spectra of the Simple Salt Hydrates. *Inorganic Chemistry*, 4(7):954–958, jul 1965.

[103] D. M. Rogers and J. O. Johansson. Metal-to-metal charge-transfer transitions in Prussian blue hexacyanochromate analogues. *Materials Science and Engineering: B*, 227:28–38, jan 2018.

[104] G. C. Allen and N. S. Hush. Intervalence-Transfer Absorption. Part 1. Qualitative Evidence for Intervalence-Transfer Absorption in Inorganic Systems in Solution and in the Solid State. In *Progress in Inorganic Chemistry*, pages 357–389. John Wiley & Sons, Inc., January 1967.

[105] N. S. Hush. Intervalence-Transfer Absorption. Part 2. Theoretical Considerations and Spectroscopic Data. In *Progress in Inorganic Chemistry*, pages 391–444. John Wiley & Sons, Inc., January 1967.

[106] W. Kaim, B. Sarkar, and G. Kumar Lahiri. Mixed-Valence Intermediates as Ideal Targets for Spectroelectrochemistry (SEC). In *Spectroelectrochemistry*. The Royal Society of Chemistry, 07 2008.

[107] J. P. Eaton and D. Nicholls. The complex cyanides of chromium(II) and chromium(0). *Transition Metal Chemistry*, 6(4):203–206, aug 1981.

[108] M. B. Robin and P. Day. Mixed valence chemistry-a survey and classification. In *Advances in Inorganic Chemistry and Radiochemistry*, pages 247–422. Elsevier, 1968.

[109] D. Hayes, R. G. Hadt, J. D. Emery, A. A. Cordones, A. B. F. Martinson, M. L. Shelby, K. A. Fransted, P. D. Dahlberg, J. Hong, Xiaoyi Zhang, Q. Kong, R. W. Schoenlein, and L. X. Chen. Electronic and nuclear contributions to time-resolved optical and X-ray absorption spectra of hematite and insights into photoelectrochemical performance. *Energy & Environmental Science*, 9(12):3754–3769, 2016.

[110] D. C. Arnett, P. Voehringer, and N. F. Scherer. Excitation dephasing, product formation, and vibrational coherence in an intervalence charge-transfer reaction. *Journal of the American Chemical Society*, 117(49):12262–12272, dec 1995.

[111] D. Weidinger, D. J. Brown, and J. C. Owrutsky. Transient absorption studies of vibrational relaxation and photophysics of Prussian blue and ruthenium purple nanoparticles. *The Journal of Chemical Physics*, 134(12):124510, mar 2011.

[112] H. Oshio, H. Onodera, and T. Ito. Spectroelectrochemical Studies on Mixed-Valence States in a Cyanide-Bridged Molecular Square, $[Ru^{II}{}_2Fe^{II}{}_2(\mu\text{-}CN)_4(bpy)_8](PF_6)_4 \cdot CHCl_3 \cdot H_2O$. *Chemistry - A European Journal*, 9(16):3946–3950, aug 2003.

[113] Ø. Hatlevik, W. E. Buschmann, J. Zhang, J. L. Manson, and J. S. Miller. Enhancement of the Magnetic Ordering Temperature and Air Stability of a Mixed Valent Vanadium Hexacyanochromate(III) Magnet to 99 °C (372 K). *Advanced Materials*, 11(11):914–918, aug 1999.

[114] F. Ureña-Begara, A. Crunteanu, and J.-P. Raskin. Raman and XPS characterization of vanadium oxide thin films with temperature. *Applied Surface Science*, 403:717–727, may 2017.

[115] C. Cartier dit Moulin, F. Villain, A. Bleuzen, M.-A. Arrio, P. Sainctavit, C. Lomenech, V. Escax, F. Baudelet, E. Dartyge, J.-J. Gallet, and M. Verdaguer. Photoinduced Ferrimagnetic Systems in Prussian Blue Analogues $C^{I}Co_4[Fe(CN)_6]_y$ (C^{I} = Alkali Cation). 2. X-ray Absorption Spectroscopy of the Metastable State. *Journal of the American Chemical Society*, 122(28):6653–6658, jun 2000.

[116] R. Garde, F. Villain, and M. Verdaguer. Molecule-based room-temperature magnets: Catalytic role of V(III) in the synthesis of vanadium-chromium Prussian blue analogues. *Journal of the American Chemical Society*, 124(35):10531–10538, aug 2002.

[117] F. J. Luque, I. A. Kowalik, J. P. Prieto-Ruiz, M. Á. Niño, H. Prima-García, F. M. Romero, D. Arvanitis, E. Coronado, R. Miranda, and J. J. de Miguel. Magnetic ordering in an $(Fe_{0.2}Cr_{0.8})_{1.5}[Cr(CN)_6]$ Prussian blue analogue studied with synchrotron radiation based spectroscopies. *Journal of Materials Chemistry C*, 6(30):8171–8186, 2018.

[118] P. Zimmermann, S. Peredkov, P. Macarena Abdala, S. DeBeer, M. Tromp, C. Müller, and J. A. van Bokhoven. Modern X-ray spectroscopy: XAS and XES in the laboratory. *Coordination Chemistry Reviews*, 423:213466, nov 2020.